# Multiphase Hydrodynamics in Flotation Systems

Michael Richard Brady

Dissertation submitted to the faculty of the Virginia Polytechnic Institute and State University in partial fulfillment of the requirements for the degree of

Doctor of Philosophy
In
Engineering Mechanics

Pavlos P. Vlachos, Committee Chair
Demetri Telionis, Member
R.H. Yoon, Member
Saad A. Ragab, Member
Gerry Luttrell, Member

August 12, 2009
Blacksburg, Virginia, USA

Keywords: Multiphase Fluid Mechanics, Turbulent Collisions, Turbulent Mixing, Bubble Dynamics, Foam Physics, Foam Drainage, Flotation

Multiphase Hydrodynamics in Flotation Systems

Michael Richard Brady

## ABSTRACT

Flotation is a complex, multiphase process used to separate minerals. Four problems central to the fundamentals of the flotation process were studied. A multiphase grid turbulence experiment was conducted to verify particle collision models. The slip velocities of solid particles and bubbles were measured using Digital Particle Image Velocimetry (DPIV). The experimental results were compared with the predictions from empirical and theoretical collision models.

Time-resolved DPIV was used to measure the turbulent velocity field in a Rushton turbine around the impeller region. The turbulence quantities were found by removing the periodic component from the blade passing, which is a dominant part of the measured velocities near the impeller. We provide evidence that larger, biased dissipation and turbulent kinetic energy values are estimated in the vicinity of the impeller due to the periodic component of the blade passage. The flow was found to be anisotropic close to the impeller. Vortex detection revealed that the tip vortices travel in a nearly radial direction from the impeller for small Reynolds numbers and with a wider distribution for higher Reynolds numbers.

The rise of a buoyant bubble and its interaction with a free liquid surface was experimentally investigated using Time-Resolved Digital Particle Image Velocimetry as a function of bubble size, and surfactant concentration of the fluid medium. It is shown that the presence of a surfactant significantly affected the characteristics of the velocity field during the rise and interaction with the free surface. This difference is attributed to the adsorption coverage of the

surfactant at the bubble-fluid interface. Wake profiles were compared. The presence of large vortices were observed and found to play a significant role.

Finally, Numerical and experimental results of stable and unstable foams are presented by comparing liquid fractions and bubble sizes. There was good agreement between the experiments and numerical modeling in free drainage and forced drainage experiments. In addition, foam coarsening was measured and characterized experimentally.

Each of the problems investigated have added to the understanding in the underlying physics of the flotation process and can lead to more accurate modeling. The ultimate goal of this work is to contribute to the design of more effective and efficient flotation machines.

## ACKNOWLEDGEMENTS

I would like to first thank my family for all of their encouragement. My mother for inspiration. My father for perseverance. My stepfather and stepmother for their support and guidance. And the rest of my family who have helped in more ways than they know.

My advisors deserve thanks for helping me progress this research. And finally, my friends and co-workers, who have made this process so enjoyable.

To everyone, my deepest gratitude. Without you, this milestone would not have been possible.

# ATTRIBUTION

The following people have made scholarly contributions to this dissertation. All have contributed in co-authorship, proofreading, or editing of the individual chapters. A brief description of their contributions will be given.

**Asst. Prof. Pavlos P. Vlachos** – Committee chair and coauthor. Provided guidance throughout the entirety this work.

**Prof. Demetri Telionis** – Committee member and coauthor. Provided guidance in research, editing and proofreading.

**Prof. Roe-Hoan Yoon** – Committee member and coauthor. Provided guidance on chapters 1 and 4. In addition, he contributed to the overall impact of this dissertation.

**Hyunsun Do** – Ph.D. Student, Engineering Science and Mechanics Department. Hyunsun performed the numerical analysis in Chapter 5. He is also first author, in addition to myself, in chapter 5.

# TABLE OF CONTENTS

## LIST OF FIGURES

# LIST OF TABLES

# Chapter 1: Dissertation Introduction and Overall Background

## INTRODUCTION

A Flotation system is a complex, three phase process used to selectively separate minerals from raw materials. Solid particles are released into a liquid medium and separated by the addition of a gas phase. The discriminatory separation occurs as the hydrophobic particles attach to the rising air bubbles, while the hydrophilic or less hydrophobic particles remain in the turbulent slurry. The hydrophobic particles, along with the air bubbles, form froth at the top of the vessel and are then extracted from the system mechanically. Surfactants are added to alter the surface characteristics by changing the contact angle and the surface tension. The surfactants have two main functions: to increase the likelihood that the particle and bubble will attach when they collide, and to help in controlling the bubble size.

Flotation occurs within a highly turbulent environment. Turbulence is typically generated with an impeller. The unsteady nature of the turbulence is used to increase the collision frequency of particle and bubble. In addition, bubble breakup is also heavily controlled by the turbulence characteristics. Once the particle collides with a bubble, it must attach and stay attached throughout the pulp and froth phases to ensure recovery. The complex interaction of hydrodynamic and surface forces ultimately controls the efficiency of the flotation process.

The objective of this study is to investigate fundamental fluid mechanical problems relating to the flotation process. The focus is on the hydrodynamics in the turbulent pulp phase, as well as the froth phase. Four problems were studied experimentally. A multiphase grid turbulence experiment was conducted to verify particle collision models. The turbulent characteristics of a Rushton mixing tank were measured in its impeller stream. The interaction of a rising bubble

with a free interface was investigated. And finally, the drainage and structure of coarsening foams were measured experimentally and compared to a numerical model. Each of the four problems studied here were determined to be areas where modern experimental fluid mechanics can contribute fundamental research to the current state of knowledge. The understanding of the underlying physics can lead to the design and use of more efficient flotation systems.

## REVIEW OF LITERATURE

### Multiphase collision measurements and modeling

Flotation cells are designed to maximize the collision rates between particles and bubbles. The flotation process occurs within a highly turbulent three-phase flow, a detailed understanding of which is still limited. Knowledge of the dispersed phase velocities is a basis for understanding what occurs in a turbulent, multi-phase environment. In many analytical formulations of flotation processes, the rate of collision is modeled in terms of the fluctuations of bubbles and particles.

The empirical model of Liepe and Möckel ([1]), which is one of the most frequently cited in the flotation literature, is essentially a compilation of experimental data from six different earlier publications. The RMS velocities of the particle phase were measured along with the fluid phase. Schubert ([2]) used the model extensively in his studies on the effect of various hydrodynamic parameters on flotation. Moreover, the predictions from this, and the other analytical models have not been compared experimentally. In this study, we present experimental results using modern methods and compare the performance of the most widely used turbulent collision models.

The frequency of collisions between bubbles and particles is one of the most important parameters in flotation modeling. It is usually modeled as a linear relation to the particle and bubble number densities and is proportional to the square of the sum of the radii of the two phases,

$$\mathbf{Z_{12} = C_{12} N_1 N_2 R_{12}^2} \tag{1.1}$$

Saffman and Turner ([3]) proposed a model to calculate the collision frequency based on the fluid mechanics of the system. It is based on the sum of the particle radii, the number densities, the viscosity and the energy dissipation rate.

$$\mathbf{Z_{12} = \sqrt{\frac{8\pi}{15}} R_{12}^3 N_1 N_2 \sqrt{\frac{\varepsilon}{\nu}}} \tag{1.2}$$

Abrahamson ([4]) proposed a collision frequency between particles of two kinds, labeled 1 and 2, where the Stokes number of the colliding particles is very large, essentially assuming that particle motion is completely uncorrelated with the flow. Equation 1.3 is dependent upon the slip velocity of the dispersed phase, $U_i$, that is the velocity of the particle or bubble, minus the velocity of the flow in the same location.

$$\mathbf{Z_{12} = 2^{3/2} \pi^{1/2} N_1 N_2 d_{12}^2 \sqrt{\left(\overline{U_1^2} + \overline{U_2^2}\right)}} \tag{1.3}$$

This equation has been used extensively to predict collision rates between bubbles and particles in flotation ([5]).

There are various methods of calculating the variance of the particle and bubble slip velocities, $\overline{\mathbf{U_i^2}}$. All have their associated assumptions. They are described in detail in Chapter 2. No research to date has experimentally measured the slip velocity of particles and bubbles in a turbulent flow and compared the various models.

The main objective in this study is to measure the fluctuations of particles and bubbles in a developing and eventually homogenous turbulent flow field using Time Resolved Particle Image Velocimetry. The RMS of these velocity fluctuations are then calculated, in order to compare the various collision models stated above. The validation of the collision models contributes to more accurate flotation modeling.

### Turbulence characteristics of stirred vessels

Flotation systems employ a variety of impeller designs. Blade design influences the turbulent structures in the flow as well as the bubble breakup characteristics. A multitude of designs are used. To study the fundamentals of the turbulence in the pulp phase of a flotation system, a bench top mixing tank provides a simple and reproducible model to study. There is a wealth of experimental and numerical studies of the turbulent characteristics of the flow in stirring tanks. These are cylindrical tanks in which a stirring device generates turbulence. Stirring tanks are widely used in a large number of applications in industries to promote blending, chemical reaction, micro mixing etc. Mixing processes are very important elements in many industrial devices, but at the same time they involve complex phenomena, since in most cases, the flow is turbulent over the entire volume and strongly inhomogeneous and anisotropic.

The flow in mixing vessels is typically generated with rotors or impellers. The impeller agitates the flow and creates shear characteristics in accordance with the requirements of the mixing process. Bladed impellers can cause strong gradients in the flow, which lead to turbulence and higher shear rates. As the rotor agitates the flow, recirculation regions form. The Rushton design has been particularly studied partly due to its simplicity. A description of its geometry can be found in Chapter 3.

Researchers have used a variety of methods to record velocity fluctuations in stirring tanks, such as Hot Wire Velocimetry, Laser-Doppler Velocimetry and more recently Particle Image Velocimetry. Although mixing in stirring tanks has been extensively studied in the past years computationally and experimentally, our understanding of the underlying physics of and turbulent mixing is not yet complete. The main objective of the present study is to record the flow field with high temporal and spatial resolution to provide better understanding of the nature of mixing in a stirring vessel.

Although previous efforts provided valuable insight of the mixing process in Rushton vessels, no experimental effort has been directed at resolving the global character of the flow with sufficient temporal resolution. Experimental efforts with high temporal resolution have been attempted, however they were limited to point measurements. The present effort addresses this issue by employing state of the art, non invasive flow diagnostics, and allowing spatially resolved measurements with KHz sampling frequency. Both the spatial and temporal dynamics of the mixing process are analyzed. In addition the motion of the turbulent structures will be studied to understand the momentum and energy transport characteristics.

### The interaction of a bubble with a free interface

The study of the dynamics of bubble motion is an important problem in fluid mechanics. A variety of processes involve bubble motion, especially those involving particle separations. Bubble collisions with other bubbles or solid particles represents a fundamental problem in multi-phase flows. This problem is further enhanced with the presence of surfactants in the liquid.

The aim of this work is to study the dynamics of a bubble rising and interaction with a free surface and the effect of surfactants on this process. A great deal of work has been carried

out concerning the dynamics of a solid sphere rebounding on a wall immersed in a fluid. Much of the work involves optically tracking the motion of the sphere and measuring the coefficient of restitution (velocity after impact divided by the velocity before impact). The Stokes number has been shown to be a good indicator of the coefficient of restitution. An explanation of the dependence on the Stokes number has been given by relating it to the lubrication force around impact.

Work involving bubbles or buoyant droplets has been investigated by a number of authors. Legendre et al.([6]) performed shadowgraph experiments to track a rising drop as it struck a solid wall. It was determined that 80% of the initial kinetic energy was dissipated with a single collision with the solid wall. Canot et al. ([7]) numerically modeled a bubble bouncing on a solid surface using the Boundary Element Method. However this was done using a potential flow model and solving the Laplace equation.

Bubble motion is significantly affected by the properties of the gas-liquid interface. The effect of surfactants on bubble motion in various liquids has been investigated by various authors. Malysa et al. ([8]) classified the velocity of a rising bubble as a function of the concentrations of various solutions and the adsorption coverage of the surfactants. The bubble velocity was found to be significantly influenced by the extent of the adsorption coverage of the surfactant to the bubble. A variety of theoretical works ([9] and [10]) explaining the underlying mechanisms of surfactant adsorption and its effect on the bubble velocity has also been carried out.

To date, a time resolved picture of the flow around a bubble impacting a surface has not been done. If the dynamics are to be fully understood, the fluid flow and its coupling with the bubble motion should be understood. In this study, the flow around an impacting bubble as well

as the bubble shape and trajectory are measured using Particle Image Velocimetry. The objective is to understand the forces involved with a bubble impact with a free surface as well as the flow structures in the subsequent wake.

### Foam Drainage and Coarsening

The froth phase in flotation is a very important factor in optimizing the recovery of the system. The foam in flotation systems is generally unstable (coarsens). The drainage of stable foams has been extensively studied. Unstable foams have also been studied but to a lesser extent.

The foam structure can be thought of as a complex network of films and solid pipes. These films are called lamellae, and the edges of the polyhedra meet along tubes called Plateau borders (PB). The diameters of these pipes can expand and contract depending on the wetness of the foam. The liquid drainage takes place along the Plateau Borders.

Small amounts of surfactants are enough to create a no-slip condition on the walls of the lamellae and the PBs. Authors (Leonard and Lemlich [11]; Verbist et. al. [12]) have neglected the viscous losses along the junctions and arrive at simple equations that govern foam drainage. More advanced modeling has also been achieved (Neethling *et al*. [13]; Koehler *et al*. [14]) by taking into account losses in the junctions. Analytical solution that meet idealized initial and/or boundary conditions also exist ([12]).

Coarsening, a very common phenomenon in practical situations is controlled by two major well-known mechanisms. The first is gas diffusion. Pressure gradients between the different sized bubbles cause gas to diffuse from the smaller bubbles to the larger. However, gas diffusion is often neglected in practical foams because it is a much slower process than drainage. The second mechanism is film rupture. As liquids drain through bubbles, the film gets thinner and

thinner until it breaks. Coarsening characteristics are generally inferred from the changing drainage properties such as the measured velocity (Hutzler and Weaire [15]). Direct observation of the changing bubble size, which defines coarsening, is a more useful tool to study foam dynamics and validate foam models. Two major methods to directly analyze bubble size within the foam are light scattering using a coherent light source, and optical measurements using photography. Light scattering directs a laser from one side of foam to the other, and determines the bubble size based on the attenuation of light intensity (Weaire and Hutzler [16]). This technique is useful, however it requires a complex model to determine the average bubble size along with assumptions about the foam. Direct optical measurements use image processing to separate the individual bubbles and determine the diameter. In the present study we use direct optical measurement to determine the bubble size and capacitance measurements to determine the liquid fraction. Bubble size and liquid fraction are independently measured in a time resolved fashion to study foam drainage and coarsening. The objective here is to characterize the liquid fraction and bubble size experimentally and validate foam drainage models for stable and coarsening foams.

## REFERENCES


1. Liepe, F. and M. Hans-Otto, Untersuchungen zum Stoffvereinigen in Flüssiger Phase. Chem. Techn., 1976. 28(Jg., Heft 4).
2. Schubert, H., On the turbulence-controlled microprocesses in flotation machines. International Journal of Mineral Processing, 1999. 56(1-4): p. 257-276.
3. Saffman, P.G. and J.S. Turner, On the collision of drops in turbulent clouds. Journal of Fluid Mechanics, 1956. 1: p. 16-30.
4. Abrahamson, J., COLLISION RATES OF SMALL PARTICLES IN A VIGOROUSLY TURBULENT FLUID. Chemical Engineering Science, 1975. 30(11): p. 1371-1379.
5. Schubert, H., On the turbulence-controlled microprocesses in flotation machines. International Journal of Mineral Processing, 1999. 56(1-4): p. 257-276.
6. Legendre, D., C. Daniel, and P. Guiraud, Experimental study of a drop bouncing on a wall in a liquid. Physics of Fluids, 2005. 17(9): p. -.
7. Canot, E., et al., Numerical simulation of the buoyancy-driven bouncing of a 2-D bubble at a horizontal wall. Theoretical and Computational Fluid Dynamics, 2003. 17(1): p. 51-72.
8. Malysa, K., M. Krasowska, and M. Krzan, Influence of surface active substances on bubble motion and collision with various interfaces. Advances in Colloid and Interface Science, 2005. 114: p. 205-225.
9. Zholkovskij, E.K., et al., Dynamics of rear stagnant cap formation at low Reynolds numbers 1. Slow sorption kinetics. Journal of Colloid and Interface Science, 2000. 226(1): p. 51-59.
10. Griffith, R.M., The effect of surfactants on the terminal velocity of drops and bubbles. Chemical Engineering Science, 1962. 17: p. 107-1070.
11. Leonard, R.A. and Lemlich, R., 1965, A study of interstitial liquid flow in Foam", AICHE Journal, 11, 18-29.
12. Verbist, G., Weaire, D. and Kraynik, A.M., 1996, The foam drainage equation, J.Phys.:Condens.Matter 8, 3715-3731.
13. Neethling, S.J., Lee, H.T. and Cilliers, J.J.,2002, A foam drainage generalized for all liquid contents, .Phys.:Condens.Matter 14,331-342.

14. Koehler, S.A., Hilgenfeldt, S. and Stone, H.A.,2000, A generalized view of foam drainage: experiment and theory, Langmuir 16, 6327-6341.
15. Hutzler, S., Weaire, D., 2000, Foam coarsening under forced drainage, Philosophical Magazine Letters 80(6), 419-425.
16. Weaire, D., and Hutzler, S., The Physics of Foams, 2001, Oxford University Press.

# Chapter 2: Evaluation of multiphase flotation models in grid turbulence via Particle Image Velocimetry

Michael Brady[1], Pavlos P. Vlachos[2], Demetri P. Telionis[1] and Roe-Hoan Yoon[3]
[1]Department of Engineering Science and Mechanics
[2]Department of Mechanical Engineering
[3]Department of Mining Engineering
Virginia Polytechnic Institute & State University
Blacksburg, VA 24060 USA

Reprinted from *The International Journal of Mineral Processing*, vol. 80, M. Brady, P. Vlachos, D. Telionis, R.H. Yoon, "Evaluation of multiphase flotation models in grid turbulence via Particle Image Velocimetry", pp. 133-143, 2006, with permission from Elsevier

## ABSTRACT

Industrial processes involving multi-phase flows such as flotation require understanding of the relationships between bubbles, solid particles and the flow. Modern experimental tools are employed in this effort to measure with great accuracy the basic features of the motion of all three phases in turbulent flow. We employed a unique Digital Particle Image Velocimeter (DPIV) that can record with great accuracy and kHz temporal resolution, velocity vectors of all three phases, namely the fluid, the solid particles and the air bubbles. The interaction of these three phases was studied in homogeneous isotropic turbulence generated by cylindrical grids. Particles and bubbles were released into the turbulence and the motions of the three phases were monitored. The experimental results obtained in the present work were compared with the predictions of the models published in the literature.

## INTRODUCTION

Flotation cells use bubbles to collect solid particles selectively. They are designed to maximize the collision frequencies between particles and bubbles. The flotation process occurs within a highly turbulent three-phase flow, a detailed understanding of which is still limited. Knowledge of the dispersed phase velocities is a basis for understanding what occurs in a turbulent, multi-phase environment. In many analytical formulations of flotation processes, the rate of collision is modeled in terms of the fluctuations of bubbles and particles. These in turn are related to the character of the turbulent flow that drives both bubbles and particles. Typical very recent examples of such models are presented in [1] and [2].These are either empirical models based on

## Nomenclature

| | |
|---|---|
| Subscript i | dispersed phase (particle or bubble) |
| Subscript l | liquid |
| Superscript * | nondimentional quantity |
| $C_{12}$ | collision frequency coefficient [$m \cdot s^{-1}$] |
| $d_i$ | diameter of phase i [m] |
| $d_{12}$ | sum of radii of particle and bubble |
| $N_i$ | number density of phase i [$m^{-3}$] |
| $R_{12}$ | radius of collision [m] = $(d_1+d_2)/2$ |
| St | Stokes number, ratio of particle time scale to flow time scale |
| T | Lagrangian integral scale |
| $u_i$ | $i^{th}$ component of fluctuating velocity |
| $\sqrt{\overline{\mathbf{U_i^2}}}$ | root-mean-squared velocity of i with respect to flow [$m \cdot s^{-1}$] |
| $\overline{\mathbf{U_i^2}}$ | variance of phase i with respect to flow [$m^2 \cdot s^{-2}$] |
| $\overline{\mathbf{U_l^2}}$ | variance of flow velocity |
| $\overline{(U_i^2)}_{abs}$ | variance of velocity of phase i [$m^2 \cdot s^{-2}$] |
| $\mathbf{U_o}$ | Characteristic velocity [$m \cdot s^{-1}$] |
| $Z_{12}$ | collision frequency between particle and bubble [$m^{-3} \cdot s^{-1}$] |
| $\varepsilon$ | kinetic energy dissipation rate[$m^2 \cdot s^{-3}$] |
| $\boldsymbol{\mu}$ | viscosity [$N \cdot s \cdot m^{-2}$] |
| $\eta$ | Kolmogorov length scale |
| $\boldsymbol{\nu}$ | kinematic viscosity [$m^2 \cdot s^{-1}$] |
| $\rho_i$ | density of i [$kg \cdot m^{-3}$] |
| $\tau_i$ | relaxation time of i [s] |
| L | Characteristic length [m] |
| $\mathbf{x}_j$ | Cartesian direction [m] |

experimental data analysis ([3]), or analytical formulations based on theoretical approximations ([4]; [5]; [6]). The Liepe and Möckel model was developed nearly thirty years ago on the basis of data obtained using laboratory techniques of limited accuracy, while the analytical models are all approximations. No attempt has been made so far to validate either the empirical or the analytical models using modern experimental tools. This is the purpose of the present communication.

The model of Liepe and Möckel, which is most frequently cited in the flotation literature is a essentially a compilation of experimental data from six different earlier publications. Schubert ([7]) used the model extensively in his studies on the effect of various hydrodynamic parameters on flotation. One should note here that all of these experiments were carried out with solid particles heavier than water. Therefore, use of the Liepe and Möckel model to estimate the turbulent root mean square velocities of bubbles in a flotation cell is questionable. Moreover, the predictions from the analytical models have not been compared either with each other or against experimental data. In the present paper we present experimental results obtained with modern powerful methods and compare the performance of the most popular models against the new experimental data and against each other.

The present experiments were conducted in a facility where turbulence is generated by a grid of cylindrical rods. This offers a wide range of turbulence scales, beginning with the regions immediately downstream of the rods, where large vortical structures reside. Far from the grid, turbulence tends to become homogeneous. The turbulence characteristics are, therefore, similar to those found in flotation cells and flotation columns, but they are well defined and the experiments are repeatable. In the experiments discussed here the turbulent kinetic energy and the corresponding turbulent dissipation are much lower than those encountered near the impeller

of a flotation machine. We are currently repeating these measurements in a stirring tank and will report the results in a subsequent publication.

## Collision Models

The frequency of collision between bubbles and particles is usually modeled as a linear relation to the particle and bubble number densities and is proportional to the square of the sum of the radii of the two phases,

$$\mathbf{Z}_{12} = \mathbf{C}_{12}\mathbf{N}_1\mathbf{N}_2\mathbf{R}_{12}^2 \qquad \textbf{2.1}$$

Saffman and Turner ([5]) proposed two collision models. The first took into account only the shear mechanism for collision and is based on the assumption that the Stokes number asymptotically approaches zero.

$$\mathbf{Z}_{12} = \sqrt{\frac{8\pi}{15}}\mathbf{R}_{12}^3\mathbf{N}_1\mathbf{N}_2\sqrt{\frac{\varepsilon}{\nu}} \qquad \textbf{2.2}$$

The second model accounted for inertial differences due to gravity and turbulent accelerations.

Abrahamson ([6]) proposed a collision frequency between particles of two kinds, labeled 1 and 2, where the Stokes number of the colliding particles is very large, essentially assuming that particle motion is completely uncorrelated with the flow. Thus, Abrahamson's collision frequency,

$$\mathbf{Z}_{12} = 2^{3/2}\pi^{1/2}\mathbf{N}_1\mathbf{N}_2\mathbf{d}_{12}^2\sqrt{\left(\overline{\mathbf{U}_1^2} + \overline{\mathbf{U}_2^2}\right)}, \qquad \textbf{2.3}$$

accounted for only the accelerative mechanism for collisions. The slip velocity, $U_i$, is defined as the velocity of the dispersed phase (particle of bubble), minus the velocity of the flow field in the same location. Equation has been used extensively to predict collision rates between bubbles and particles in flotation ([7]).

There are various methods of calculating the variance of the particle and bubble slip velocities, $\overline{\mathbf{U_i^2}}$. One such method is based on a derivation from the BBO equation ([4]) that assumes single-frequency oscillations,

$$\frac{\overline{\mathbf{U_i^2}}}{\overline{\mathbf{U}^2}} = \frac{(1-\mathbf{b})^2}{\mathbf{aT}+1} \qquad \textbf{2.4}$$

$$a = \frac{36\mu}{(2\rho_i + \rho_f)d_p{}^2} \qquad b = \frac{3\rho_f}{2\rho_i + \rho_f}$$

Equation 2.4 can also be written in terms of the absolute RMS velocities,

$$\frac{\overline{(\mathbf{U_i^2})_{abs}}}{\overline{\mathbf{U}}^2} = \frac{\mathbf{aT}+\mathbf{b}^2}{\mathbf{aT}+1} \qquad \textbf{2.5}$$

Abrahamson also included a simplification to Equation 2.5 by assuming solid particles in a gas (b=0, a=$1/\tau_p$) and calculating the time scale, $T = 0.7\overline{U^2}/\varepsilon$, therefore reducing to the following equation

$$\overline{(U_i^2)}_{abs} = \frac{\overline{U^2}}{1+1.5\tau_i \varepsilon / \sqrt{\overline{U^2}}} \qquad 2.6$$

The most common form used in flotation research is a combination of the collision frequency given by Abrahamson and the particle root-mean-squared velocity with respect to the flow given by Liepe and Möckel, and proposed for use in flotation research ([7]) .

$$\sqrt{\overline{U_i^2}} = 0.33 \frac{\varepsilon^{4/9} d_i^{7/9}}{\nu^{1/3}} \left( \frac{\rho_i - \rho_l}{\rho_l} \right)^{2/3} \qquad 2.7$$

This expression was developed by dimensional analysis and least-squares fitting over a large number of experimental data from several sources and is valid at intermediate Stokes numbers where flotation processes occur.

Lee and Erickson. ([8]) derived an approximation to determine the bubble RMS.

$$\overline{(U_i^2)}_{abs} = 2(d_{12}\varepsilon)^{2/3} \qquad 2.8$$

One final model we will discuss was developed by Williams and Crane ([9]) and is a modification of the approach developed by Levins and Glastonbury. Equations 2.4 through 2.6 require the assumption of an exponential decay form of the Lagrangian correlation function and was shown not be applicable in the viscous subrange of turbulence by Williams and Crane. The spectrum was modified to take into account small-scale turbulence, resulting in the following equation

$$\frac{\overline{(U_i^2)}_{abs}}{\overline{U_i^2}} = \frac{\gamma}{\gamma - 1} \left( \frac{1}{1+\theta_i} - \frac{1}{(1+\gamma\theta_i)\gamma} \right) \qquad 2.9$$

where, $\gamma = 2(L_f / \lambda_g)^2$, $L_f = \sqrt{\overline{U_i^2}}\, T_L$, $\lambda_g = \sqrt{\overline{U_i^2}}\,(15\nu/\varepsilon)^{1/2}$, and $\theta_i = St = \tau_i / T_L$.

There are limitations to all of these models. Saffman and Turner assume Stokes numbers of 1 or less, while Abrahamson assumes a Stokes number of infinity. Neither of these conditions is valid within the flotation environment over the particle sizes that are usually common in flotation processes. Liepe and Möckel's model should be valid for particles at intermediate Stokes numbers. The limitation is that Eq. (7) was derived from experimental data obtained with solid particles and therefore is valid for particles, with density greater than that of the fluid, which is not the case with air bubbles. In addition, the Williams and Crane model does not incorporate a turbulent shear mechanism for collisions.

To determine how these limitations affect collision rates, fluid velocity measurements have been recorded in grid turbulence. The velocity at the Kolmogorov scale, $\mathbf{U}=(\boldsymbol{\varepsilon\nu})^{1/4}$, has been determined from these and compared against the RMS velocities predicted by the four models described above. The nondimentionalized forms of these models are shown in Table 2.1. These comparisons will show how well each predicts small particle fluctuations. Some preliminary measurements on flow fluctuations and particle fluctuations were presented at the Annual Meeting of Society of Mining Engineers ([10]), in which results were reported on particle velocity fluctuations. In the present communication, we include more results and add data on bubble velocity fluctuations.

**Table 2.1 - Summary of models**

| Original Derivation | valid for: | Nondimentionalized Equation | Eq. no. |
|---|---|---|---|
| Liepe and Möckel | Intermediate St, | $\sqrt{\overline{U_i^{*2}}} = 0.33\,Re^{1/3}\,\varepsilon^{*4/9} d_i^{*7/9}\left(\frac{\rho_i-\rho_f}{\rho_f}\right)^{2/3}$ | **2.10** |
| Levins and Glastonbury | | $\frac{\overline{U_i^{*2}}}{\overline{U^{*2}}} = \frac{(1-b)^2}{aT^*L/U_o+1}$ | **2.11** |
| Abrahamson | St>>1, Accelerative mechanism only | $\overline{(U_i^{*2})}_{abs} = \frac{\overline{U^{*2}}}{1+1.5\tau_i^*\varepsilon^*\sqrt{\overline{U^2}}}$ | **2.12** |
| Williams and Crane | St>>1, Accelerative mechanism only | $\frac{\overline{(U_i^{*2})}_{abs}}{\overline{U^{*2}}} = \frac{\gamma^*}{\gamma^*-1}\left(\frac{1}{1+\theta^*_i}-\frac{1}{(1+\gamma^*\theta^*_i)\gamma^*}\right)$ | **2.13** |
| Lee and Erickson. | Bubbles | $\overline{(U_i^{*2})}_{abs} = 2(d_{12}^*\varepsilon^*)^{2/3}$ | **2.14** |

The main objective of this project is to record the fluctuations of particles and bubbles in a homogenous turbulent flow field. The RMS of these velocity fluctuations are then calculated, in order to compare the various models stated above. Each of these models relies on the accurate determination of the kinetic energy dissipation rate. Our measurement technique to determine the dissipation rate is now discussed.

## Kinetic Energy Dissipation Rate

The kinetic energy dissipation rate has been shown to determine the degree of droplet and bubble break up and rates of chemical reactions. Direct calculation of the dissipation rate from the definition,

$$\varepsilon = \frac{\upsilon}{2}\left\langle\left(\frac{\partial u_i}{\partial x_j} + \frac{\partial u_j}{\partial x_i}\right)^2\right\rangle, \qquad \textbf{2.15}$$

requires the evaluation of the strain rate fields at a spatial resolution less than the Kolmogorov length scale. In the above equation the bracket implies summation of such terms over combinations with i and j taking the values of 1 through 3. So far, there are no experimental methods available that can fully resolve instantaneous spatial derivatives at such small scales. However, implementing Taylor's frozen turbulence hypothesis allows the spatial derivatives to be represented by time derivatives ([11]),

$$\left\langle\left(\frac{\partial u_i}{\partial x_i}\right)^2\right\rangle = \frac{1}{\overline{U_i}^2}\left\langle\left(\frac{\partial u_i}{\partial t}\right)^2\right\rangle$$

This relationship can be used to determine the dissipation rate ([12]),

$$\varepsilon = \frac{15\upsilon}{\overline{U_o}^2}\left\langle\left(\frac{\partial u_i}{\partial t}\right)^2\right\rangle \qquad \textbf{2.16}$$

With kiloHertz levels of time resolution, our experimental method permits the accurate estimation of time derivatives. Dissipation rates are calculated using Equation 2.16.

## Digital Particle Image Velocimetry

The results presented herein were generated using Particle Image Velocimetry (PIV). During the past two decades, numerous publications have appeared presenting improvements on the PIV method. Applications of the method range from low-speed liquid and two-phase flows to supersonic gas flows. Review articles by [13]; [14], [15] and [16] provide comprehensive summaries of the principles of the method and its various applications. The work of [17], [18], [19], [20] and [21] established the digital implementation of PIV, namely DPIV. The applicability of the method in resolving a variety of length scales in the flow has been

investigated by [22]. Despite the advances in improving the spatial resolution and accuracy of the method, conventional DPIV systems provide a limited temporal resolution (~30Hz), which is insufficient for resolving the fluctuations present in a turbulent flow field. For moderate Reynolds numbers ($10^3$-$10^5$) and small length scales, which are common in a laboratory environment, the sampling frequency necessary in order to resolve adequately the turbulent characteristics of the flow is indeed in the order of $10^3$ Hz. The system developed by the present team extends the range of time resolution to this range of frequencies.

Past implementation of time-resolved systems employed digital sensors with limited resolution ([23]) or drum cameras that are limited both in recording times as well as frame rate ([24]). Recent work by [25] presented an analog based kilohertz frame rate PIV system capable of recording up to 4000 fps. By employing analog recording, the system delivers superior spatial resolution (>1Kx1K), however due to the fact that such high frame rates require extreme rotation speed for the film, the registration of the images is compromised by film alignment errors that are added on the common digitization errors. Super resolution, iterative, and hybrid DPIV algorithms were developed in order to carry out the task of the velocity evaluation by [26], [27], [28] and [29]. Finally, several implementations of the method demonstrated its applicability in two-phase and multi-phase flows [30] and [31].

Previous work by the present team ([32]) presented a fully digital system with 1 KHz sampling rate , which however was limited to 256x256-pixel resolution. More recently we presented time resolved DPIV (TRDPIV) measurements with kHz sampling rate in multi-phase flows ([33]) and provided detailed error analysis ([34]) In the present effort we have improved upon the earlier works to employ a time-resolved DPIV system capable of resolving multi-phase flows with ~1kHz sampling rate and enhanced spatial resolution on the order of 60μm.

## Facilities and Instrumentation

Experiments to characterize the particle and bubble response to turbulence were performed. A small-scale water tunnel has been constructed in which we generated homogenous isotropic turbulence (Figure 2.1). The design allows quick change of the fluid/particle mixture and flushing of the system for more tests. The facility is appropriate for mixing different sizes of particles with different densities, as well as generating air bubbles of different sizes using capillaries. Turbulence is generated by a grid of circular cylinders 1 cm in diameter, spaced by 1 cm in both the length and width directions. This is the simplest reproducible and repeatable example of homogeneous turbulence. On the other hand, the space immediately above the cylinders displays a range of large turbulent structures that simulate the turbulent flow in a flotation column or above the impeller of a flotation cell.

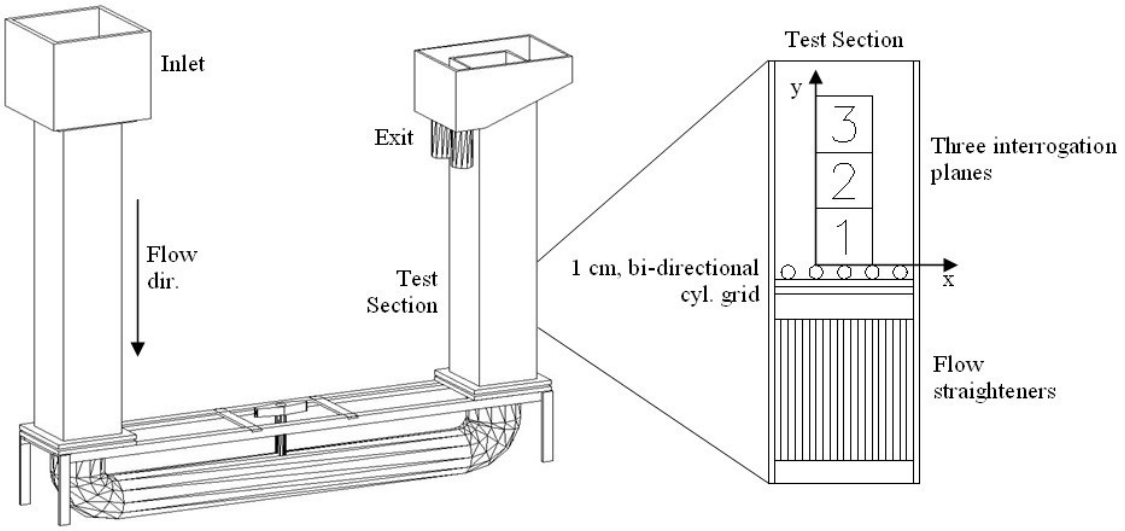


**Figure 2.1 - Schematic of water tunnel and expanded view of test section**

The Reynolds number based on the grid spacing was on the order of Re=1000. The Kolmogorov length scale is of the order of 50μm and the corresponding time scale was 100ms. This value of the Kolmogorov length scale was estimated approximately using the formula $\eta=L(Re)^{-3/4}$. The

experiments were performed with a sampling frequency of 1000 Hz ($\Delta t$=1ms) and a spatial resolution of 60μm/pixel. We could therefore resolve velocity variations almost down to the Kolmogorov scale, but our measurement method would fail to capture the smallest scales in regions of high turbulence dissipation where the Kolmogorov scale would be smaller. The DPIV data analysis scheme was optimized for the maximum spatial resolution with the minimum spatial averaging effects introduced by the cross-correlation. Therefore the velocity measurements were carried out with a minimum interrogation window of 8x8 pixels with 3 pixels (62%) overlap spacing between consecutive vectors. This results in spatial resolution for the flow field of the order of 180μm.

Non-invasive optical flow diagnostics measurements were performed in order to characterize the particle and/or bubble interactions within homogeneous isotropic turbulence. DPIV requires a plane sheet of intense laser light. This sheet cuts the domain along planes of interest. The DPIV component arrangement shown in Figure 2.2 records the instantaneous flow field in a plane. In the present case the plane of interest is vertical and parallel to the x-y plane as shown in Fig. 1. Data were collected along three square sections, each with sides equal to 4 cm, or 4L. The length scale L was chosen to be equal to one rod diameter. The origin of the coordinate system is at the lower left corner of the domain of measurements, as shown in Figure 2.1. We employ a digital camera to record the instantaneous position of different objects in the flow field. Recording the position of seed particles that follow the flow allows us to calculate the instantaneous flow velocity field. Over the past few years, we were able to improve this method by increasing the frequency response by two orders of magnitude over commercially available systems. We have also employed this method to record two-phase flows, namely spray flows or bubbly flows.

Digital Particle Image Velocimetry (DPIV) is the most established global flow-field measurement technique. However, time-resolved measurements with simultaneous velocity, shape and size characterization of multiple phases remains a great challenge. In the current effort, we integrate the appropriate hardware and software components necessary to perform such measurements. A CMOS (complementary metal oxide semiconductor) Vision Research Phantom-IV camera with frame rate up to 1000 frames per second (fps) and spatial resolution of 512x512 is employed using single exposure per frame for the recording of the DPIV images. The camera is synchronized with a high repetition rate Copper–vapor pulsing laser with emission wavelengths at 511nm and 578nm. The pulse duration is of the order of 25nsecs, sufficient for performing measurements for low and moderate speeds.

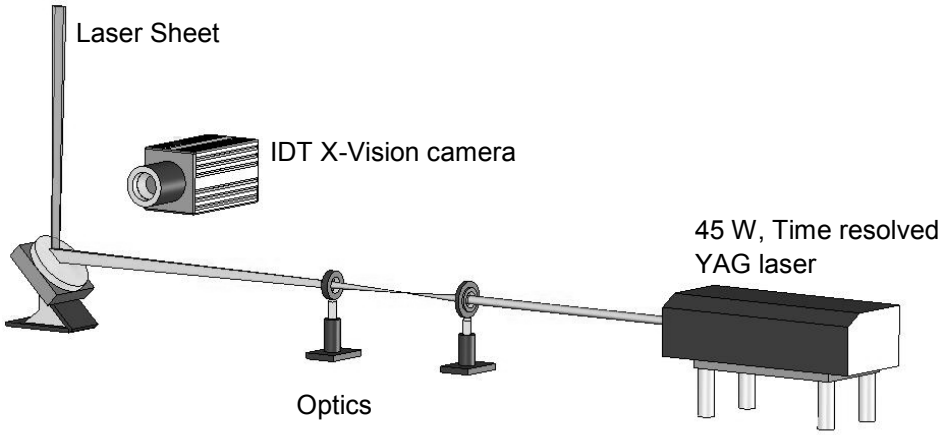


**Figure 2.2-View of a typical DPIV experimental setup**

For multiphase flows, saturation of the image from overexposure of bubbles or droplets is detrimental to the process of carrying out accurate quantitative measurements of size and position. Conventional DPIV systems employ CCD (charged coupled device) cameras, which

suffer from leakage effects, namely, the excessive charge from overexposed pixels leaks to the neighboring ones saturating the whole area. In contrast, CMOS sensors isolate the individual pixels behaving as a cut-off filter without leaking the energy. Therefore, by employing CMOS technology we eliminate the leakage effect, allowing resolution of a multi-phase flow with direct imaging within a laser sheet. This feature is of great importance, since it simplifies the experimental setup, enhances the signal-to-noise ratio, and more importantly allows accurate shape and size quantification of particles or bubbles present in the flow. In addition, it improves the performance of the position estimator, which is essential for the performance of the particle tracking methodology. Details on the performance characteristics and accuracy of the system can be found in Abiven and Vlachos (2002).

Traditional, cross-correlation-based PIV data-processing software was used to determine the flow velocities. This requires relatively dense seeding, namely at least 5 to 8 seed particles in each interrogation window. Because model particles and bubbles appear more sparsely in the images, they were measured using another processing technique, namely Particle Tracking Velocimetry (PTV). PTV tracks individual particle locations over multiple frames from which velocities can be determined with any order of accuracy desired. PTV allows us to measure $\overline{(U_i^2)}_{abs}$, and $\overline{U_i^2}$ experimentally, where i takes the values 1 or 2, for solid particles or bubbles respectively. The kinetic energy dissipation rate was calculated using traditional, cross-correlation-based PIV, providing a means to calculate $\overline{(U_i^2)}_{abs}$ and $\overline{U_i^2}$ from the models in Equations 2.10-2.14.

## RESULTS

Very small particles characterized by Stokes numbers less than 1 behave as fluid elements, responding to all the fluctuations of the flow. The $U_{rms}$ corresponding to the particle motion is defined by the velocity at the level of the Kolmogorov micro-scale for homogeneous isotropic turbulence, namely, $(\varepsilon\nu)^{1/4}$. Figure 2.3 shows two sample images over the range y/L=0-4, just above the turbulence grid and the resulting velocity field produced by cross correlation. The third frame in each row represents the instantaneous vector fields calculated. The first and second row present snapshots obtained with model particles and bubbles respectively. Figure 2.4 displays results averaged over 1,500 instantaneous frames. The color contours correspond to magnitudes of the quantity plotted. The region where data were obtained consist of the three square frames, centered over two of the grid rods as shown in Fig.1. Two jets issuing between each pair of cylinders are therefore captured in the lower frame. Immediately downstream of the grid the turbulence is not homogenous. Homogeneity and isotropy evolve as we move up and away from the grid. The time-averaged vorticity contours clearly show two regions of intense vorticity on either side of the jet. The dissipation rate was computed using Taylor's hypothesis of frozen-turbulence, namely Equation 2.16. Figure 2.4 clearly illustrates a leveling off of the dissipation rate beyond three grid lengths.

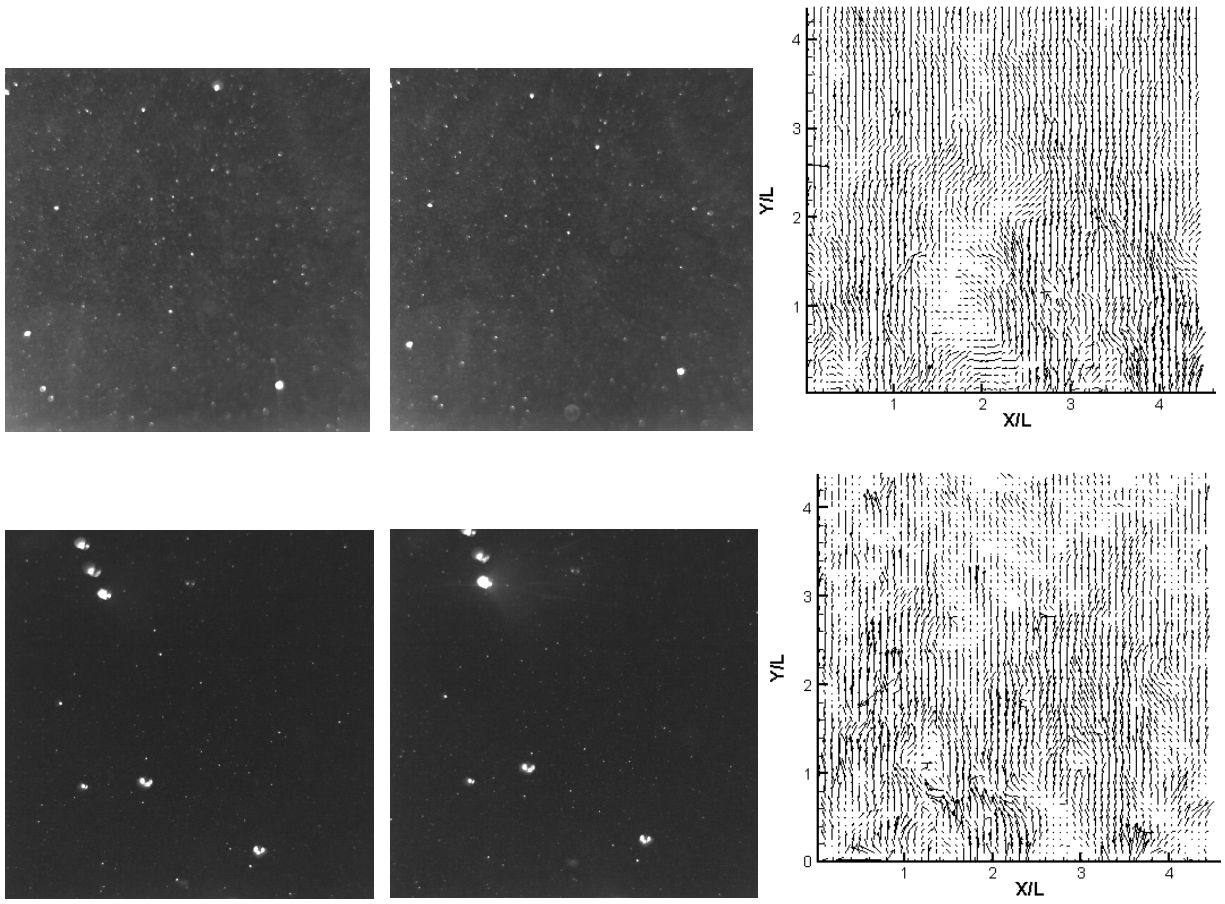


**Figure 2.3 - Two sample images with 80 μm solid particles and flow tracers (top row), and 1.2 mm bubbles and flow tracers (bottom row) separated by 0.001 sec and corresponding velocity field from cross correlation**

The average dissipation rate in each of the three frames above the grid was estimated by averaging the measurements of Figure 2.4 to obtain about 3, 0.8 and 0.4 dimensionless dissipation units. With tunnel velocity of 0.14 m/s and length scale L=0.01 m, these rates correspond to about 5.9, 1.57 and 0.70 $m^2/s^3$, respectively. These values are considerably lower than those encountered near the impeller of flotation machines ([35]). To satisfy the one-second criterion of suspending solid particles ([7]), the average specific power of such machines is about 1 or 1.5 $Kg/m^3$. But the energy dissipation in the immediate vicinity of the impeller can be 50 to 200 times larger. Our data therefore were obtained with turbulence levels corresponding to regions far from the impeller of a flotation machine, or to flow in flotation cells. We are

presently repeating these measurements in stirring tanks with much larger levels of turbulence dissipation. These results will be reported in a subsequent publication.

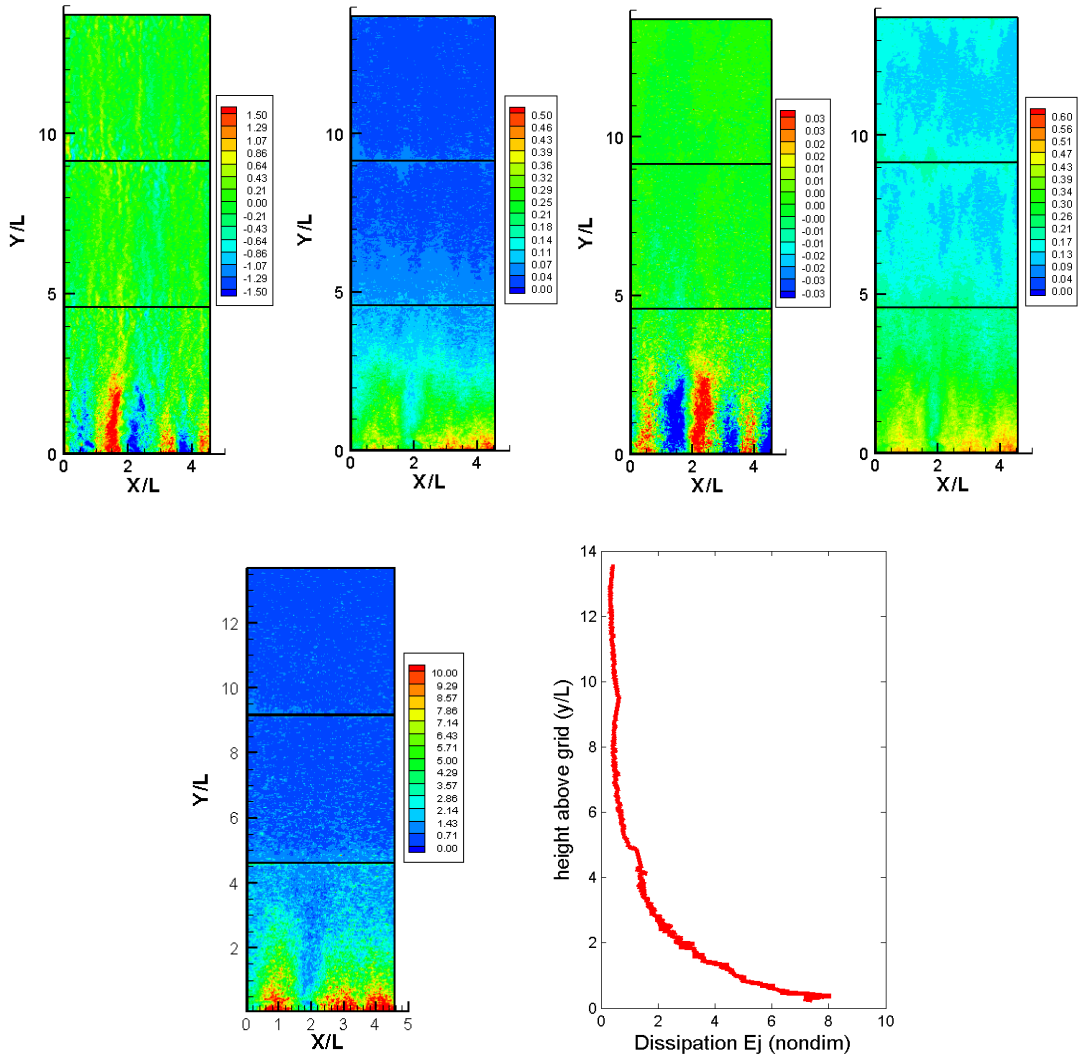


**Figure 2.4 - Time averaged results of three interrogation planes (all nondimentionalized by Uo and L) downstream of the turbulence grid over a length of approximately 14 grid spacings. From left to right and top to bottom : vorticity, turbulent kinetic energy, Reynolds stresses, Vrms, dissipation, and dissipation averaged over time and x. Dissipation is normalized by $Uo^3L^{-1}$**

Particle Tracking Velocimetry (PTV) was utilized to track the positions of the 80-μm glass particles. Figure 2.5 shows particle trajectories at three regions above the turbulence grid tracked for 50 frames. These three frames were obtained by zooming in to the frames shown in Figure

2.1 - Schematic of water tunnel and expanded view of test section, and the units on the axes are in number of pixels of the camera. The circles represent the location and diameter of each particle measured by PTV. The size of the particle appears to be changing with time. This is because the particle is going through the laser sheet with a Gaussian intensity profile. An estimate of the size of the particle is therefore the largest diameter recorded along a trajectory. The region just above the turbulence grid shows a domain of unsteady but coherent motion, especially on the extreme left and right of the image, which are in the immediate downstream region over each rod. Flow reversal in the wake of the rods is evident. Further above the grid at y/L=4-6, the particle accelerations are not as severe; however large-scale fluid motion is now evident. Finally, in the region y/L=10-12 above the grid, small scale turbulence is the only noticeable type of particle fluctuation.

### Comparison of models

In Figure 2.6 to Figure 2.8 we present experimental data and analytical predictions along the height of the measuring domain, which covers different levels of the dissipation rates. The analytical predictions were calculated in terms of dimensionless expressions shown in Table 1. Using the experimental dissipation rate estimates, the predicted RMS velocities of the 80-μm particles were calculated and compared to the measured RMS velocities of the particles obtained via the Particle Tracking algorithm. Figure 2.6 indicates that the RMS slip velocity measurements agree well with those predicted by the Liepe-and-Möckel model. The RMS velocities do not deviate from the experimental results by more than 12% over the region of interest. The model of Levins and Glastonbury underestimated the particle RMS by about 50% in the fully-developed flow region (y/L>8). Figure 2.7 shows the absolute particle RMS velocity and the corresponding predictions from Abrahamson and Williams and Crane. Abrahamson's

model provides a reasonable estimate (18% mean error) in the fully developed region. The Williams and Crane model did not provide a good prediction, generating a 40% mean error.

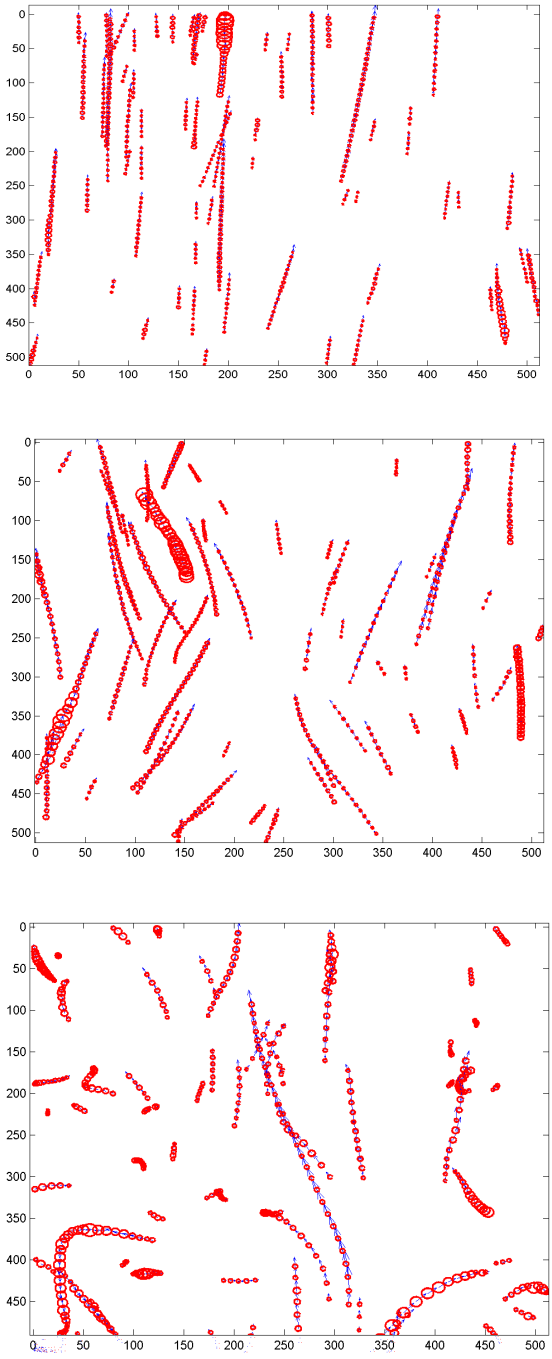


**Figure 2.5 - – Trajectories of 80 μm particles: bottom y/L=0-2 grid lengths, middle y/L=4-6, top y/L=10-12. Units on the axes are in number of pixels**

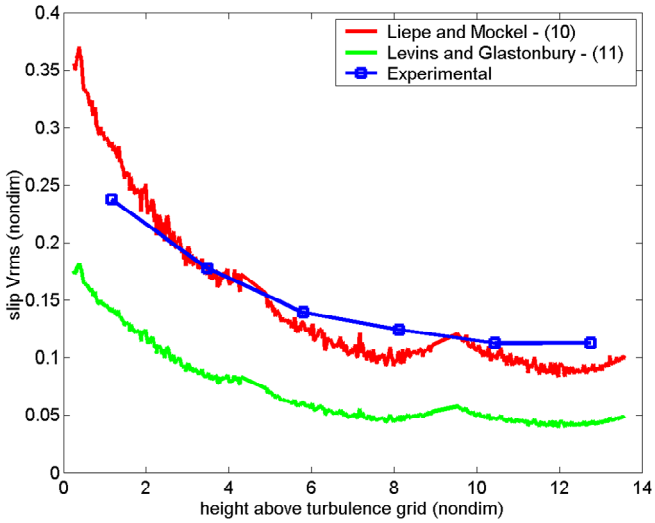


**Figure 2.6 - RMS of slip velocity versus height above turbulence grid of 80 μm particles and corresponding predictions from models. Equations numbers are shown in Table 2.1**

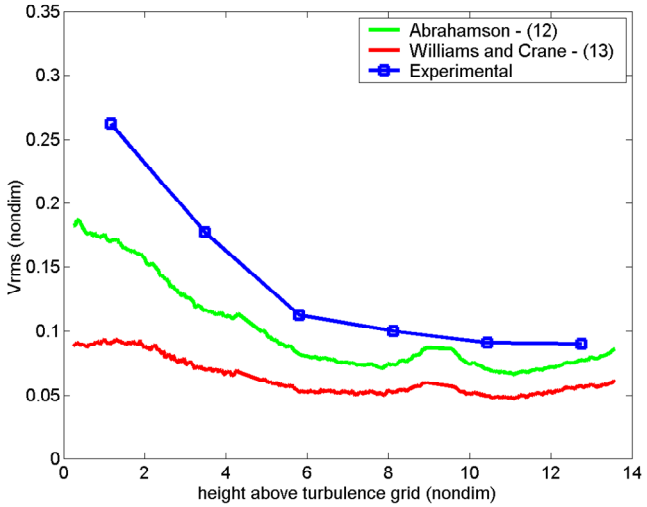


**Figure 2.7 - RMS velocity versus height above turbulence grid of 80 μm particles and corresponding predictions from models. Equations numbers are shown in Table 2.1**

The bubble RMS slip velocity, shown in Figure 2.8 is significantly higher than the particle RMS by about 100% in the homogeneous isotropic region, indicating relatively large fluctuations compared to the flow. Liepe and Möckel's empirical model, although not developed for the case of bubbles is shown along with the Levins and Glastonbury model. Both models overestimate the bubble RMS with the Levins and Glastonbury model providing a better prediction with a mean error of 22%. Figure 2.9 shows the results of the other models. Results obtained with the Abrahamson and the Williams and Crane models are in good agreement with the measured bubble RMS (13% and 12% mean errors, respectively). The model developed by Lee et al. provided the poorest estimates of the bubble RMS with a mean error of at least 350%.

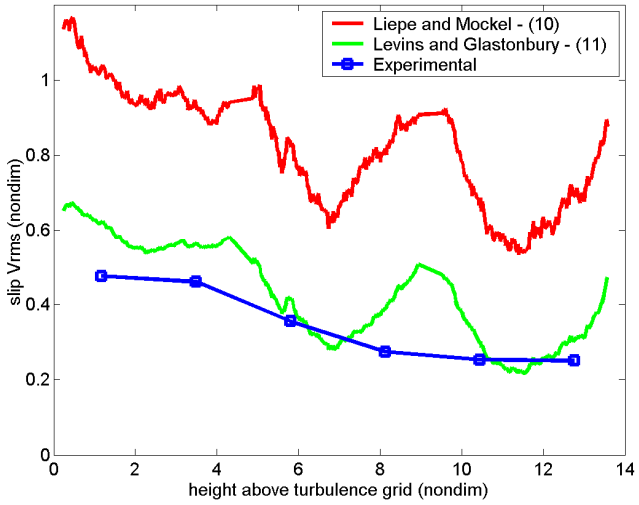


**Figure 2.8 - RMS of slip velocity versus height above turbulence grid of 1.2 mm bubbles and corresponding predictions from models. Equations numbers are shown in Table 2.1**

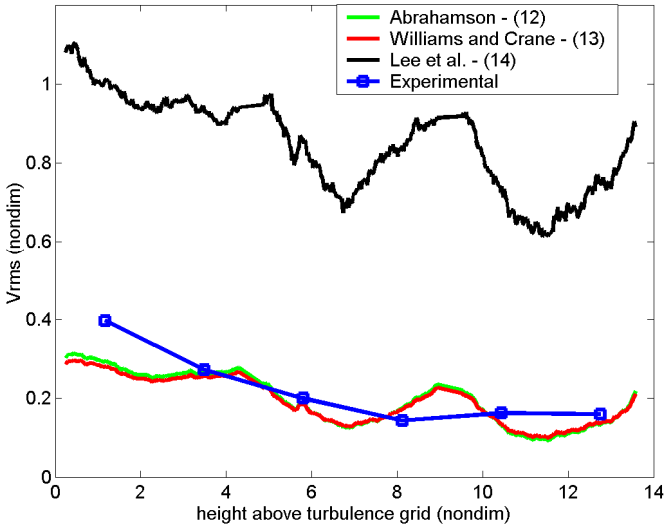


**Figure 2.9 - RMS velocity versus height above turbulence grid of 1.2 mm bubbles and corresponding predictions from models. Equations numbers are shown in Table 2.1**

The model of Liepe and Möckel is the only model derived from a large number of experimental data. Its validity as reported by the authors is limited by the inequality $d_i > 10\ \eta$, that is the particle diameter must be larger than ten Kolmogorov length scales. In the upper region of our experimental domain, this inequality is satisfied. The experimental data referenced and employed by Liepe and Möckel were collected manually, literally particle by particle, for thousands of particles. The element if human error is therefore a possibility. It is therefore useful to confirm the validity of the model in terms of data obtained with modern automated experimental methods. All the other models tested here are analytical models, each basd on different assumptions. It is not appropriated here to critisize their validity. We only present results to indicate their validity.

## CONCLUSIONS

A range of turbulence characteristics, including isotropic turbulence was created in a model flotation cell through turbulence grid. The turbulent dissipation rate was measured using a cross-correlation-based Particle Image Velocimeter. Particle Tracking Velocimetry was used to determine the velocity fluctuations of the solid particles and the bubbles relative to the fluid phase. RMS velocities of particles and bubbles were calculated and compared to experimental and theoretical models that are based on the turbulent dissipation rate. The particle RMS slip velocity was in good agreement with Liepe and Möckel's empirical model, demonstrating 12% mean error. A theoretical model, derived by Levins and Glastonbury was found to be in good agreement with the bubble RMS, but substantially underpredicted the RMS of the glass particles. In addition, the theoretical models derived by Abrahamson, and Williams and Crane provided good and almost identical agreement in predicting the RMS of the bubble velocity, but did not do as well in predicting particle fluctuations.

## REFERENCES


1. Ralston, J., et al., Flotation rate constant predition for metal sulfide particles. Centenary of Flotation 2005 Symposium, 2005.
2. Sherrel, I. and R.H. Yoon, Development of a Turbulent Flotation Model. Centenary of Flotation 2005 Symposium, 2005.
3. Liepe, F. and M. Hans-Otto, Untersuchungen zum Stoffvereinigen in Flüssiger Phase. Chem. Techn., 1976. 28(Jg., Heft 4).
4. Levins, B.E. and J.R. Glastonbury, Trans. Instn. Chem. Engr., 1972. 50(32): p. 132.
5. Saffman, P.G. and J.S. Turner, On the collision of drops in turbulent clouds. Journal of Fluid Mechanics, 1956. 1: p. 16-30.
6. Abrahamson, J., COLLISION RATES OF SMALL PARTICLES IN A VIGOROUSLY TURBULENT FLUID. Chemical Engineering Science, 1975. 30(11): p. 1371-1379.
7. Schubert, H., On the turbulence-controlled microprocesses in flotation machines. International Journal of Mineral Processing, 1999. 56(1-4): p. 257-276.
8. Lee, C.H., L.E. Erickson, and L.A. Glasgow, BUBBLE BREAKUP AND COALESCENCE IN TURBULENT GAS-LIQUID DISPERSIONS. Chemical Engineering Communications, 1987. 59(1-6): p. 65-84.
9. Williams, J.J.E. and R.I. Crane, PARTICLE COLLISION RATE IN TURBULENT-FLOW. International Journal of Multiphase Flow, 1983. 9(4): p. 421-435.
10. Brady, M., et al., Turbulent Bubble Particle Interactions Measured by Particle Image Velocimetry. Society of Mining Engineer, 2004(04:193).
11. Sheng, J., H. Meng, and R.O. Fox, A large eddy PIV method for turbulence dissipation rate estimation. Chemical Engineering Science, 2000. 55(20): p. 4423-4434.
12. Hinze, J.O., Turbulence. 1994: McGraw-Hill, Inc: New York.
13. Hesselink, L., DIGITAL IMAGE-PROCESSING IN FLOW VISUALIZATION. Annual Review of Fluid Mechanics, 1988. 20: p. 421-&.
14. Adrian, R.J., PARTICLE-IMAGING TECHNIQUES FOR EXPERIMENTAL FLUID-MECHANICS. Annual Review of Fluid Mechanics, 1991. 23: p. 261-304.
15. Grant, I., Selected papers on Particle Image Velocimetry. SPIE Milestone Series MS99, SPIE Optical Engineering Press, Bellingham, WA., 1994.

16. Grant, I., Particle image velocimetry: A review. Proceedings of the Institution of Mechanical Engineers Part C-Journal of Mechanical Engineering Science, 1997. 211(1): p. 55-76.
17. Willert, C.E. and M. Gharib, DIGITAL PARTICLE IMAGE VELOCIMETRY. Experiments in Fluids, 1991. 10(4): p. 181-193.
18. Westerweel, J. ANALYSIS OF PIV INTERROGATION WITH LOW PIXEL RESOLUTION. in Conference on Optical Diagnostics in Fluid and Thermal Flow. 1993. San Diego, Ca.
19. Westerweel, J., Digital Particle Image Velocimetry, Theory and Application. 1993: Delft University Press, Delft, The Netherlands.
20. Huang, H.T. and M. Gharib, Processing error in digital particle image velocimetry. ASME FEDSM 1997:3068, 1997.
21. Huang, H., D. Dabiri, and M. Gharib, On errors of digital particle image velocimetry. Measurement Science & Technology, 1997. 8(12): p. 1427-1440.
22. Adrian, R.J., Dynamic ranges of velocity and spatial resolution of particle image velocimetry. Measurement Science & Technology, 1997. 8(12): p. 1393-1398.
23. Whybrew, A., et al., Two techniques for all-digital time-resolved PIV, in Third International Workshop on Particle Image Velocimetry. 1999: Santa Barbara.
24. Lecordier, B. and M. Trinite, Time resolved PIV measurements for high speed flows. Third International Workshop on Particle Image Velocimetry, Santa Barbara, Sept. 1999, 1999.
25. Upatnieks, A., K. Laberteaux, and S.L. Ceccio, A kilohertz frame rate cinemagraphic PIV system for laboratory-scale turbulent and unsteady flows. Experiments in Fluids, 2002. 32(1): p. 87-98.
26. Scarano, F. and M.L. Riethmuller, Iterative multigrid approach in PIV image processing with discrete window offset. Experiments in Fluids, 1999. 26(6): p. 513-523.
27. Guezennec, Y.G. and N. Kiritsis, STATISTICAL INVESTIGATION OF ERRORS IN PARTICLE IMAGE VELOCIMETRY. Experiments in Fluids, 1990. 10(2-3): p. 138-146.
28. Cowen, E.A. and S.G. Monismith, A hybrid digital particle tracking velocimetry technique. Experiments in Fluids, 1997. 22(3): p. 199-211.

29. Wereley, S.T. and C.D. Meinhart, Second-order accurate particle image velocimetry. Experiments in Fluids, 2001. 31(3): p. 258-268.
30. Boedec, T. and S. Simoens, Instantaneous and simultaneous planar velocity field measurements of two phases for turbulent mixing of high pressure sprays. Experiments in Fluids, 2001. 31(5): p. 506-518.
31. Khalitov, D.A. and E.K. Longmire, Simultaneous two-phase PIV by two-parameter phase discrimination. Experiments in Fluids, 2002. 32(2): p. 252-268.
32. Vlachos, P.P., A spatio-temporal analysis of separated flows over bluff bodies using quantitative flow visualization, in Department of Engineering Science and Mechanics. 2000, Virginia Polytechnic Institute and State University: Blacksburg, VA.
33. Abiven, C. and P.P. Vlachos, Super spario-temporal resolution, digital PIV system for multiphase flows with phase differentiation and simultaneous shape and size quantification. Int. Mech. Eng. Congress, New Orleans, LA, 2002.
34. Abiven, C., P.P. Vlachos, and G. papadopoulos, DPIV Strategies for resolving high shear and vortical flows. ASME Int. Mech. Eng. Congress, New Orleans, LA, 2002.
35. Schubert, H. and C. Bischofberger, On the microprocesses air dispersion and particle-bubble attachment in flotation machines as well as consequences for the scale-up of macroprocesses. International Journal of Mineral Processing, 1998. 52(4): p. 245-259.

# Chapter 3: Turbulence characteristics in a Rushton stirring vessel measured via time resolved DPIV

This manuscript has not yet been submitted for publication

Michael Brady[1] and Pavlos P. Vlachos[2]
[1]Department of Engineering Science and Mechanics
[2]Department of Mechanical Engineering
Virginia Polytechnic Institute & State University
Blacksburg, VA 24060 USA

## ABSTRACT

Time-resolved DPIV was used to measure the turbulent velocity field in a Rushton turbine near the impeller region. The range of Reynolds numbers investigated varied from 20,000 to 50,000. The flow in the impeller stream of a Rushton impeller can be best summarized as a radial jet with a pair of convecting tip vortices. The turbulence quantities were found by removing the periodic component from the blade passing, which is a dominant part of the measured velocities near the impeller. We provide evidence that larger, biased dissipation and turbulent kinetic energy values are estimated in the vicinity of the impeller due to the periodic component of the blade passage. The dissipation in the impeller stream showed decreasing trends with the Reynolds number, partly due to decreasing spatial resolution compared with the Kolmogorov length scale. The flow was found to be anisotropic close to the impeller. Vortex detection revealed that the tip vortices travel in a nearly radial direction from the impeller for small Reynolds numbers and in more erratic directions for higher Reynolds numbers. Other normalized turbulence quantities, namely Reynolds stresses and vorticity are found to scale nearly as a constant with Reynolds number.

## INTRODUCTION

There is a wealth of experimental and numerical results of the turbulent characteristics of the flow in stirring tanks. These are cylindrical tanks in which a stirring device generates turbulence. Stirring tanks are widely used in a large number of industrial applications to promote blending, chemical reaction, micro mixing etc. Industry needs suitably designed stirring vessels to increase production, product quality and reduce maintenance costs. Mixing processes are very important elements in many industrial devices, but at the same time they involve complex flow interactions, since in most cases, the flow is turbulent over the entire volume and strongly inhomogeneous and anisotropic.

The flow in mixing vessels is typically generated with rotors or impellers. The impeller agitates the flow and creates shear characteristics in accordance with the requirements of the mixing process. Bladed impellers can cause strong gradients in the flow, which lead to turbulence and higher shear rates. As the rotor agitates the flow, recirculation regions form. Lamberto et. al. [1] showed that the flow field in the tank generated by flat-bladed turbines is divided in half, and creates two distinct toroidal regions above and below the impeller. They also noted that the two regions act as a barrier to mixing by increasing the blend time. Therefore, determining the flow field and its characteristic quantities (eg. turbulent kinetic energy dissipation rate and turbulent kinetic energy etc) is of great significance.

Researchers used a variety of methods to record velocity fluctuations in stirring tanks, such as hot wire velocimetry [2], laser-Doppler velocimetry [3-5], and more recently particle-image velocimetry [4, 6-8]. Wu and Patterson [5] performed an energy balance on measured turbulent kinetic energy over a control volume to obtain local values of turbulent dissipation. Rao and Brodkey[2] and Okamoto et al.[9] applied power spectrum methods, while others ([2] , [5] and

[10]) estimated the integral scale by integration of the auto-correlation function. Mununga et. al. [11] simulated the laminar flow in an unbaffled mixing vessel stirred by a solid disk rotor and a 4-blade impeller using the CFD package FLUENT.

Although mixing in stirring tanks has been extensively studied in the past years computationally and experimentally, our understanding of the underlying physics of energy transport and turbulent mixing is not yet complete. The main objective of the present study is to analyse the flow field with high temporal and spatial resolution to provide better understanding of the nature of mixing in a stirring vessel in which inhomogeneous anisotropic turbulence is present.

Although previous efforts provided valuable insight of the mixing process in Rushton tanks, no experimental effort has been directed at resolving the global character of the flow with sufficient temporal resolution. Experimental efforts with high temporal resolution have been attempted [12], however was limited to a point measurements. The present effort addresses this issue by employing Time Resolved Particle Image Velocimetry (TRDPIV), allowing spatially resolved measurements with kHz sampling frequency. Thus both the spatial and temporal dynamics of the mixing process are revealed.

## Nomenclature

| | |
|---|---|
| $D$ | Tank Diameter [m] |
| $D_{imp}$ | Impeller Diameter [m] |
| $N$ | Impeller Rotational Speed[1/sec] |
| $Re$ | Reynolds Number |
| $u_i$ | Liquid Velocity in Direction i [m/sec] |
| $u_{tip}$ | Blade tip velocities [m/sec] |
| $u_i'$ | Fluctuating velocity component [m/sec] |
| $U_i$ | Mean velocity component [m/sec] |
| $w$ | Impeller Blade Width [m] |
| $w_b$ | Baffle width [m] |
| $\varepsilon$ | Turbulent kinetic energy dissipation rate [$m^2/sec^3$] |
| $f$ | Frequency [Hz] |
| $f_b$ | Frequency of impeller blade [Hz] |
| $\rho$ | Liquid Density [$kg/m^3$] |
| $r$ | Radial distance from center of impeller [m] |

| | |
|---|---|
| z | Vertical coordinate [m] |
| ν | Kinematic Viscosity [$m^2$/sec ] |
| ω | Vorticity [$sec^{-1}$] |
| η | Kolmogorov length scale [m] |
| M | Magnification [μm/pix] |
| $\Delta_d$ | Discriminant of the characteristic equation |
| $P$ | First invariant of the characteristic equation |
| $Q$ | Second invariant of the characteristic equation |
| $R$ | Third invariant of the characteristic equation |
| $D$ | velocity gradient tensor [m/s] |
| $\lambda$ | complex eigenvalue of the velocity gradient tensor |
| Δ | Spacing between vectors [m] |

## EXPERIMENTAL SETUP

The experimental apparatus used in this study consisted of a small-scale cylindrical, baffled stirring Rushton tank, made of Plexiglas with diameter D=0.1504m (6 inches) (shown in Figure 3.1). Four equally-spaced axial baffles with width ($w_b$) $1/10^{th}$ of the tank diameter (D) were mounted along the wall. A Rushton impeller with six blades was located at a height 0.0762m (D/2) from the bottom. The ratio between the vessel and the impeller diameter was $D_{imp}/D$ =1/3.The ratio of blade width ($w_i$) to the impeller diameter ($D_{imp}$) was 0.25. The tank was filled with deionized water as the working fluid. The height of the water was maintained at 0.1504 m, which is equal to the tank diameter. The cylindrical tank was housed in an outer rectangular container filled with water to eliminate the optical distortion of light passing through a curved boundary of media with different indices of refraction. In addition, a lid was placed on the setup on top of the baffles to prevent bubble entrainment from the free surface. Studies have shown [13] that the lid only affects the flow in the region very close to the lid/water interface and the velocities in the impeller stream region are virtually identical to the free surface case.

The Reynolds number $\mathrm{Re} = N \cdot D_{imp}^2 / \nu$ was based on the impeller diameter and the rotation speed. Furthermore, an estimation of the Kolmogorov length scale was based on $\eta = D_{imp} \cdot (\mathrm{Re})^{-3/4}$. Although, strictly speaking the Kolmogorov length scale is dependent on the

local dissipation rate by $\eta = \left(\nu^3/\varepsilon\right)^{0.25}$ , the aforementioned approximation provides a good estimate for comparing our resolution to the dissipation length scales.

This work is focused on the near impeller region where the turbulent mixing is generated and it is this region that exhibits the strongest velocity gradients and the largest velocity dynamic range. The interrogation area encompassed the rectangular region $0.2<r/D_{imp}<1$ and $-0.2<z/D_{imp}<0.2$. The laser sheet was focused on a plane of about 1mm thickness, parallel to the impeller shaft. Measurements were performed at six Reynolds numbers (Re) in the range 20,000-45,000 –shown in Table 3.1, corresponding to shaft rotational speeds of 529-1323 rpm and blade tip-velocities $u_{tip}$=1.4-3.52 m/sec. It should be noted that the shaft frequency is $1/6^{th}$ of the impeller blade frequency. All distances are normalized with the impeller diameter $D_{imp}$ and the velocities are normalized with the blade tip velocity, $u_{tip}$. The reference coordinate system is fixed at the center of the impeller. Each case contained 2000 images All of which were used for the time-accurate analysis of the data although 500 flow fields were used for the time-averaged results.

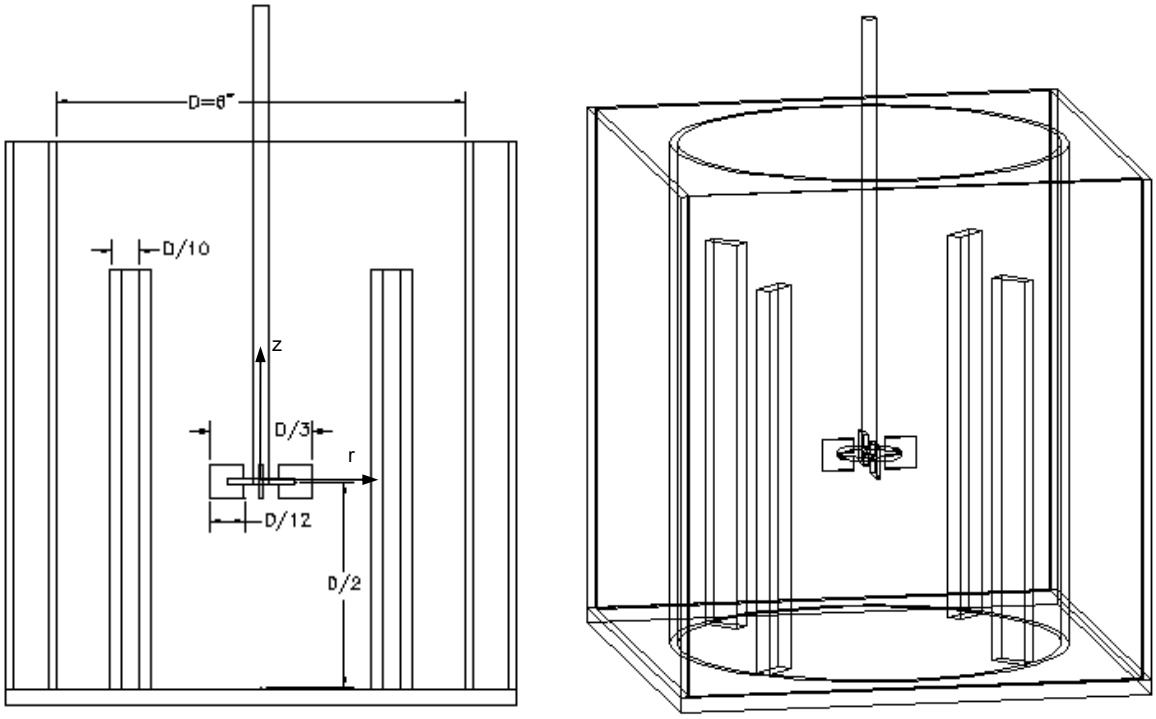


**Figure 3.1: Schematic and dimensions of the Rushton tank geometry.**

**Table 3.1 - Experimental parameters test matrix**

| Case | 1 | 2 | 3 | 4 | 5 | 6 |
|---|---|---|---|---|---|---|
| $10^3$Re | 20 | 25 | 30 | 35 | 40 | 45 |
| $u_{tip}$ (m/s) | 1.41 | 1.74 | 2.11 | 2.46 | 2.81 | 3.17 |
| $\eta$ ($\mu$m) | 30 | 26 | 22 | 20 | 18 | 16 |
| N (rev/sec) | 8.82 | 10.93 | 13.23 | 15.43 | 17.63 | 19.85 |

Digital particle image velocimetry [14-15] was used in order to resolve the character of the flow. In the present study we use an in-house developed time-resolved DPIV system capable of

delivering sampling frequencies on the order of 10 kHz, however due to spatial resolution requirements, the temporal resolution for this work was kept to 250 Hz. Since time and spatial resolution usually work inversely with each other in PIV systems, the spatial resolution was chosen to resolve small enough scales to accurately measure the turbulent dissipation rate (spatial gradient method). The temporal resolution was chosen to accurately resolve the impeller blade frequency.

The system is comprised of an IDT X-Stream camera. The camera is synchronized with a Lee-Lasers Nd-Yag pulsing laser with an emission wavelength of 532 mm. The pulse duration was in the order of 100 nsec, which is sufficient for performing measurements at low and moderate speeds. The laser was passed through a series of optics forming a 1mm light sheet that illuminated the area of interrogation. The flow was seeded with 8 μm diameter spherical, hollow glass flow tracers made with a specific gravity of 1.05. The optical setup was adjusted such that the particles registered an image of approximately 3x3 pixels. In-house developed PIV velocity estimation software [16-17] employing FFT-based cross-correlation with an iterative multi-pass scheme [18-19] with second-order discrete window offset [20-21] was used. The first pass interrogation window size was 32x32 pixels satisfying the ¼ rule for the maximum resolvable displacement. The window used in the discrete window offset pass ($2^{nd}$) was 16x16 pixels. This amounts to a 75% overlap between adjacent windows. Given the experimental setup, the spatial resolution (vector spacing) was about 128 μm. With the range of Reynolds numbers presented in this paper, the spatial resolution is larger than the Kolmogorov length scale by a factor of 8 for the largest Reynolds number, and about a factor of 4 for the lowest Reynolds number.

## RESULTS AND DISCUSSION

### Flow in the impeller stream

The focus of this study is primarily the turbulent characteristics in the impeller stream, however a short description of the mean flow will be discussed. An ensemble averaged view of the flow field is shown in Figure 3.2 for Re=20K. The impeller stream, in a time-averages sense can be described as a widening jet with decreasing peak radial-velocity as r increases. The radial jet, is not precisely radial. The jet is inclined about 4 degrees with the radial axis. This slight asymmetry in the ensemble averaged data is consistent with the results of other studies ([12]). The only geometric asymmetry in the tank is the impeller shaft. Therefore it is likely that the presence of the shaft is the cause of the slight inclination of the in plane velocity.

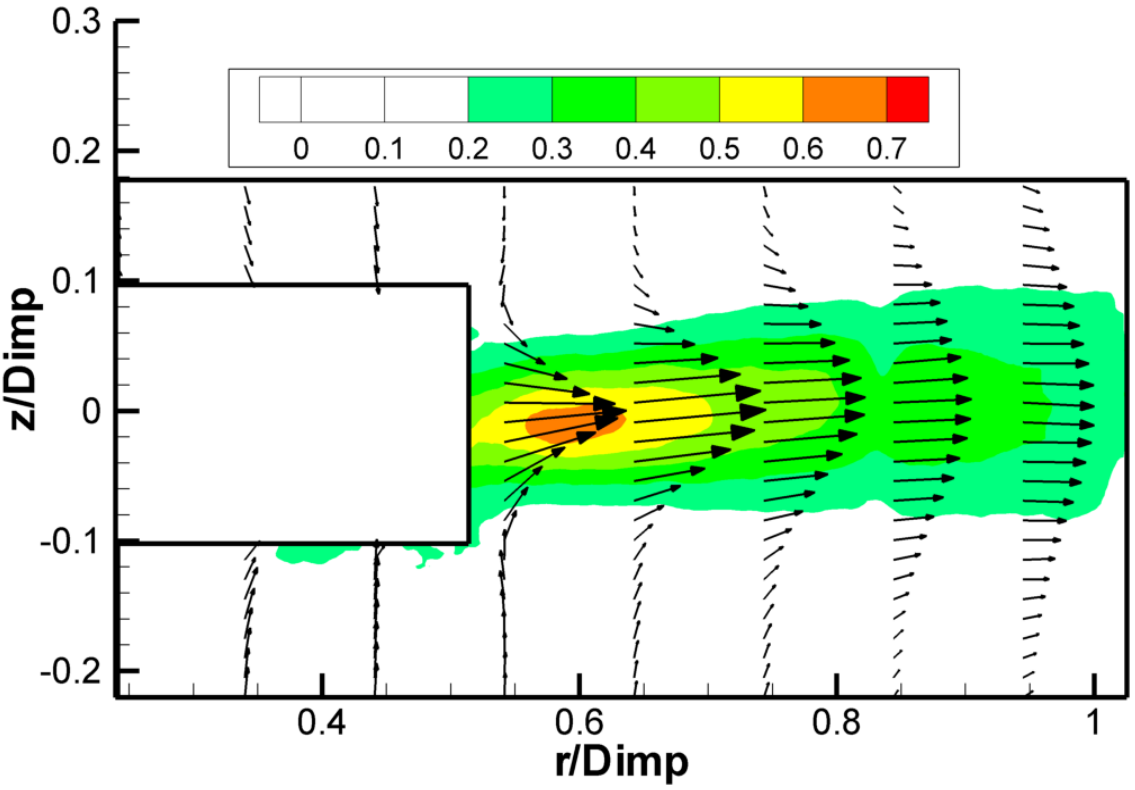


**Figure 3.2: In plane velocity vectors and velocity magnitude contours, $V_{mag}/u_{tip}$. Re=35K.**

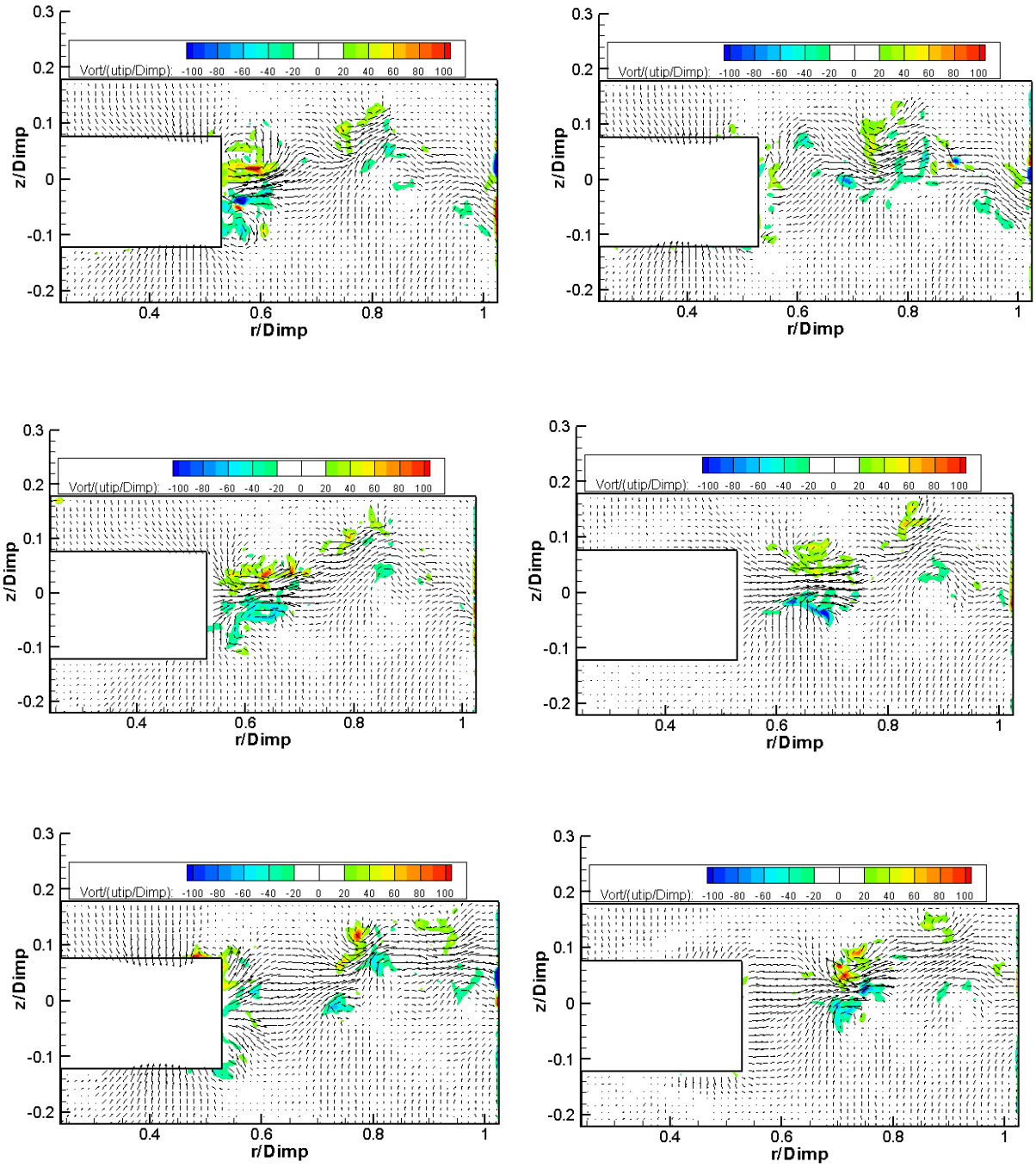


**Figure 3.3: (a)-(f) top to bottom, left to right. Instantaneous vorticity contours with vectors over one blade cycle. $\Delta t$=1/250 sec, $\Delta\phi$=10 degrees per frame**

The instantaneous velocity field over one blade cycle can be described as a radial jet along the impeller blade centerline, with a pair of tip vortices convecting out radially. A series of velocity field snapshots with vorticity contours are shown in Figure 3.3 over one blade cycle for the Re=20K case. The time elapsed between frames is 1/250 sec, corresponding to an angular displacement of a blade equal to about 10.0 degrees. This corresponds to about 36 frames per impeller revolution for the smallest Reynolds number. In these figures the passage of the blade is evident in terms of the large velocity magnitudes that persist for the entire sequence. Figure 3.3(a) is the start of the cycle when one of the impeller blades is parallel to the laser sheet ($\phi$=0 degrees), and continuing over a 60 degree blade cycle. In Figure 3.3 (f), a new set of tip vortices are generated, and the old pair that was generated in Figure 3.3 (a) is still convecting outward and noticeable broken down in size at $r/D_{imp}$=0.8. Apparently the flow is sustained for a certain period after the blade has cut through the plane of interrogation. The 2-D vortices shown are actually a vortex ring attached to each blade tip.

### Turbulence decomposition and spectra in the impeller stream

It is the purpose of this paper to classify the turbulence spatially and temporally. The instantaneous velocity can be expressed as,

$$u_r = U_r + u_r'$$
$$u_z = U_z + u_z' \qquad \textbf{3.1}$$

where $U_r$ and $u_r$' represent the mean and fluctuating velocity components of the radial velocity, and similarly for the z-component. Extracting U from the field is most effectively done by employing a narrow banded notch filter (band stop) to the velocity data. Others have used methods such as a simple ensemble averaged mean, or moving window averages. However, the

former does not effectively remove periodic variations in the flow (such as the blade in this case), and the latter tends to filter out turbulent frequencies unless the window size is carefully chosen. After utilizing the notch filter, the ensemble mean was subtracted from each velocity field, and the remaining velocities were assumed to be the turbulent fluctuations.

Separating the effect of the blade frequency and characterizing its impact on the turbulent statistics is important for the proper characterization of the turbulence in the tank. The relative effect of the periodic component to the true turbulent fluctuations can be determined by calculating the energy spectra. The energy spectra, E(f), is related to the variance of the velocity fluctuations by

$$\overline{u_i'^2} = \int_0^\infty E(f)df \qquad 3.2$$

The time and spatially resolved data allows us to compute the energy spectra at each point in the domain.

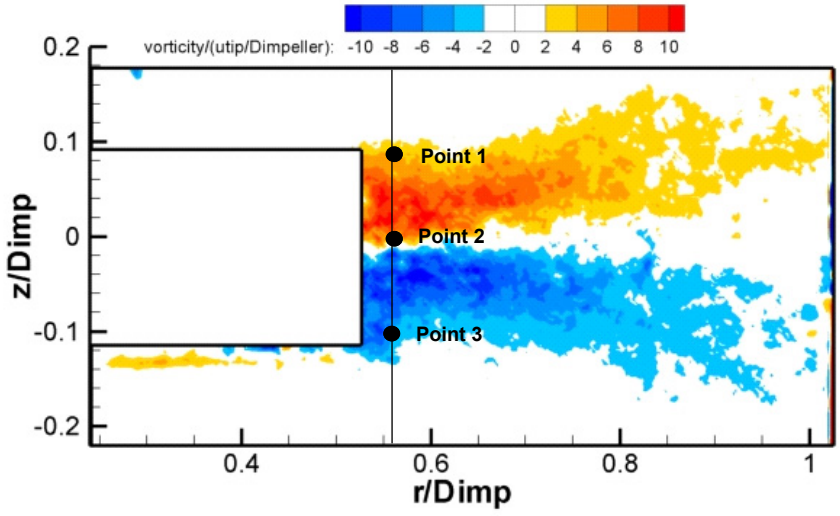


**Figure 3.4 Schematic showing locations of energy spectra. Line located at r/Dimp=0.56. Point locations are z/Dimp=(1.2,0,-1.2) respectively**

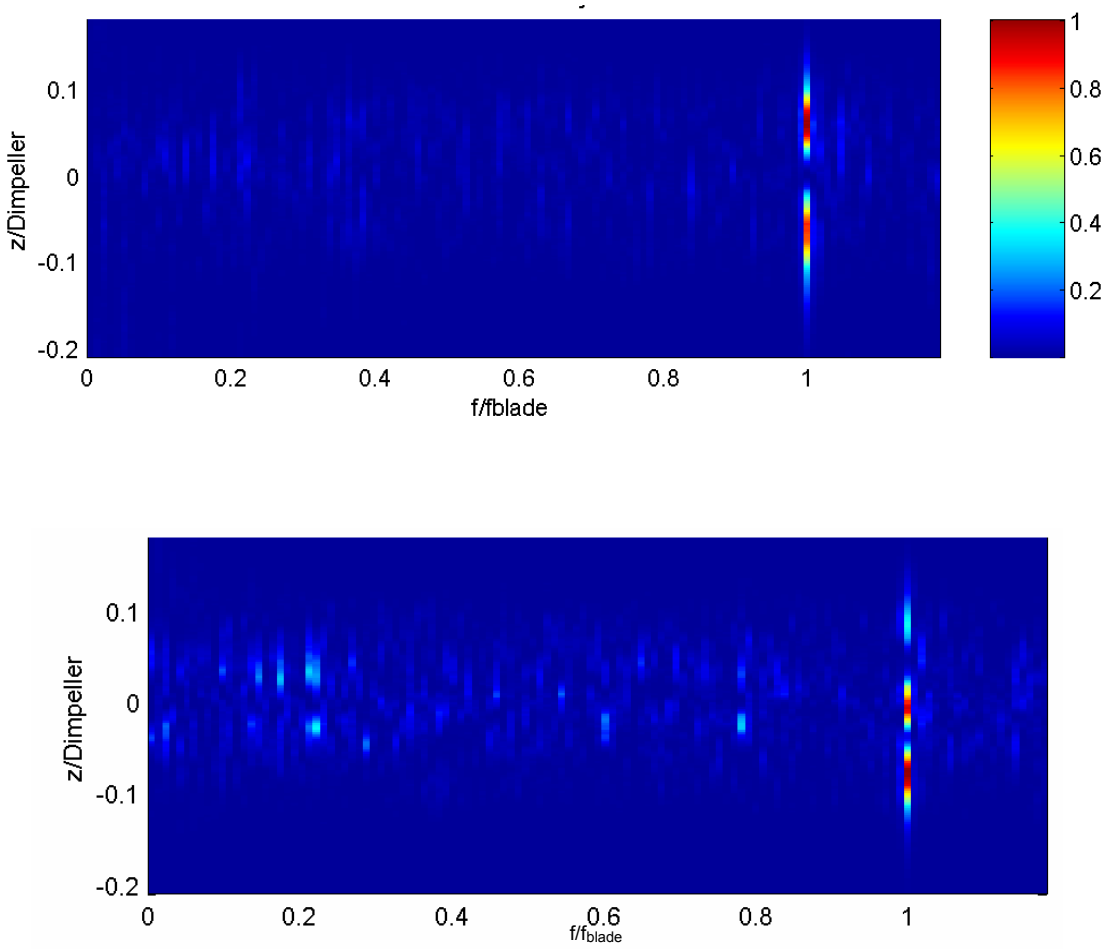


**Figure 3.5 normalized contours of Energy Spectrum of $u_z$ (top) and $u_r$ (bottom) , Re=40,000. frequency normalized with blade frequency. r/D=0.56**

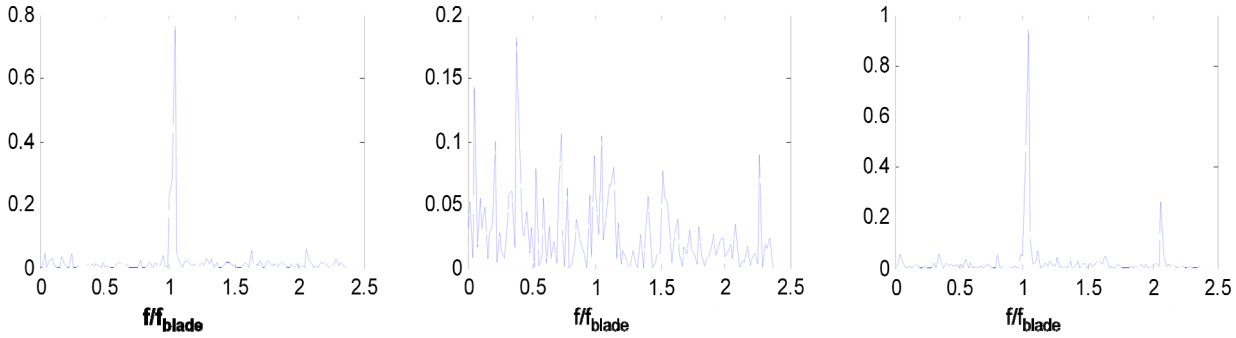


**Figure 3.6 (a), (b), (c) left to right. Energy Spectrum of uz, for Re=40,000. (a) corresponds to point 1 in Figure 4, (b) to point 2, and (c) to point 3**

The effect of the cyclic blade component can be seen in Figure 3.4 through Figure 3.6. Figure 3.4 shows a vertical line and three points corresponding to the locations of where the energy spectra shown in Figure 3.5 were calculated. Along the vertical line at each point, the energy spectrum was calculated and they are plotted as a contour plot in Figure 3.5 . The energy spectra were normalized with the total energy for relative comparison. Notice the difference between the energy spectra of $u_r$ and $u_z$. For $u_z$ two relative energy maxima at the blade frequency are shown, while for $u_r$ three peak locations are present. The two maxima in $u_z$ correspond to the tip vortices shedding at the blade frequency. The three maxima in $u_r$ also contain the tip vortices, but they also have a contribution from the radial jet at $z/D_{imp}=0$. Because the jet is primarily in the radial direction, there is no significant energy contribution from $u_z$ along the centerline.

The cyclic blade component of the velocity dominates the region very close to the impeller as just shown. To see how the impeller blade rotation affects the flow in the entire domain, the energy contained at the blade frequency was calculated at each point. These values were found by integrating the energy spectrum over the entire peak around the blade frequency. The results are shown in Figure 3.7. Figure 3.7(a), showing the effect on the radial velocity has a high-energy component along the centerline just next to the blade and is decaying with increasing r. In addition, there are high-energy regions around the corners of the impeller drawn in Figure 3.7(a), corresponding to the shedding of the tip vortices. Similarly, Figure 3.7(b), the energy at the blade frequency in the z-velocity component, shows the effects from the tip vortices. However, a low energy region along the centerline is noticeable. The radial jet along the centerline that is shed with each blade passing evidently does not deviate significantly from the radial direction. In addition, the areas above and below the impeller contain the highest energy values. This region is where the flow, after the passing of the impeller blade, rushes to fill in

behind the impeller blade with a high z-velocity component. This affect can also be seen in the snapshots of the flow shown in Figure 3.3 along the top and bottom of the impeller blade.

The total energy at the blade frequency for a given point does not give its relative importance to the signal. Therefore the relative affect of the impeller blade to the rest of the mean flow and the turbulence can be determined by calculating the energy spectrum as just shown, and then normalizing by the total energy at that point. This will determine the percentage of the total energy contained at the blade frequency at a given point. We will call this quantity the blade effect, BE. Mathematically this operation is:

$$BE = \frac{\int_{f_b-\Delta f}^{f_b+\Delta f} E(f)df}{\overline{u_i'^2}} \qquad \textbf{3.3}$$

where $\Delta f$ was chosen to be 2% of the Nyquist frequency. This included the entire peak around the blade frequency, but kept as small as possible. Figure 3.8 shows this result as a contour plot, for both velocity components, calculated at each point in the domain. It is clear that at the corners of the impeller, the blade frequency is significant, accounting for about 55% of the total energy in that region for the r-component and about 40-50% in the z-component. Figure 3.8 verifies the significance of the energy at the blade frequency around the impeller stream. The energy at the blade becomes less significant (drops to less than about 5% of the total energy) around r/Dimp=0.75 for the radial velocity component. However, this high-energy component only exists radially outward from the top and bottom corners of the blade. The area around the centerline, $-0.06<z/D_{imp}<0.06$ does not contain a significant energy component from the blade with exception of extreme close region of $r/D_{imp}<0.55$. The z-component tends to retain the effects from the blade longer as shown in Figure 3.8(b). The energy drops to about 7% of the

total at the blade around r/Dimp=0.85. The same absence of the rotating blade component along the centerline exists here as well. However the region is much narrower, extending from -0.02<z/$D_{imp}$<0.02. The decay of this frequency component indicates that the radial jet along the blade centerline, and the tip vortices have begun to develop into turbulence.

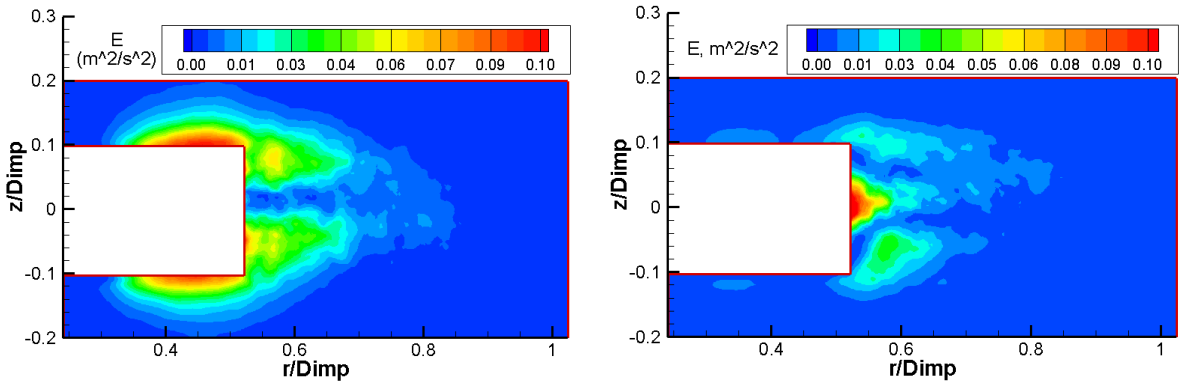


**Figure 3.7 Blade Effect for (a) left, radial velocity and (b) right, z-velocity, Re=20K**

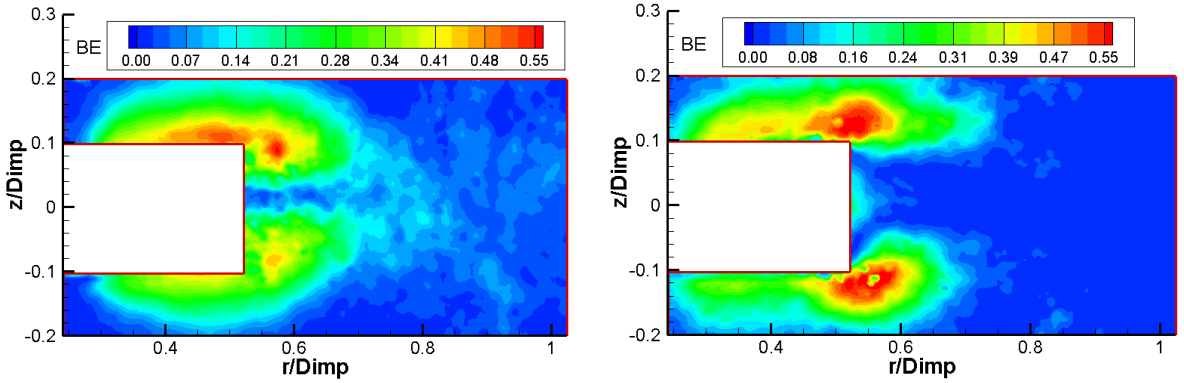


**Figure 3.8 - contained at the blade frequency for (a) left, radial velocity and (b) right, z-velocity, Re=20K**

It should be noted that the time resolution in this study is not sufficient to see the characteristic -5/3 turbulence slope. However, the time resolution is sufficient to remove the driving, periodic component in the flow, ie. the Nyquist frequency is well above that of the blade passage. The 250 Hz sampling frequency is about five times that of the blade rotational frequency for the case

of Re=20,000. The effect of this frequency component on the turbulent statistics will now be discussed.

### Effect of blade passage on turbulent statistics

The effects of the removal of the impeller blade frequency on the turbulent statistics will now be discussed. The turbulent kinetic energy, $k=u_r'^2 + u_z'^2$, is significantly affected by the blade frequency as shown in Figure 3.9 which is a contour plot of the percent drop in turbulent kinetic energy after the blade frequency component was removed. It is evident that immediately above and below the impeller, the removal of the periodic component resulted in about a 65% drop in k in that region. In addition, *k* is reduced by about 35% right next to the impeller (in the positive radial direction), and slowly the frequency component becomes less significant as the r increases. The effect of the blade quickly decreases and at $r/D_{imp}=0.84$, the blade frequency does not impact *k* significantly as shown in (b). This is in good agreement with the analysis of the energy spectrums in the preceding paragraph.

The affect of the blade frequency on the turbulent kinetic energy dissipation rate, ε (defined later by Equation 3.5), is less affected by the removal of the blade frequency as shown in Figure 3.10. However there still remains a significant drop in ε above and below the impeller after the removal as seen in the turbulent kinetic energy. In the impeller stream region (radially outward from the impeller), the effect of the blade frequency is on average about 12%. Figure 3.10(b) shows that the dissipation is less affected by the impeller blade. The difference in the total $u_r'u_z'$ and $u_r'\ u_z'$ with the blade component removed is shown in Figure 3.11. The cross term in the Reynolds stresses is not significantly affected except very near the blade passage, or beyond

r/Dimp = 0.7. For the remainder of the figures and the discussion, all turbulent quantities are presented with the blade frequency removed.

### Reynolds Stresses in the Impeller stream

A comparison of the three measured Reynolds stresses is needed to determine the degree of turbulence, and whether or not the turbulence is isotropic. Figure 3.12 shows the cross-term of the Reynolds stresses. The rms values reach a maximum very close to the blade, however not exactly adjacent to it, and then decrease with r. The cross term of the in-plane Reynolds stress, $u_r'u_z'$ (Figure 3.12 right) shows a dividing line between positive and negative values at the impeller blade centerline, consistent with previous results [7]. Figure 3.13 shows a comparison of the three Reynolds stresses. Very good agreement with [3] was attained when the values were normalized properly. Baldi and Yianneskis used a smaller diameter tank and placed their impeller 1/3 of the way from the bottom of the tank. In contrast, the impeller in this study was ½ of the way from the bottom of the tank to the free surface. The Reynolds stresses in Figure 3.13 (right) show a deviation from the Baldi and Yianneskis study. However because these values are so small in magnitude at the line compared (centerline), only a small difference in the z-value will change the results significantly as seen in the contour plot (Figure 3.12).

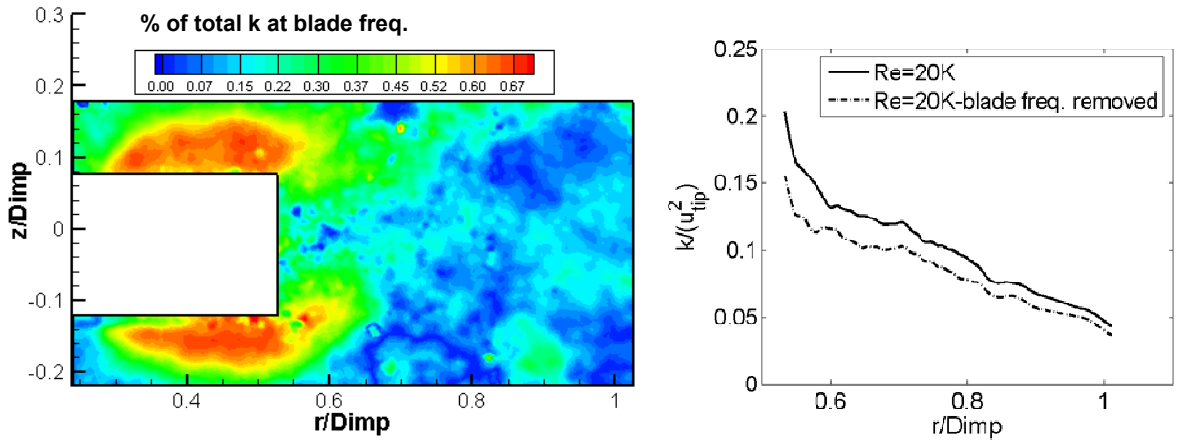


**Figure 3.9 a) top, percent of k at the blade frequency and (b) bottom, normalized k at (z/Dimp=0.05). Re=20K**

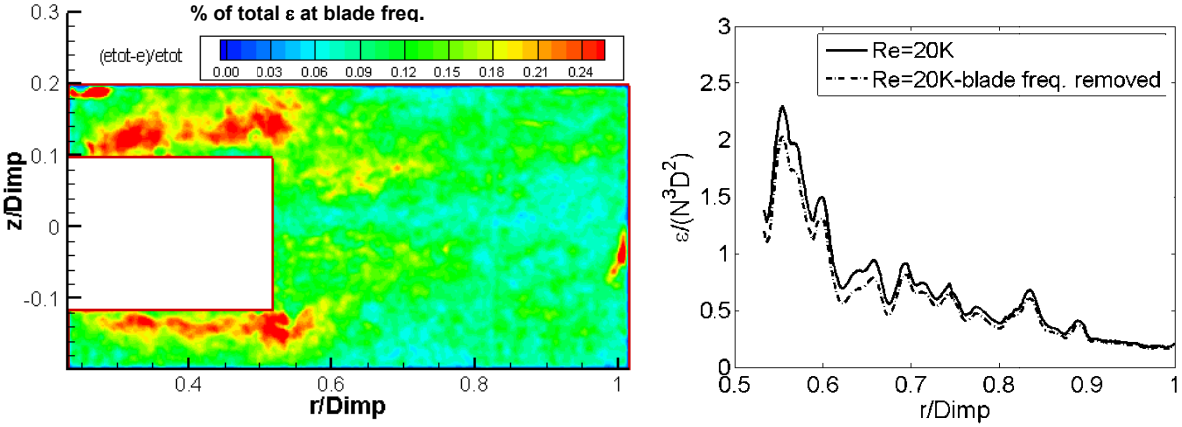


**Figure 3.10 (a) top, percent of ε at the blade frequency and (b) bottom, normalized ε at (z/Dimp=0.05) Re=20K**

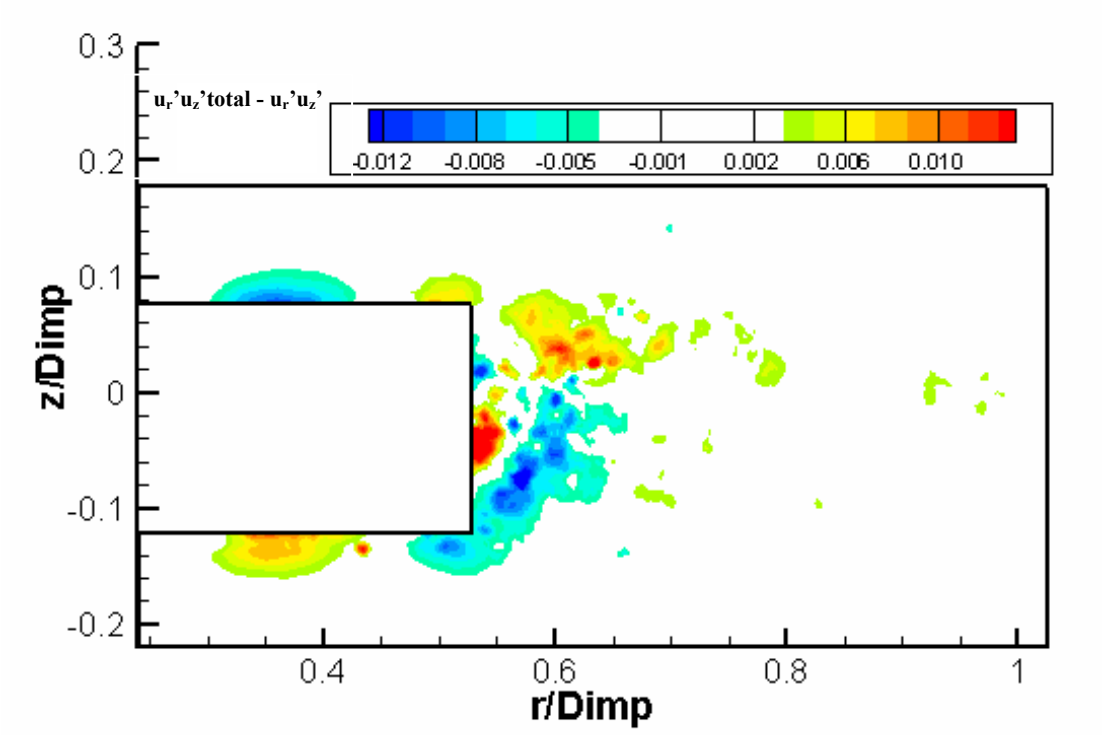


**Figure 3.11 Difference in $u_r'u_z'$ (nondim.) after removal of the impeller blade frequency**

The degree of isotropy can be analyzed by subtracting the various Reynolds stress values in each frame and then ensemble averaging at each point. Figure 3.14 left shows the difference in the $u_r'$ and $u_z'$ rms values. It is evident that directly above and below the impeller blade, and along the centerline in the impeller stream, the difference is considerable. The difference in these regions is about 0.12. This difference is more significant in the regions above and below the impeller, due to the relatively smaller magnitudes of the rms values in that region. Around $z/D_{imp}$=0.8, the difference becomes negligible. The differences between the two diagonal Reynolds stress values and the square root of the magnitude of the off diagonal term, $u_r'$ $u_z'$ are also shown in Figure 3.14.

## Dissipation in the impeller stream

The turbulent kinetic energy dissipation rate may be the most important quantity in a mixing machine. For turbulent flows, the turbulent kinetic energy dissipation rate is generally much more significant than the dissipation from the mean flow. Therefore only the turbulent dissipation will be addressed here. The normalization of the dissipation was done using $N^3D_{imp}^2$. This number has been shown to provide less scatter in the data published by the many authors using varying geometries and Reynolds numbers.

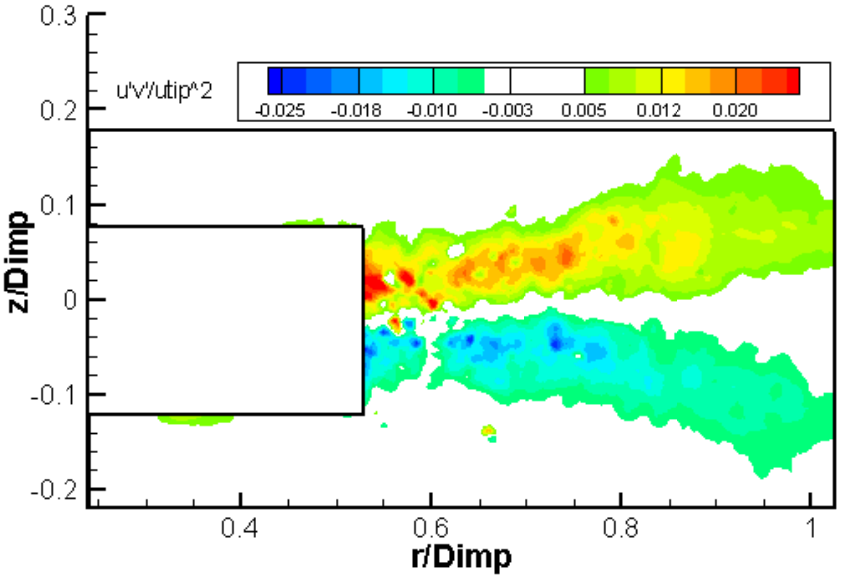


**Figure 3.12 Averaged Reynolds stresses $u_z$' $u_r$'**

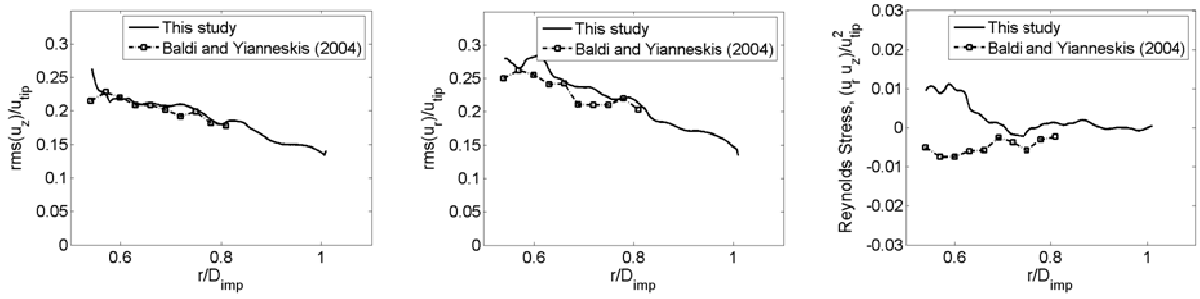


**Figure 3.13 Comparison of Reynolds stresses with another experimental study, (a) left, (b) right, (c) right**

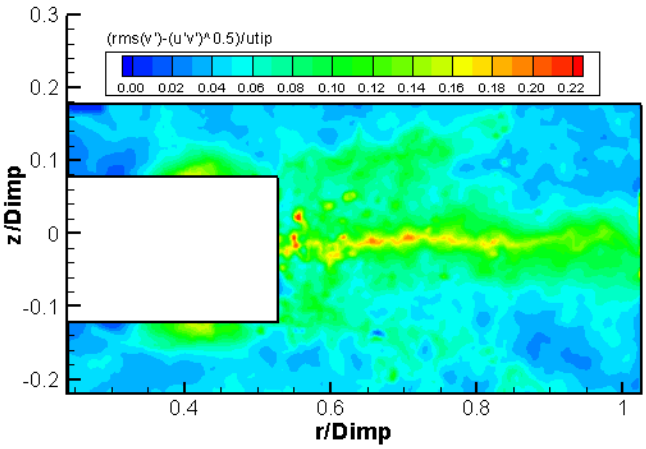


(a)

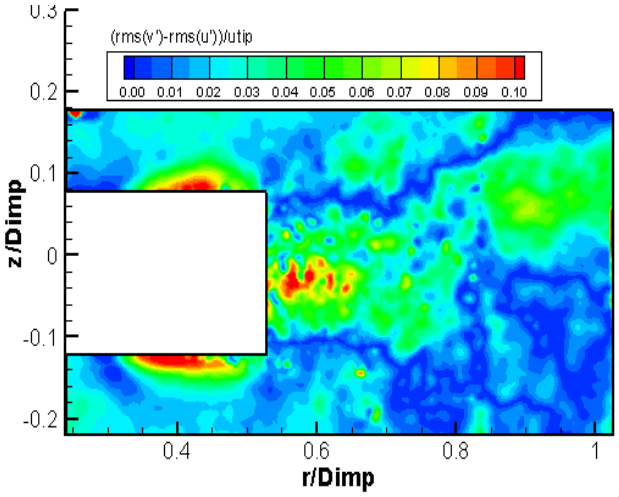


(b)

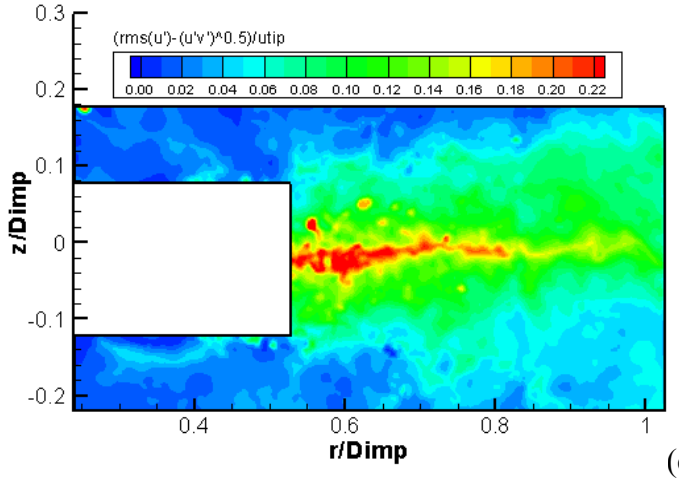


(c)

**Figure 3.14 Difference in Reynolds stresses terms, (a) top, (b) middle, (c) bottom**

A variety of methods are available for the calculation of turbulent dissipation rate. We chose a direct method from the strain rate tensor,

$$\varepsilon = 2\nu\left\langle s_{ij}s_{ij}\right\rangle = \frac{\upsilon}{2}\left\langle\left(\frac{\partial u_i}{\partial x_j}+\frac{\partial u_j}{\partial x_i}\right)^2\right\rangle. \qquad \textbf{3.4}$$

$S_{ij}$ is the strain rate tensor. This tensor contains twelve terms [22]. Two dimentional PIV, providing sufficient spatial resolution, allows for the measurement of five of these quantities. Assuming isotropy for the remaining seven terms, the dissipation can be reduced to the form,

$$\varepsilon = \nu\left[2\overline{\left(\frac{\partial u_r}{\partial r}\right)^2}+2\overline{\left(\frac{\partial u_z}{\partial z}\right)^2}+3\overline{\left(\frac{\partial u_r}{\partial z}\right)^2}+3\overline{\left(\frac{\partial u_z}{\partial r}\right)^2}+2\left(\overline{\frac{\partial u_r}{\partial z}\frac{\partial u_z}{\partial r}}\right)\right] \qquad \textbf{3.5}$$

The propagation of error through the dissipation calculation is of concern. The square of a spatial derivative contains a large degree of error amplification. Therefore to minimize the propagation of error, a fourth order finite difference approximation was used to calculate the velocity gradients. According to this method the velocity gradient of a velocity component u at point i is,

$$\left(\frac{\partial u}{\partial x}\right)_i = \frac{1}{12\Delta}\left[8u_{i+1}-8u_{i-1}+u_{i-2}-u_{i+2}\right] \qquad \textbf{3.6}$$

The method shown in Equation 3.6 was originally developed by Chapra [23]. The direct measurement via Equation 3.5 does not invoke many of the assumptions needed in other methods such as dissipation measurement based on the turbulent kinetic energy. However, the use of this method is not without fault due to the assumption of isotropic turbulence, which was shown not to hold close to the impeller as stated earlier. Figure 3.15 shows dissipation contours for the case of Re=20K. The maximum dissipation is along the centerline of the blade. However

it is not immediately adjacent to the blade. The relative maximum appears around $r/D_{imp}$=0.54. This trend is consistent with numerous previous experiments. The dissipation values are in the range of values presented in other works, however noticeable on the low side. A comparison with other works will be presented in the following section.

The Kolmogorov length scale, representing the spatial scale where the turbulent kinetic energy dissipates into the internal energy of the fluid, can be estimated using ε (defined earlier). The minimum Kolmogorov scale, shown in Figure 3.16, was found to be 19 microns for the case of Re=20K. This prediction has about a 50% difference from the method based on the Reynolds number defined earlier.

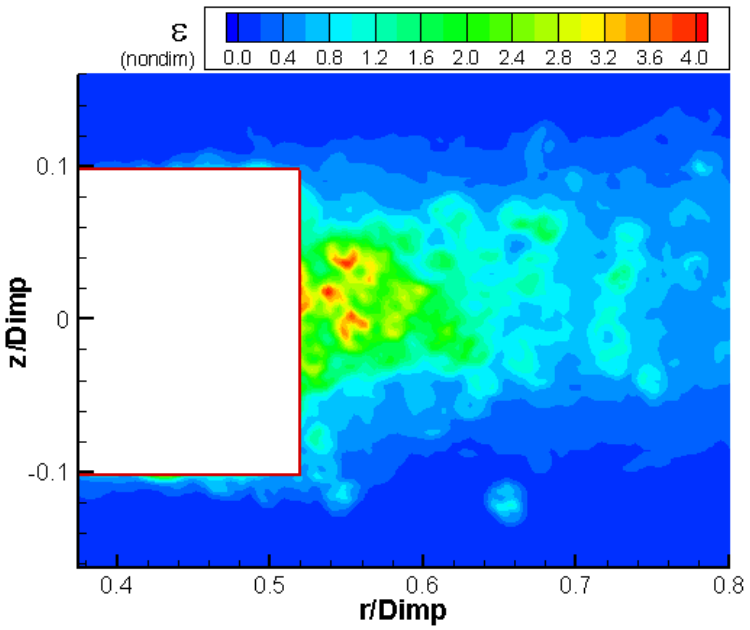


**Figure 3.15 Non-dimentionalized dissipation rate contours for Re=20K**

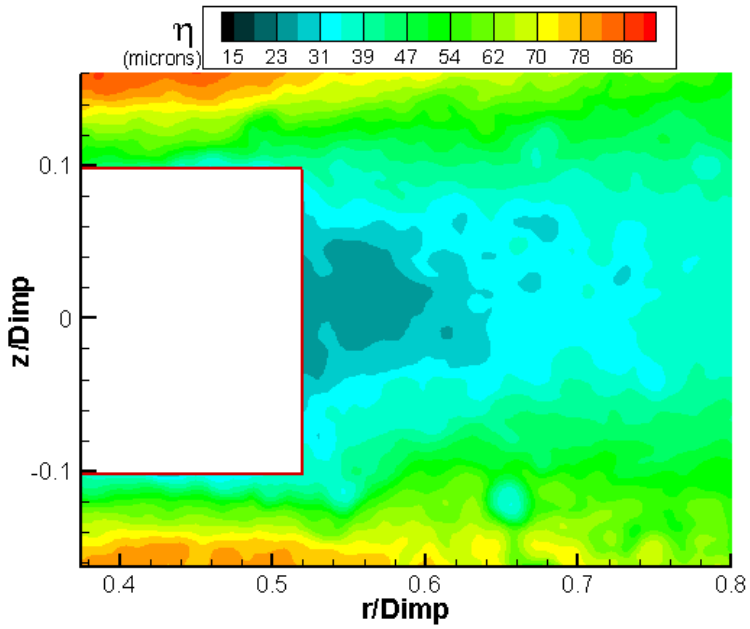


**Figure 3.16 Kolmogorov length scale contours**

## Scaling turbulent quantities with Re

The scaling of the turbulence with Reynolds number will now be investigated. Figure 3.17 and Figure 3.18 show how maximum and mean dissipation in the impeller stream scale with Reynolds number. The impeller stream is defined here as the rectangular region defined by $z/D_{imp}$:-0.1 to 0.1, and $r/D_{imp}$:0.55 to 0.8. A general decreasing trend is observed for the normalized dissipation with increasing Reynolds number. The dissipation measurement is strongly dependant on the spatial resolution of the data. Previous works ([6] and [24]) have discussed the underprediction of the turbulent kinetic energy dissipation versus the ratio of spatial resolution to the Kolmogorov length scale. The maximum dissipation in this study is about half of that reported by Baldi and Yianneskis (2004), although their study had a slightly different geometry as described earlier. As the Reynolds number increases, the ratio of the spatial

resolution to the Kolmogorov scale increases, accounting for the decreasing trend of dissipation with Reynolds number. Other quantities, namely vorticity magnitude, Urms and Vrms appear to follow nearly constant trends in the range of Reynolds numbers investigated here as shown in Figure 3.19 thru-Figure 3.22.

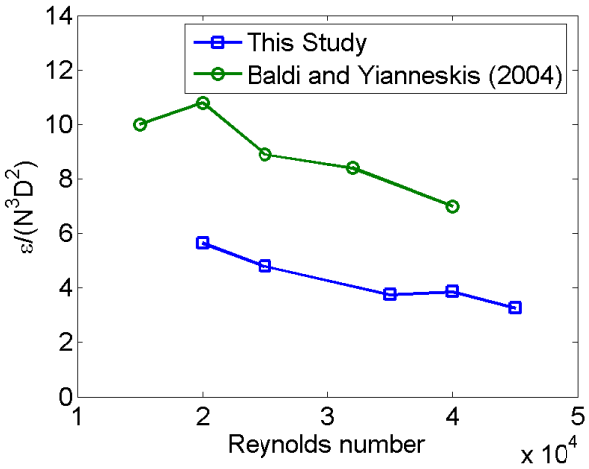


**Figure 3.17 Normalized max dissipation vs. Re**

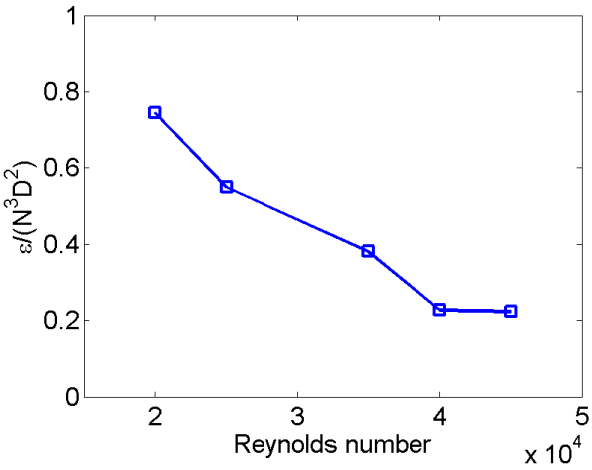


**Figure 3.18 Normalized mean dissipation vs. Re**

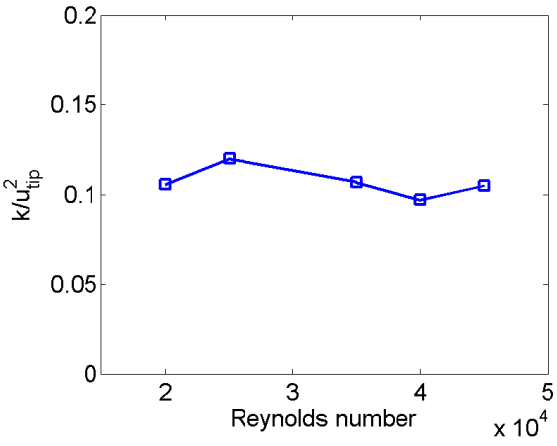


**Figure 3.19 mean k vs. Re**

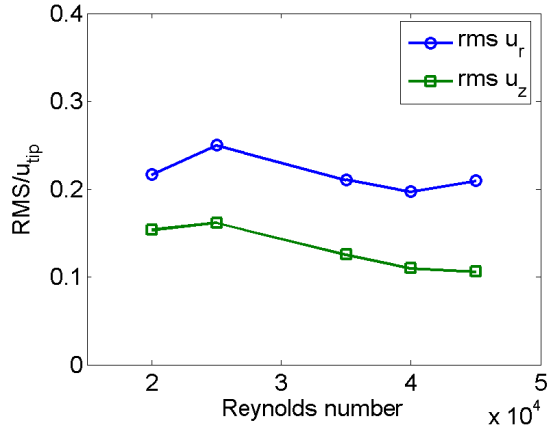


**Figure 3.20 Normalized mean Urms and Vrms vs. Re**

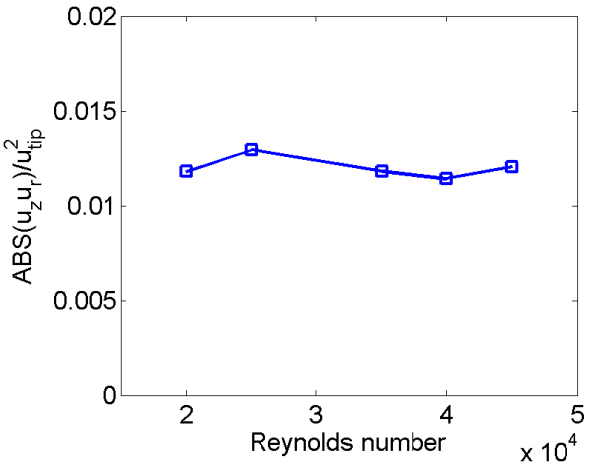


**Figure 3.21 Mean Reynolds stress vs. Re**

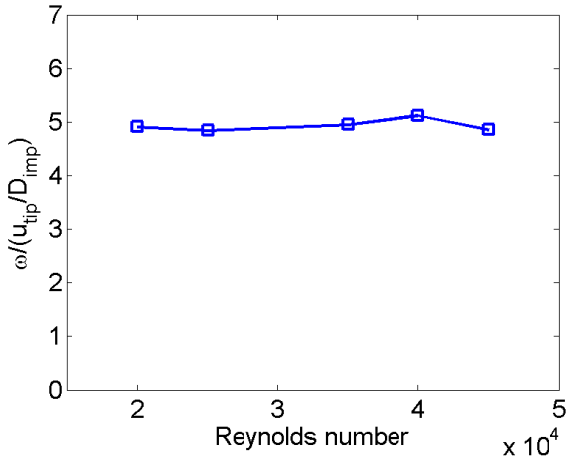


**Figure 3.22 Vorticity magnitude vs. Re**

## Coherent Structures Detection

The trailing vortices from the blade tips have been shown to contain the majority of the Kinetic Energy of the impeller stream. During the experiment, it was observed that the tip vortices exhibited a more erratic behavior with increasing Reynolds number. For example, in the smallest Reynolds number of 20,000, the tip vortices in general seemed to follow a path more aligned with the radial axis than the tip vortices at higher Re. Vortex and coherent structures detection is a useful tool to observe the motion of these vortices and quantify their motion. A number of methods are available to detect vortices. Haller, [25] gives a comprehensive analysis of the various methods.

The Vortex identification method used here was proposed by [26]. The imaginary part of the complex eigenvalue of the velocity gradient tensor is used to detect vortices. The eigenvalues of the velocity gradient tensor, $\mathbf{D}= \nabla\mathbf{u}$, are defined by the characteristics equation,

$$\lambda^3 + P\lambda^2 + Q\lambda + R = 0, \qquad 3.7$$

where $\mathbf{P} = \nabla . \mathbf{u}$, is an invariant and identically zero for incompressible flow. The other invariants are, $\mathbf{Q}=\frac{1}{2}\left[\mathbf{P}^2\text{-tr}(\mathbf{DD})\right]$, and $\mathbf{R}=\frac{1}{3}\left[\text{-}\mathbf{P}^3+3\mathbf{PQ}\text{-tr}(\mathbf{DDD})\right]$. The complex nature of the eigenvalues is determined by the value of the discriminant. The discriminant is defined as,

$$\Delta_d \equiv \left(\frac{1}{2}\mathbf{R}+\frac{1}{27}\mathbf{P}^3-\frac{1}{6}\mathbf{PQ}\right)^2+\left(\frac{1}{3}\mathbf{Q}-\frac{1}{9}\mathbf{P}^2\right) \quad \textbf{3.8}$$

Under the condition that the discriminant, $\Delta_d$, is positive, there will be one real eigenvalue, $\lambda_r$ and a pair of complex conjugated eigenvalues, $\lambda_{cr} \pm \lambda_{ci}$. The advantages in Zhou's method are that it is based on invariants, and therefore frame independent. Also, complex eigenvalues are only produced by regions of circular or spiraling streamlines, meaning shear layers are eliminated from the detection algorithm even though they may have high vorticity. This technique was compared with other methods and determined to be the most consistent and reliable in detecting the tip vortices from the Rushton impeller.

Normally the vortices are visualized by plotting isosurfaces of the magnitude of the complex part of the eigenvalue, $\lambda_{ci}$. The detection of the vortices was carried out here by first binarizing the $\lambda_{ci}$ values. Any $\lambda_{ci}$ value greater than zero, it is assumed, represents a vortex. The binarized scalar field was then put through a nearest neighbor search to determine the nonzero values that were connected to each other, separating the individual vortices from each other. Once the Vortices are separated, their sizes and positions can be determined. Since only the relatively large tip vortices were desired to be detected, all vortices whose size was less than one third the blade height were discarded. This number was determined manually to represent the approximate size of one of the tip vortices.

The detection results are displayed in Figure 3.23 and Figure 3.24. Figure 3.23 shows the distribution of vortex centers for a Reynolds number of 25,000 over 200 frames. There are clear, narrow regions near the impeller blade where the tip vortices stay relatively straight. The vortex paths cease to track radially around r/Dimp=0.7, where they appear more uniformly distributed in the z-direction. Figure 3.24 shows the normalized distribution along the z-coordinate for all Reynolds numbers computed over 1000 frames. The figure is normalized so that the integral of the curve with respect to z is equal to 1. The observation stated earlier, that the tip vortices seem to track radially for low Re, and more erratically for higher Re is quantified in this plot. For the low Re of 20K and 25K, there is a region of low concentration of vortices on the center of the impeller. Towards the tips of the impeller, the distributions are at a maximum, showing that the tip vortices stay in a relatively straight line in the r-direction, especially for the low Reynolds number of 20K and 25K. For higher Reynolds numbers, the distribution flattens out and is a more uniform shape. This indicates that once the tip vortices are shed at a Reynolds number above 35,000, they don't in general travel in a straight radial path as for the low Reynolds number case. It has been reported that the tip vortices carry the majority of the momentum from the impeller stream to the other regions of the Rushton tank. This finding shows that even over a small range of Reynolds numbers between 20,000 and 40,000, the fluid mechanics is vastly different within the Rushton tank.

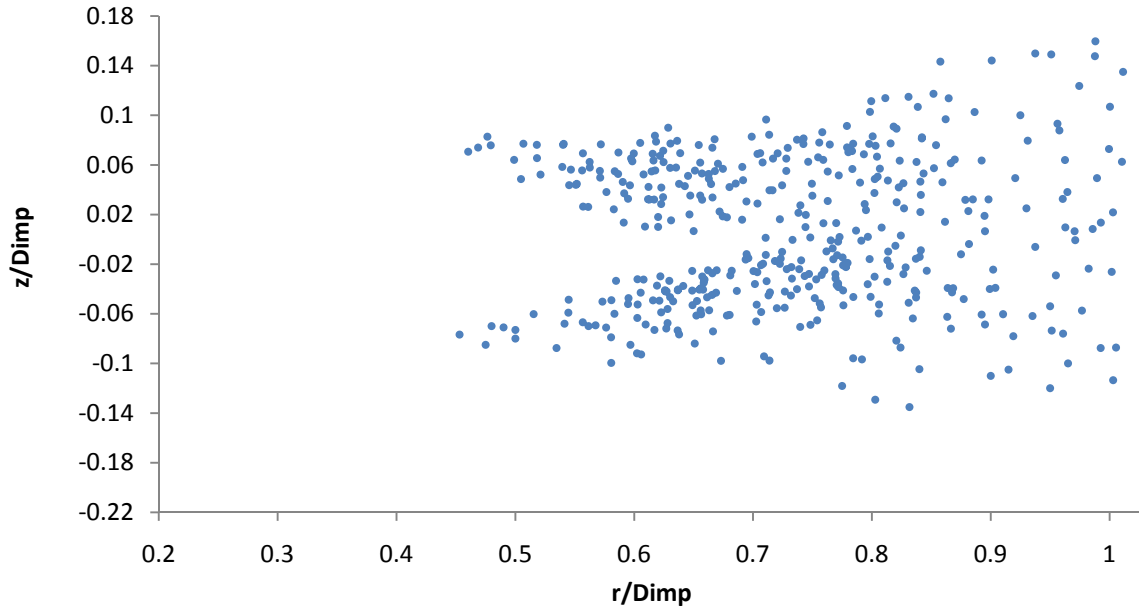


**Figure 3.23 Distribution of vortex detection along the z-direction for Re=25K**

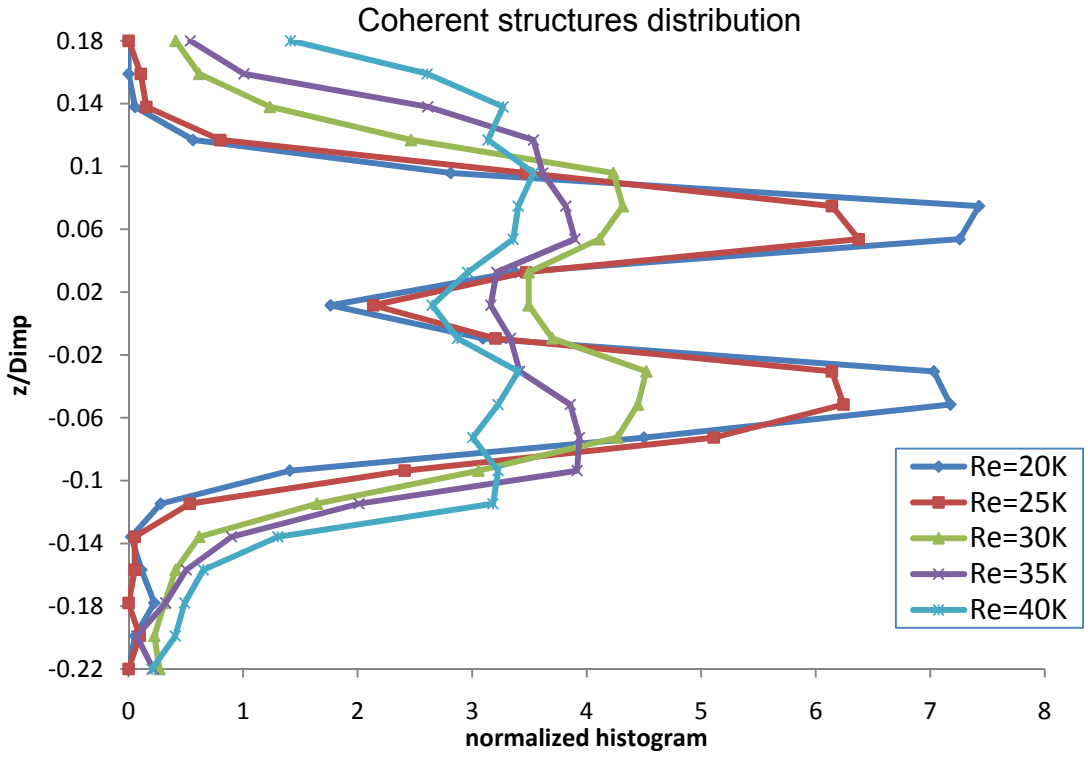


**Figure 3.24 normalized histogram of vortex detection along the z-direction**

## CONCLUSIONS

The mean flow, as well as turbulent quantities were determined in a Rushton turbine using time resolved DPIV. The objective was to provide accurate turbulence measurements in the impeller stream. The periodic component of the flow was found to contribute significantly to the fluctuating velocities. In addition the turbulent kinetic energy was reduced by 65% by removing the blade frequency. The turbulent kinetic energy dissipation rate was found to be less affected by the periodicity of the flow, however did vary by as much as 25%. The flow was shown to be anisotropic close to the impeller. Vortex detection revealed that the tip vortices travel in a nearly radial direction from the impeller for small Reynolds numbers and in more erratic directions for higher Reynolds numbers. The maximum and mean normalized dissipation in the impeller stream showed decreasing trends with the Reynolds number. Other normalized turbulence quantities, namely $U_{rms}$, $V_{rms}$, Reynolds stresses and vorticity magnitude scaled as nearly constant values with the Reynolds number. Good agreement was found for time averaged Reynolds stresses and turbulent energy dissipation.

## REFERENCES


1. Lamberto, D.J., et al., Using time-dependent RPM to enhance mixing in stirred vessels. Chemical Engineering Science, 1996. 51(5): p. 733-+.
2. Rao, M.A. and R.S. Brodkey, Continuous flow stirred tank turbulence parameters in the impeller stream. Chemical Engineering Science, 1972. 27: p. 137-156.
3. Baldi, S. and M. Yianneskis, On the quantification of energy dissipation in the impeller stream of a stirred vessel from fluctuating velocity gradient measurements. Chemical Engineering Science, 2004. 59(13): p. 2659-2671.
4. Piirto, M., et al., Measuring turbulence energy with PIV in a backward-facing step flow. Experiments in Fluids, 2003. 35(3): p. 219-236.
5. Wu, H. and G.K. Patterson, Laser-Doppler Measurements of Turbulent-Flow Parameters in a Stirred Mixer. Chemical Engineering Science, 1989. 44(10): p. 2207-2221.
6. Saarenrinne, P., M. Piirto, and H. Eloranta, Experiences of turbulence measurement with PIV. Measurement Science & Technology, 2001. 12(11): p. 1904-1910.
7. Sharp, K.V. and R.J. Adrian, PIV study of small-scale flow structure around a Rushton turbine. Aiche Journal, 2001. 47(4): p. 766-778.
8. Sheng, J., H. Meng, and R.O. Fox, A large eddy PIV method for turbulence dissipation rate estimation. Chemical Engineering Science, 2000. 55(20): p. 4423-4434.
9. Okamoto, Y., N. Nishikawa, and K. Hashimoto, Energy dissipation rate distribution in miixing vessels and its effects on liquid-liquid dispersion and solid-liquid mass transfer. International Chamical Engineering, 1981. 21: p. 88-94.
10. Kresta, S.M. and P.E. Wood, The Flow Field Produced by a Pitched Blade Turbine - Characterization of the Turbulence and Estimation of the Dissipation Rate. Chemical Engineering Science, 1993. 48(10): p. 1761-1774.
11. Mununga, L., K. Hourigan, and M. Thompson, Comparative study of flow in a mixing vessel stirred by a solid disk and a four bladed impeller. 14th Australasian Fluid Mechanics conference Adelaide University, Adelaide, Australia 10-14, 2001.
12. Lee, K.C. and M. Yianneskis, Turbulence properties of the impeller stream of a Rushton turbine. Aiche Journal, 1998. 44(1): p. 13-24.

13. Nouri, J.M. and J.H. Whitelaw, Effect of size and confinement of the flow characteristics in stirred reactors. Proceedings of the International Symposium on Applications of Laser Techniques to Fluid Mechanics, Lisbon, 1990. 23.2.
14. Adrian, R.J., Twenty years of particle image velocimetry. Experiments in Fluids, 2005. 39(2): p. 159-169.
15. Westerweel, J., Fundamentals of digital particle image velocimetry. Measurement Science & Technology, 1997. 8(12): p. 1379-1392.
16. Abiven, P.P.V., SUPER SPATIO-TEMPORAL RESOLUTION, DIGITAL PIV SYSTEM FOR MULTIPHASE FLOWS WITH PHASE DIFFERENTIATION AND SIMULTANEOUS SHAPE AND SIZE QUANTIFICATION. ASME International Mechanical Engineering Congress & Exposition, 2002. IMECE2002(33115): p. 10.
17. Abiven, P.P.V., COMPARATIVE STUDY OF ESTABLISHED DPIV ALGORITHMS FOR PLANARVELOCITY MEASUREMENTS. ASME International Mechanical Engineering Congress & Exposition, 2002. IMECE2002(33170): p. 10.
18. Scarano, F. and M.L. Riethmuller, Iterative multigrid approach in PIV image processing with discrete window offset. Experiments in Fluids, 1999. 26(6): p. 513-523.
19. Scarano, F. and M.L. Riethmuller, Advances in iterative multigrid PIV image processing. Experiments in Fluids, 2000. 29: p. S51-S60.
20. Wereley, S.T. and C.D. Meinhart, Second-order accurate particle image velocimetry. Experiments in Fluids, 2001. 31(3): p. 258-268.
21. Westerweel, J., D. Dabiri, and M. Gharib, The effect of a discrete window offset on the accuracy of cross-correlation analysis of digital PIV recordings. Experiments in Fluids, 1997. 23(1): p. 20-28.
22. Hinze, J.O., Turbulence. 2d ed. McGraw-Hill series in mechanical engineering. 1975, New York: McGraw-Hill. x, 790 p.
23. Etebari, A. and P.P. Vlachos, Improvements on the accuracy of derivative estimation from DPIV velocity measurements. Experiments in Fluids, 2005. 39(6): p. 1040-1050.
24. Baldi, S., D. Hann, and M. Yianneskis, On the measurement of turbulence energy dissipation in stirred vessels with PIV techniques. Proceedings of the 11th International Symposium on Applied Laser Techniques in Fluid Mechanics, Lisbon, 2002.

25. Haller, G., An objective definition of a vortex. Journal of Fluid Mechanics, 2005. 525: p. 1-26.
26. Zhou, J., et al., Mechanisms for generating coherent packets of hairpin vortices in channel flow. Journal of Fluid Mechanics, 1999. 387: p. 353-396.

# Chapter 4: Bubble interactions with free interfaces

This manuscript has not yet been submitted for publication

Michael Brady[1] and Pavlos P. Vlachos[2]
[1]Department of Engineering Science and Mechanics
[2]Department of Mechanical Engineering
Virginia Polytechnic Institute & State University
Blacksburg, VA 24060 USA

## ABSTRACT

Bubble collisions with other bubbles, particles or interfaces are very important in a variety of mass transfer applications. Here, the rise of a buoyant bubble and its interaction with a free liquid surface was experimentally investigated using a Time-Resolved Digital Particle Image Velocimetry (TRDPIV as a function of bubble size, and surfactant concentration of the fluid medium. It is shown that the presence of a surfactant significantly affected the rising approach and the characteristics of the bubble interaction and collision with the free surface. The addition of a surfactant changes the viscous forces around the bubble due to the adsorption coverage of the surfactant at the bubble-fluid interface. A bubble traveling through a surfactant solution (1e-3 M Sodium Dodecyl Sulfate) did not exhibit rebounding behavior regardless of its size. The flow filed was characterized by a vortex-ring wake, which was trailing the bubble during the approach stage. After impact, the vortex ring slowly migrated away, parallel to the wall and dissipated. In contrast a smaller (1.1 mm) bubble in pure water exhibited a rebounding behavior associated with more complex flow field and vortex interactions, and the vortices dissipated more quickly than in the no-rebound case.

## INTRODUCTION

The aim of this work is to study the dynamics of a bubble rising and bouncing on a free surface and the effect of presence of surfactants on this process. A great deal of work has been carried out concerning the dynamics of a solid sphere bouncing on a wall immersed in a fluid. [1] and [2] provide detailed reviews of this topic. Much of the work involves optically tracking the motion of the sphere and measuring the coefficient of restitution ε (velocity after impact divided by the velocity before impact). The Stokes number has been shown to be a good indicator of the coefficient of restitution. An explanation of the dependence on the Stokes number was given by [1] by relating it to the lubrication force.

Work involving bubbles or buoyant droplets has been investigated by a number of authors. [3] performed shadowgraph experiments to track a rising drop as it struck a solid wall. It was determined that 80% of the initial kinetic energy was dissipated with a single collision with the solid wall. [4] numerically modeled a bubble bouncing on a solid surface using the Boundary Element Method. However this was done using a potential flow model and solving the Laplace equation.

Bubble motion is significantly affected by the properties of the gas-liquid interface. The effect of surfactants on bubble motion in various liquids has been investigated by various authors. Malysa [5] classified the velocity of a rising bubble as a function of the concentrations of various solutions and the adsorption coverage of the surfactants. The bubble velocity was significantly influenced by the extent of the adsorption coverage of the surfactant to the bubble. A variety of theoretical works ([6] and [7]) explaining the underlying mechanisms of surfactant adsorption and its effect on the bubble velocity has also been carried out.

To date, a time-resolved analysis of the flow around a bubble impacting a free surface has not been presented. In this study, the flow around an impacting bubble as well as the bubble shape and trajectory are measured using Time Resolved Digital Particle Image Velocimetry (TRDPIV) and advanced image processing techniques.

## NOMENCLATURE

| | |
|---|---|
| $U_o$ | terminal velocity (m/s) |
| We | Weber number |
| Re | bubble Reynolds number |
| $\rho$ | liquid density ($kg/m^3$) |
| D | bubble diameter (m) |
| $\sigma$ | surface tension (N/m) |
| $\nu$ | kinematic viscosity ($m^2/s$) |
| $\lvert\lambda_{ci}\rvert$ | Normalized eigenvalue |
| $\lambda_{ci}$, $\lambda_{cr}$ | Parts of eigenvalue |
| $\lambda$ | Eigenvalue |
| S | Rate of strain tensor (1/s) |
| $\Omega$ | Vorticity tensor (1/s) |
| P,Q,R | Invariants in eigenvalue equation |
| $\chi$ | Shape factor |
| $\varepsilon$ | coefficient of restitution |
| $\Delta T$ | inverse of pulse pair frequency (s) |
| $\Delta t$ | laser pulse separation (s) |
| $V_{mag}$ | Velocity magnitude w.r.t. $U_o$ |
| **D** | Velocity gradient tensor (1/s) |
| $\Delta_d$ | discriminant |

### Experimental Setup

The objective is to study the dynamics of a rising bubble, and its interaction with the liquid and the free interface. Therefore it is necessary to track the shape and position of the bubble, and obtain a space and time-resolved flow field in the vicinity of the bubble and the free surface. The experimental setup, shown in Figure 4.1, utilizes a TRDPIV system to measure these quantities.

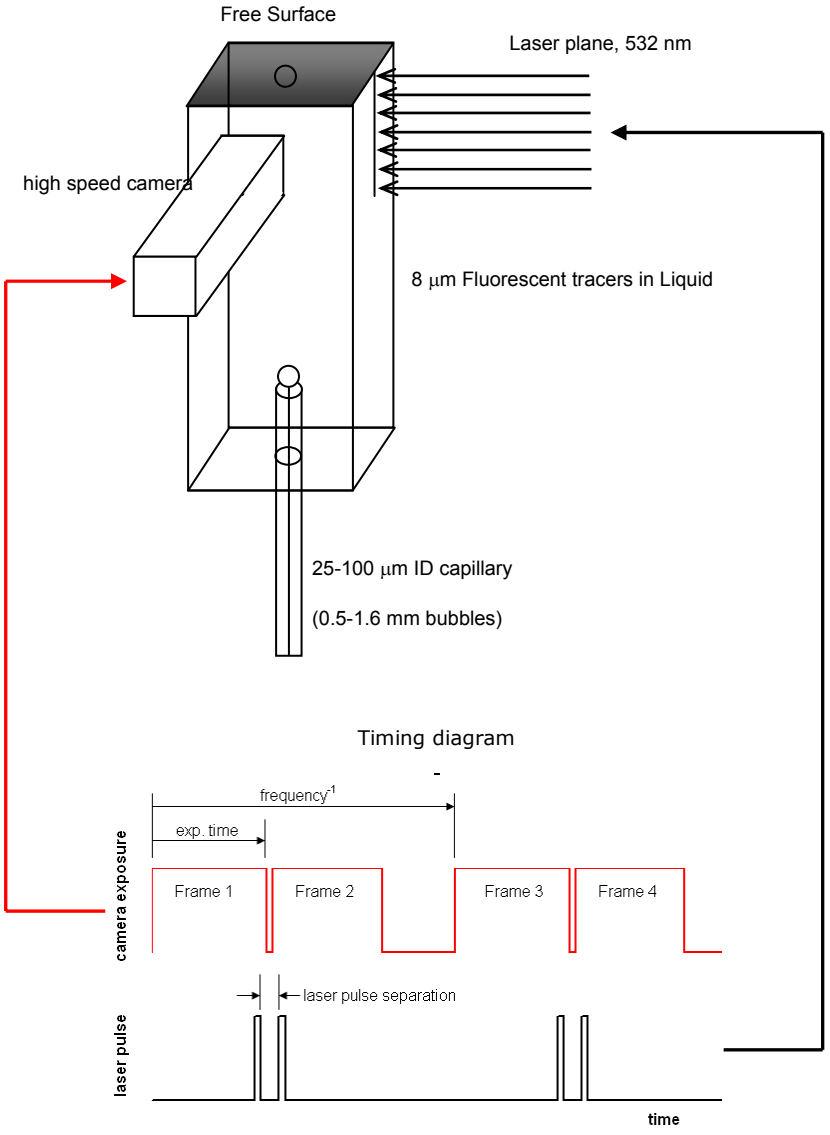


**Figure 4.1 - Schematic of experimental setup and the DPIV timing sequence.**

The experimental setup consisted of a 1"x1"x4" glass cell, equipped with varying-diameter glass capillaries inserted from the bottom. The size of a bubble released from a capillary depends on the inner diameter of the capillary, the surface tension of the liquid, and the mass flow rate. Providing the mass flow rate through the capillary is sufficiently small, the capillary produces uniform bubble diameters (regardless of the gas flow rate). The capillary inner diameters ranged

from 25 to 100μm. The corresponding bubble sizes in the liquid solutions produce by the capillaries ranged from 500 to 1600 μm.

The kinematics of a bubble moving through a liquid has been shown to be extremely sensitive to even small quantities of surfactants in the liquid. For example, [5] have shown that the purity of water (tap versus distilled, deionized, or nanopure water) can significantly affect the terminal velocity of a bubble. It is therefore important to closely control the contents of the solutions. The solutions studied in the present work were nanopure water and a 1E-3 M Sodium Dodecyl Sulfate solution (SDS). It is also necessary to seed the solutions with flow tracers, to photographically measure the flow velocities around the bubble. The particles used in this process must be a dry powder form to avoid surfactant contamination from the anti-coagulant agent generally sold in flow tracer solutions. The flow tracers used were 8 μm fluorescent polystyrene particles with a specific gravity of 1. These particles have an absorption maximum at 540nm and an emission maximum at 612 nm. A complete list of experimental conditions is shown in Table 4.1.

The rising bubbles passed through a planar laser sheet with a thickness of about 1mm, shown in Figure 4.1. Care was exercised to insure that the center of the bubble passed as close as possible through the laser sheet. The distance the bubble traveled from the capillary to the free surface was large enough for the bubbles to reach terminal velocity, and small enough to prevent the more energetic bubbles from exhibiting the customary path oscillations that have been well documented [8]. Terminal velocities were determined through image processing of the bubble images.

The high-speed camera used to record the images was an IDT X5 camera with resolution of 1280x1024 pixels. The field was illuminated using a Lee-Lasers Nd-Yag laser (50w at 10kHz). The laser and the camera were time using an external timing hub. As the bubble passes through the laser sheet it scatters the 532nm laser light according to Lorenz-Mie theory. This elastic scattering was filtered out of the image using a high pass filter (cutoff wavelength of 580 nm), leaving only the red band emission of the flow tracers to pass into the CMOS sensor. It is necessary to subtract the bubble from the image using a filter because the bubble would otherwise dominate the light energy sent into the camera, making velocity determination difficult.

The timing diagram of the PIV setup is shown in Figure 4.1. The laser pulse separation, which determines the displacement of the bubble between successive frames, was varied in order to utilize the one quarter rule for PIV processing. That is, the maximum displacement of the flow tracers should be about one quarter the size of the interrogation window. Considering that the highest velocities in the flow are in the vicinity of the bubble interface, the bubble rising terminal velocity was used as the reference value. Subsequently this secures that the bubble displacement meets the same criteria between consecutive frames. The flow sampling frequency (image pair) was set to 750 Hz for all of the cases shown here. This corresponds to a velocity field snapshot every 1.33 ms. The magnification of the lens was varied depending on the bubble size and ranged from 5.5 to 16 μm per pixel. Considering the optical setup and the software algorithm used in processing, the spatial resolution of the experiment (vector spacing) varied from 24μm to 40μm per vector. A sample image is shown in Figure 4.2

**Table 4.1 - Experimental Conditions**

| Test | Capillary ID (μm) | fluid type | surfactant | Surface Tension (N/m) | Laser pulse separation (μs) | Laser Frequency (Hz) | Pixel Size (μm/pix) |
|---|---|---|---|---|---|---|---|
| 1 | 25 | H2O & sufractant | 1e-3 SDS | 0.0443 | 330 | 750 | 5.6 |
| 2 | 51 | H2O & sufractant | 1e-3 SDS | 0.0443 | 285 | 750 | 7.0 |
| 3 | 102 | H2O & sufractant | 1e-3 SDS | 0.0443 | 310 | 750 | 10.2 |
| 4 | 102 | Nanopure H20 | none | 0.0728 | 200 | 750 | 10.2 |
| 5 | 51 | Nanopure H20 | none | 0.0728 | 200 | 750 | 7.0 |
| 6 | 25 | Nanopure H20 | none | 0.0728 | 500 | 750 | 5.6 |

## Image Preprocessing

Once the image pairs were recorded, the bubble perimeter and the center of mass were determined using image dilation and erosion. Because the bubble images were very dark inside the bubble and contained flow tracers outside the bubble, image dilation had the effect of assigning the inside of the bubble a binary value of zero, and the fluid a binary value of one. Image erosion was then performed with the same template so as to preserve the original shape of the bubble. Once the fluid and bubble were separated, the geometric center and the shape of the bubble could be determined. The bubble region was then subtracted from the original images. The static region above the free interface was found and subtracted out of the images as well. These images were then processed using an in house developed DPIV analysis software that is described in the following section.

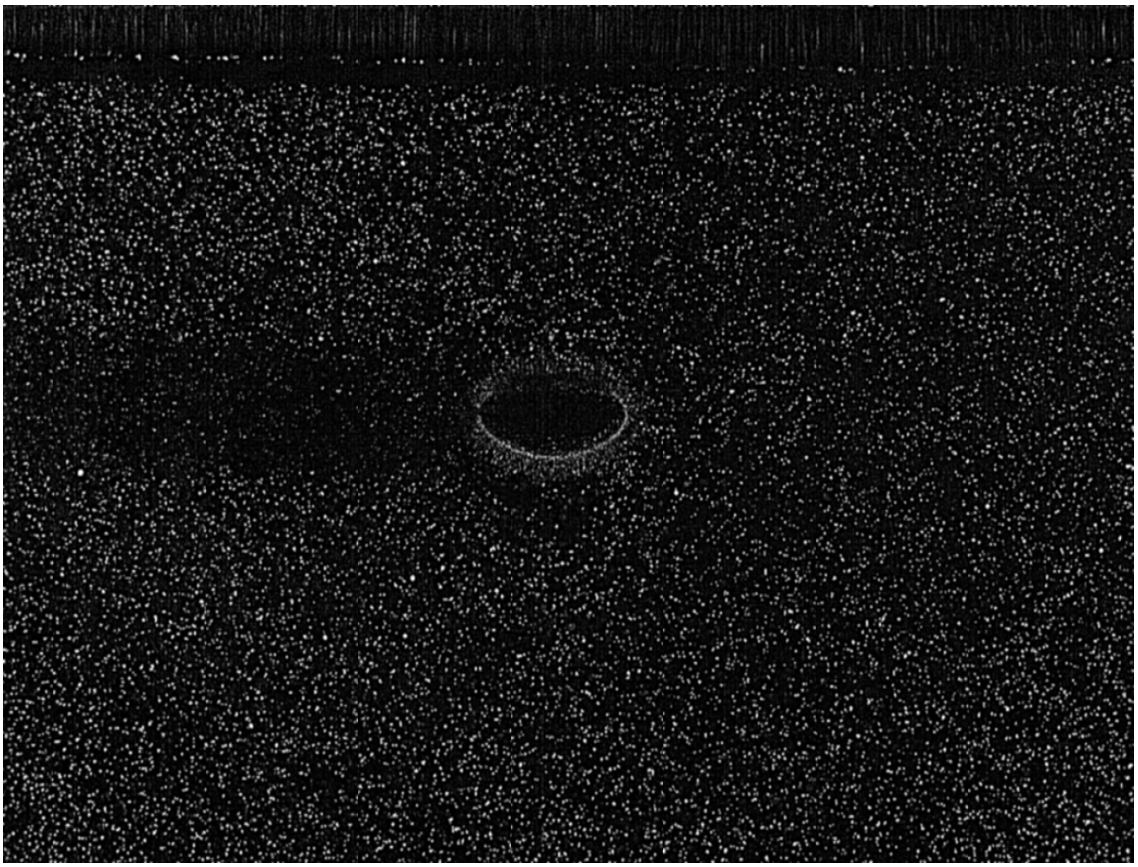

**Figure 4.2 - Raw image of a 1.02 mm bubble rising in pure water surrounded by flow tracers with a free interface.**

## TRDPIV Processing and Multi-frame correlation

The time resolved nature of the data in this study allowed for a new technique to be utilized. It is well known that PIV data suffers from bias errors depending on the displacement between successive frames and the window size [9]. The error increases as the displacement moves from this value in either direction. The percent error is particularly high for very low displacements. To reduce the error, the displacement could be increased by correlating images separated by a longer period of time. Correlating over a chosen time interval, or Multiple Frame Correlation, has been shown to significantly reduce the error for smaller particle displacements [10].

Multiple frame correlation was implemented in the following as shown in Figure 4.3. The raw image pairs were processed by cross correlation for the minimum Δt, the laser pulse separation. The displacement value for each vector was replaced by correlating over a longer time interval if it fell below the threshold of 0.4 pixels. The new time interval, 2ΔT+Δt, where ΔT is the inverse of the pulse pair frequency, spanned five laser pulses. The new displacement value was kept if its value was greater than 0.4 pixels, and another iteration over a longer time interval was performed if not. The third time interval, spanning nine laser pulses was 4ΔT+Δt as shown in Figure 4.3. The velocity was then determined by dividing by the appropriate time interval. The threshold value of 0.4 pixels was determined by considering the displacement of particles for each of the three time intervals. A pixel threshold value too low would allow too much error from the smallest time interval (Δt) in the vector field. Conversely, a pixel threshold value too high would allow very high displacements from the longer time interval. Displacements that are too high introduce other errors from the cross correlation including loss of correlation effects and wraparound aliasing.

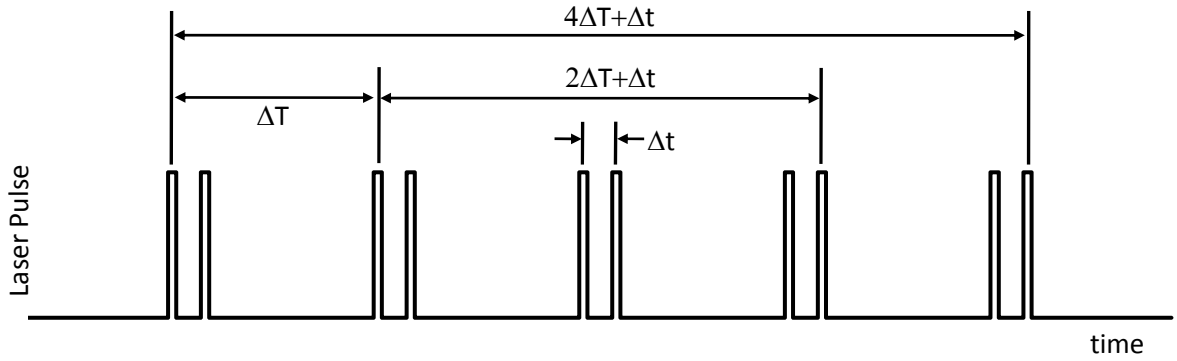


**Figure 4.3 - laser timing diagram for multiple frame correlation**

Multiple frame correlation will now be demonstrated with experimental data. Figure 4.4 shows a 1.06 mm bubble rising in pure water, the velocity field is shown in Figure 4.4 for the case of (a) normal double pulsing with one time interval, $\Delta t$, and (b) multiframe correlation incorporating three possible time intervals. The vector length is kept constant in order to clearly show the flow field topology in the low velocity regions. It is clear from the vector plots (Figure 4.4, a) that the standard correlation contains a significant level of random error and noise while the multiframe correlation (Figure 4.4 b) suppresses most of that error. As expected the normal correlation has a great deal of fluctuation in the velocity field for low velocities (below about 0.4 pixels). Multiframe correlation produces a noticeably smoother vector field. Figure 4.4 does not contain any smoothing or validation operations. A median validation was performed on the multiframe correlation and is shown in Figure 4.5. It should be noted that the vector plots shown thus far are downsampled and only display one quarter of the total vectors calculated in the given region. Figure 4.6 shows the three different correlation regions for a 1.6 mm bubble rising and settling at the free surface in a surfactant solution. The vortex ring shown on either side of the bubble is clearly in a low velocity region due to it using a longer time interval in the correlation. Vortex rings are present in many of the cases and occur in relatively slow regions. In addition, calculating velocity gradients tend to amplify any error in the velocity field. Velocity gradients will be used in the detection of these structures, as will be shown. Multiphase correlation is therefore a very useful tool for this particular experiment.

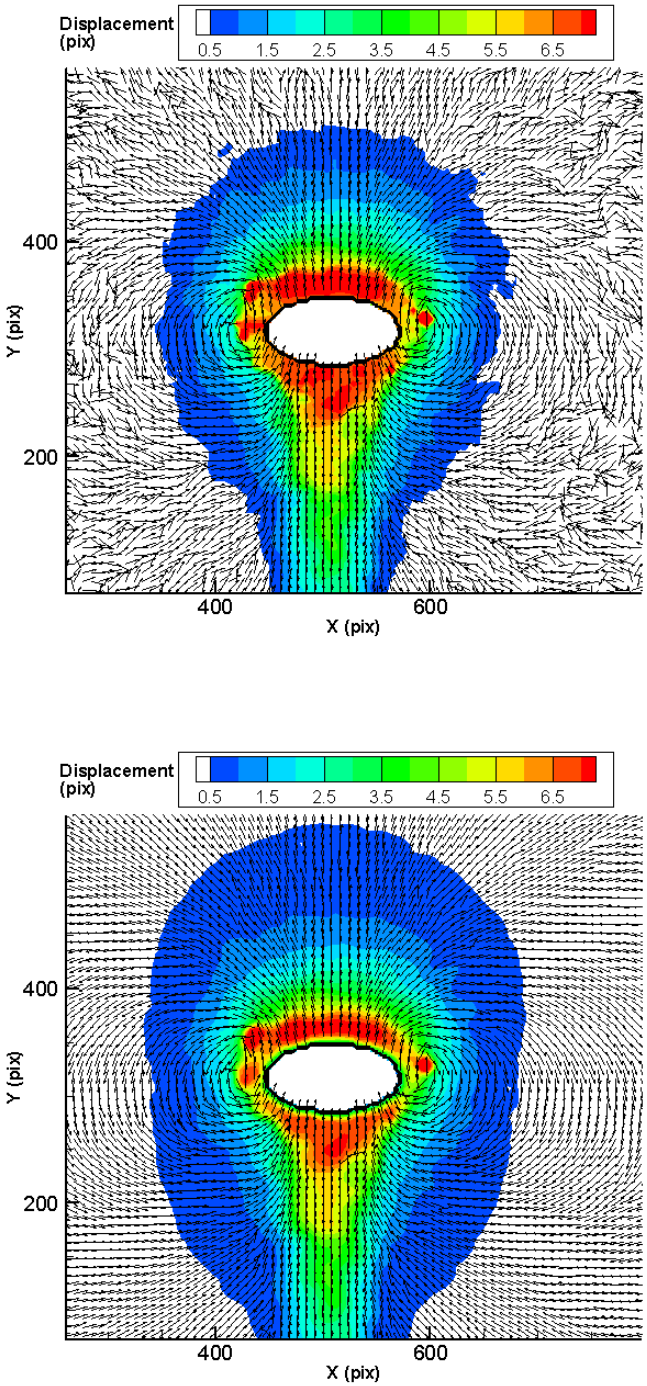


**Figure 4.4 - Vector fields (a) top, normal double pulsing and (b) bottom, using multiframe correlation. No validation is used. Vector length is constant in order to clearly show the field topology which otherwise would not be visible in the low velocity regions.**

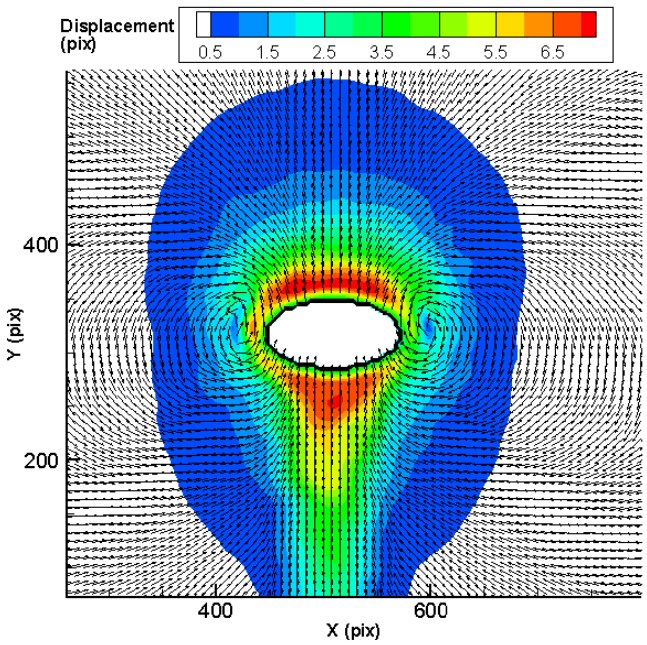


**Figure 4.5 - Final field for multiframe correlation with validation and uniform vector size**

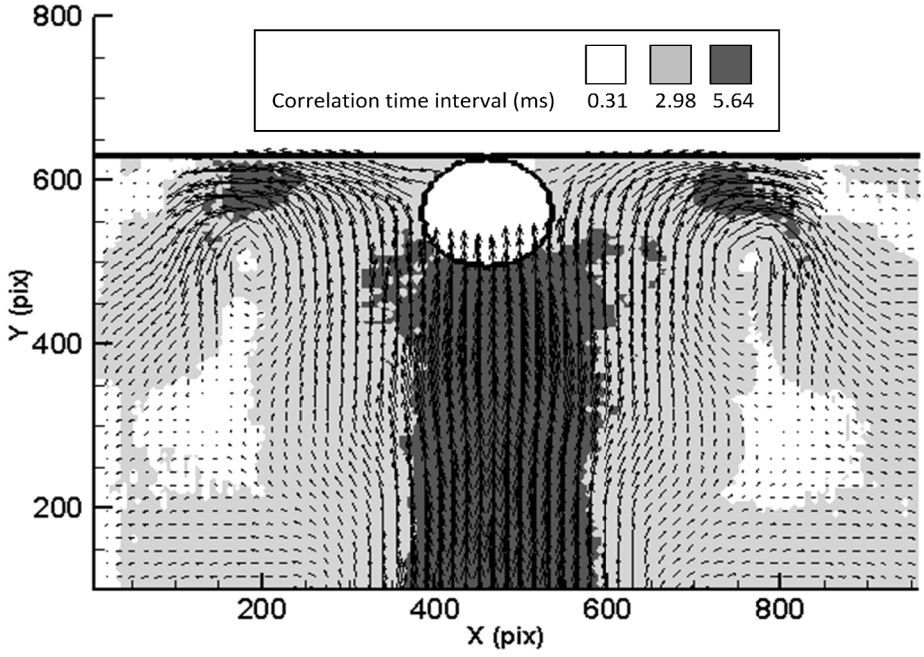


**Figure 4.6 - Velocity field around a bubble after impact with a free surface, contours represent three correlation time intervals**

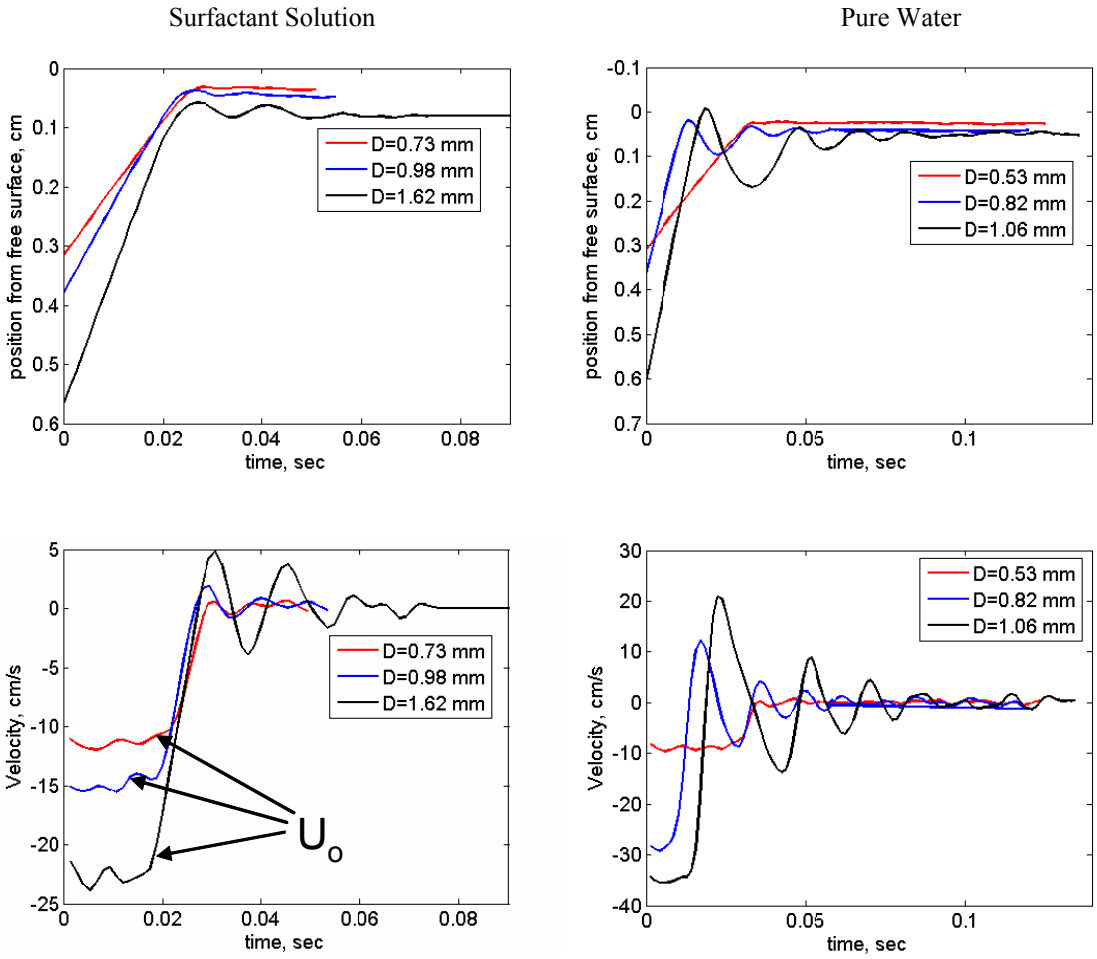


**Figure 4.7: Trajectories and velocities for bubbles moving through a surfactant solution (left) and pure water (right).**

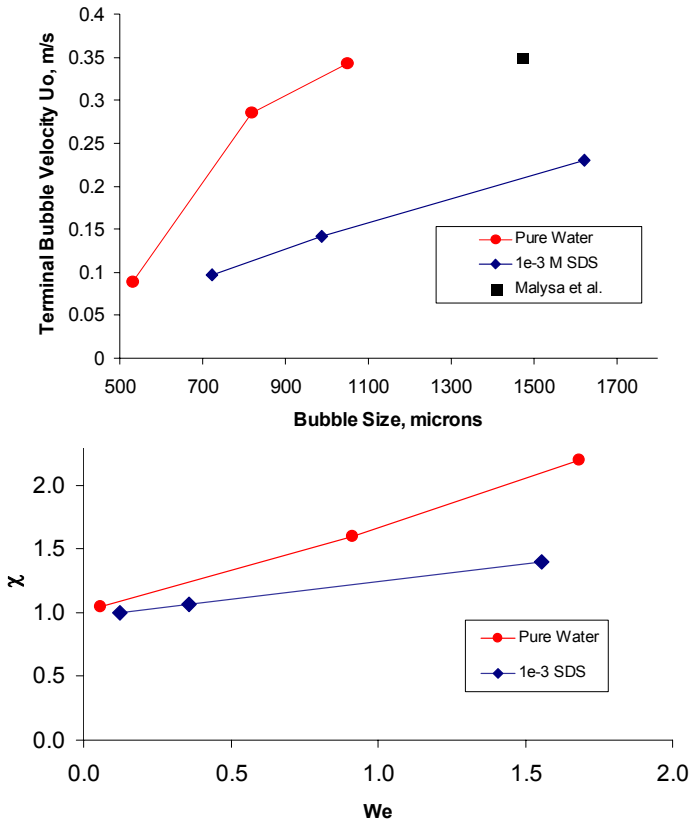


**Figure 4.8: (a-left) Terminal velocity versus bubble size (b-right) Shape factor versus Weber number**

# RESULTS AND DISCUSSION

## Bubble motion

The motion of the bubbles is dependant on the bubble size and the liquid medium. Figure 4.7 shows trajectories and corresponding velocities for varying sized bubbles moving through pure water and a 1E-3 M SDS solution. The velocities were calculated using a second order central difference scheme. In the case of pure water, the larger sized bubbles (D=1.06mm and 0.82mm) exhibited a rebounding behavior and the smaller bubble (D=0.53) did not. The largest bubble rebounded three times, each time dissipating more energy before coming to a rest.

The surfactant solution significantly slowed the approach velocity of the bubbles, and no rebounding; only shape oscillations occurred on impact with the free surface. The velocity calculations in Figure 4.7 show that the bubble velocities remained constant for a period of time before decelerating close to the wall, indicating they reached terminal velocity.

The terminal velocities of the bubbles versus their diameters are shown in Figure 4.8. The addition of a surfactant significantly decreases the terminal bubble velocity. The case of pure water contains a 1.06 mm bubble, and in the surfactant there is a 0.98 mm bubble. The velocity in pure water for these similar bubble sizes is about 260% greater than that of the surfactant solution. An experimental point from the literature in the case of pure water is also included. The terminal velocity of about 35 cm/s in pure water is the maximum velocity observed in this study as well as in the literature for this range of bubble diameters.

The reduced bubble velocity in the surfactant solution can be explained by considering the surface adsorption of the surfactant. Surfactant molecules are transported to the bubble surface as it travels through the liquid. The rising bubble will decelerate until the bubble-liquid interface has accumulated surfactants over the entire interface. The boundary condition at the interface has essentially changed from a free slip condition where there is no surfactant to nearly a no slip condition where surfactants are present. It is assumed that in this study that the bubble has accumulated surfactants over its entire surface by the time it reaches the measurement area since it has attained a constant velocity (terminal velocity).

The shape factor, $\chi$, is a measure of the deformation of the bubble. It is defined here as the ratio of the length of the major axis to the length of the minor axis of the bubble. The shape factor when the bubble has reached its terminal velocity .is shown in Figure 4.8 plotted versus the

Weber number. The Weber number, $We=\rho d U_o^2/\sigma$, is the ratio of inertia to the cohesion due to surface tension. The behavior of these functions appear to be very nearly linear. However, they do not follow the same trend. It is not clear why this discrepancy is in the trends since the Weber number includes the diameter, terminal velocity and the surface tension in the formulation.

### Fluid Motion

The dynamics of a bubble rebounding on a free surface can only be fully described by considering the fluid flow. Figure 4.9 shows the measured flow field around a 1.1 mm bubble in pure water. The Reynolds number, $Re=U_oD/\nu$, for this case is 360. The trajectory, along with the corresponding instantaneous velocity fields at selected time instants are shown. In the approach stage, $t_1$, the bubble is elliptical. The streamtraces indicate that the flow is attached around the entire surface of the bubble. The flow field resembles a doublet, however the Reynolds number is quite high at 360. At just prior to striking the free interface, $t_2$, the bubble has a trailing vortex ring. The vortex ring then moves near the free surface as the bubble rebounds, and stays there. The bubble rebounds two more times and finally comes to rest. The role of vortex dynamics in the motion of the bubble is evident.

The rise of a 1.6mm bubble in a 1E-3 M SDS solution is shown in Figure 4.11. The Reynolds number is Re=370, very close to the previous case described above. The flow field in the approach stage, $t_1$, indicates the presence of a trailing steady vortex ring behind the bubble. As the bubble impacts the free surface, the vortex ring convects around the bubble and slowly expands out along the free surface as shown in the time sequence. The significantly different behavior of two bubbles of similar Reynolds number illustrates the significant effect of the

surfactant on the flow field and the bubble motion. It is also evident that vortex dynamics plays an important role in classifying the system.

### Vortex Identification

Characterizing the vortical structures in each of the cases shown here can show insight into the underlyding dynamics of the system. Identifying the motion and strength of the vortices generated during the bubble approach and impact with the free surface. There exist a variety of methods to identify and track the motion of a vortex. [11] gives a comprehensive analysis of the various methods.

The Vortex identification scheme used here is based on a method proposed by [12]. The imaginary part of the complex eigenvalue of the velocity gradient tensor is used to detect vortices. The eigenvalues of the velocity gradient tensor, $\mathbf{D}= \nabla\mathbf{u}$, are defined by the characteristics equation,

$$\lambda^3 + \mathbf{P}\,\lambda^2 + \mathbf{Q}\,\lambda + \mathbf{R} = 0, \qquad \textbf{4.1}$$

where $\mathbf{P} = -\nabla.\mathbf{u}$, is an invariant and identically zero for incompressible flow. The other invariants are, $\mathbf{Q}=\frac{1}{2}\left[\mathbf{P}^2\text{-tr}(\mathbf{DD})\right]$, and $\mathbf{R}=\frac{1}{3}\left[-\mathbf{P}^3+3\mathbf{PQ}\text{-tr}(\mathbf{DDD})\right]$. The complex nature of the eigenvalues is determined by the value of the discriminant. The discriminant is defined as,

$$\Delta_d \equiv \left(\frac{1}{2}\mathbf{R}+\frac{1}{27}\mathbf{P}^3-\frac{1}{6}\mathbf{PQ}\right)^2+\left(\frac{1}{3}\mathbf{Q}-\frac{1}{9}\mathbf{P}^2\right) \qquad \textbf{4.2}$$

Under the condition that the discriminant, $\Delta_d$, is positive, there will be one real eigenvalue, $\lambda_r$ and a pair of complex conjugated eigenvalues, $\lambda_{cr}\pm\lambda_{ci}$. The advantages in Zhou's method are that it is based on invariants, and therefore frame independent. Also, nonzero complex

eigenvalues are only produced by regions of circular or spiraling streamlines, meaning shear layers are eliminated from the detection algorithm even though they may have high vorticity. One modification was made to Zhou's method. The final $\lambda_{ci}$ value was divided by the local velocity magnitude,

$$|\lambda_{ci}| = \frac{\lambda_{ci}}{V_{mag}} \qquad \textbf{4.3}$$

It was found that dividing by the velocity magnitude tended to yield larger magnitudes around the vortices (which were mostly in low velocity regions), and suppress the shearing regions (mostly in the high velocity wake regions). This technique was compared with other methods and determined to be the most consistent and reliable in detecting the trailing vortices from the rising bubbles.

Normally the vortices are visualized by plotting isosurfaces or contours of the magnitude of the complex part of the eigenvalue, $\lambda_{ci}$. In this case $|\lambda_{ci}|$ was the analyzed quantity. The detection of the vortices was carried out here by first binarizing the $|\lambda_{ci}|$ values. Any $|\lambda_{ci}|$. value greater than zero, it is assumed, represents a vortex. The binarized scalar field was then put through a nearest neighbor search to determine the nonzero values that were connected to each other, separating the individual vortices from each other. Once the Vortices are separated, their sizes and positions can be determined. This number was determined manually to represent the approximate size of one of the tip vortices.

Figure 4.7 shows two cases, a "contaminated bubble" containing surfactants, and a "clean" bubble that rebounds from the free surface. In the case where there is no rebound, The vortex

pair that originally trailed behind the bubble comes up and slowly dissipates as it travels along the surface away from the bubble.

The bubbles rising in surfactant solution all exhibited qualitatively similar behavior. Figure 4.12 shows the isosurfaces of the $|\lambda_{ci}|$ values. Figure 4.13 show the tracking of vortex centers for the "contaminated" bubble. The vortex centers clearly exhibit different behavior for different sized bubbles.

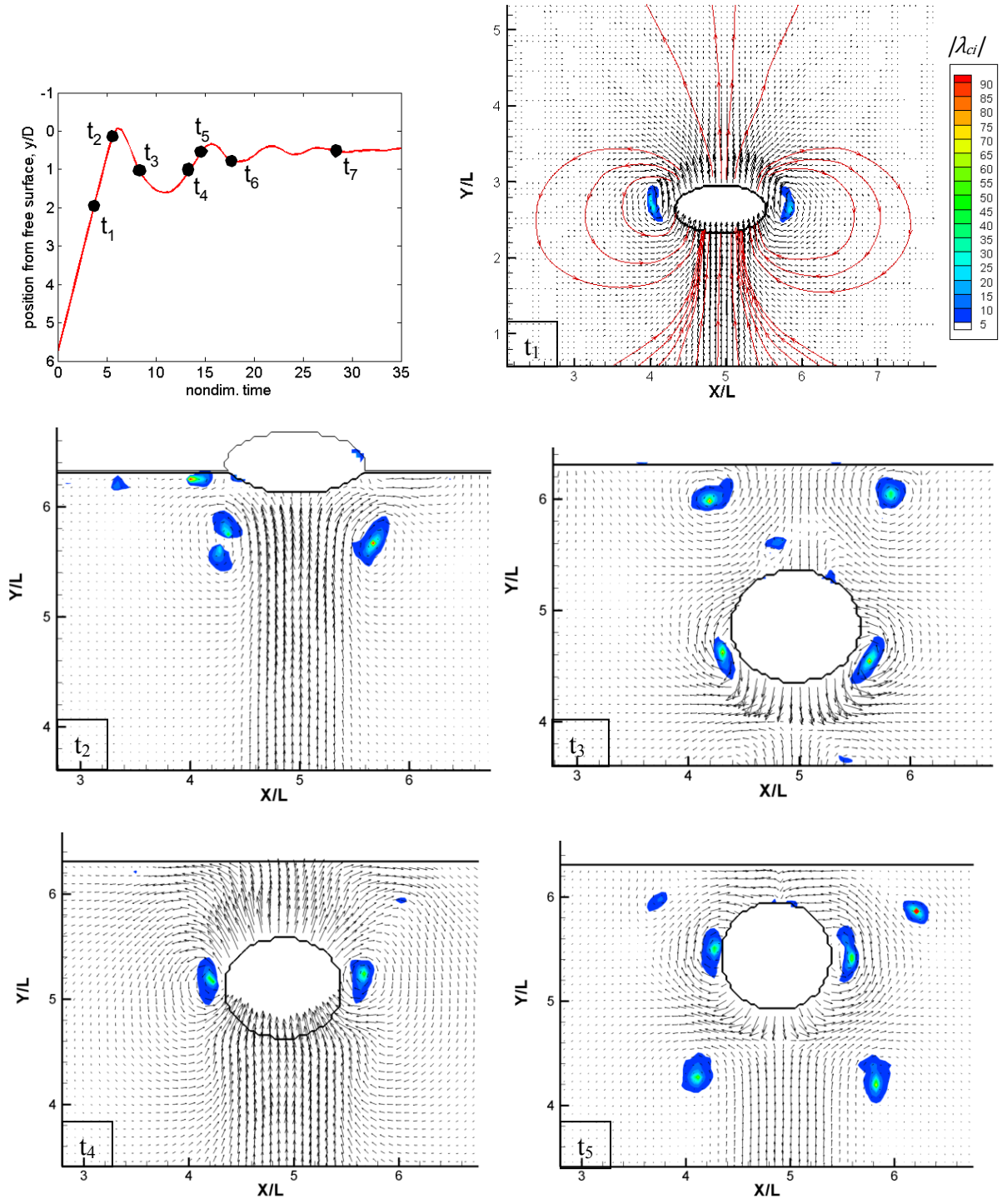


**Figure 4.9- –(a)-(f). Sequence of PIV velocity fields around a 1.06 mm bubble traveling in pure water (Re=360) as it approaches and rebounds multiple times from a free surface. The corresponding trajectory plot is also given for reference.**

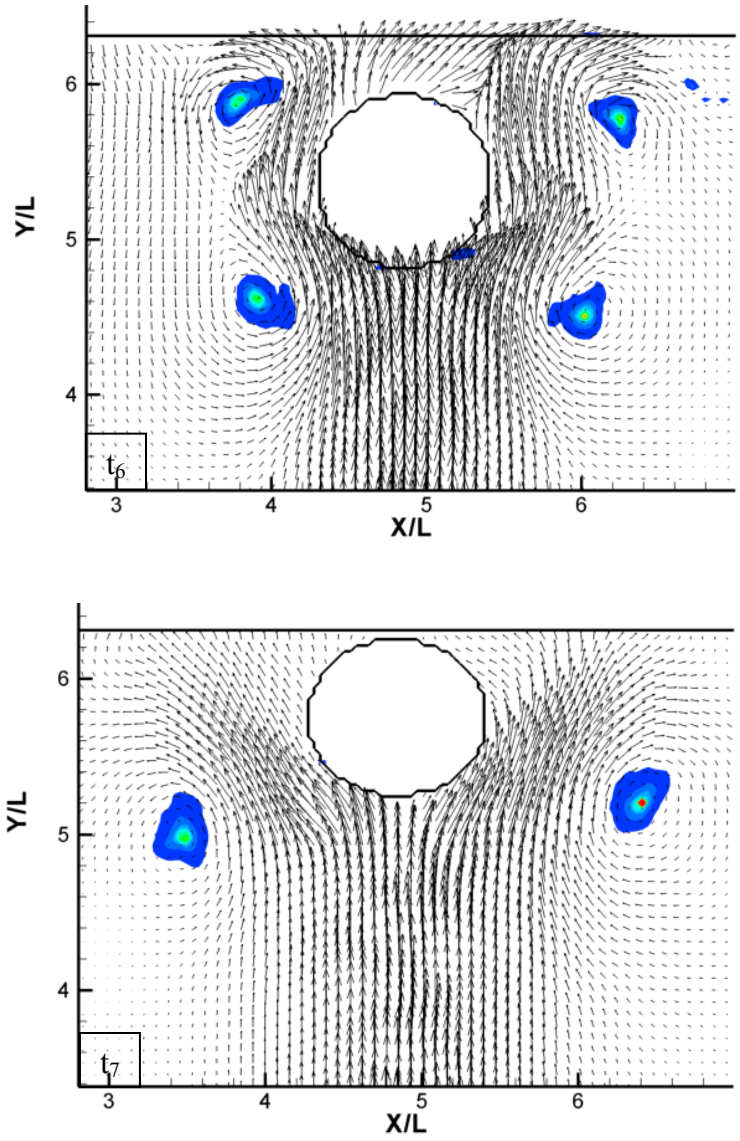


**Figure 4.10- continued:(g),(h)**

## CONCLUSIONS

The presence of a surfactant significantly affects the approach and collision characteristics of a bubble. The surfactant changes the viscous forces around the bubble due to the adsorption coverage of the surfactant at the bubble-fluid interface. A bubble traveling through a surfactant solution (1e-3 M Sodium Dodecyl Sulfate) did not exhibit bouncing behavior regardless of the size. In contrast a relatively large (1.1 mm) bubble in pure water

rebounded from the free surface three distinct times, and even smaller bubbles (800 microns) rebounded from the surface. In the surfactant solution, the flow can be characterized as containing a vortex ring trailing the bubble during the approach stage, and after impact, the vortex ring slow spreads away parallel to the wall and dissipates. The rebounding exhibited complex vortex behavior, and the vortices tended to dissipate more quickly than in the no rebounding case.

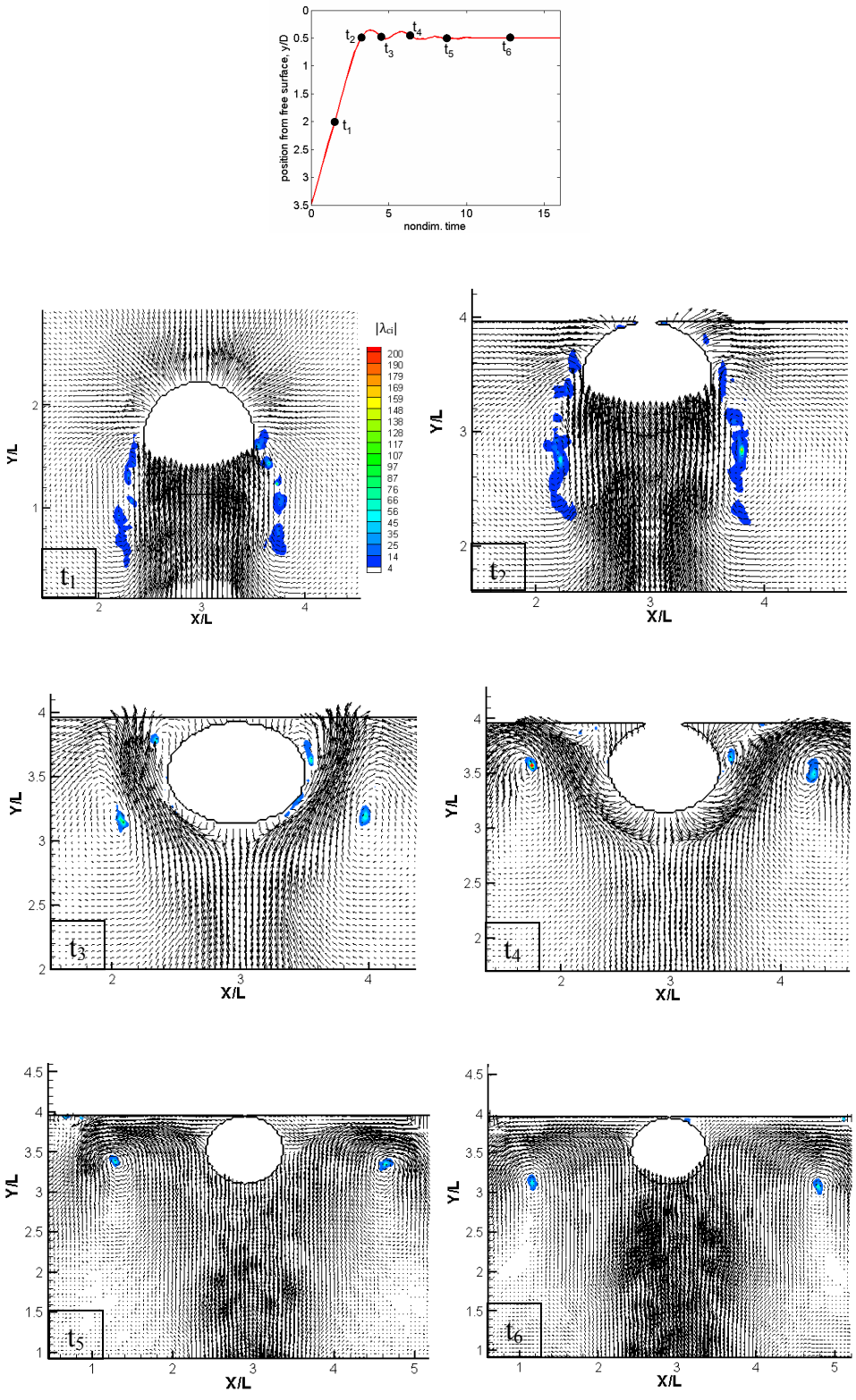


**Figure 4.11 - Sequence of PIV velocity fields around a 1.6 mm bubble traveling in surfactant solution (Re=370) as it approaches and strikes a free surface. The corresponding trajectory plot is also given**

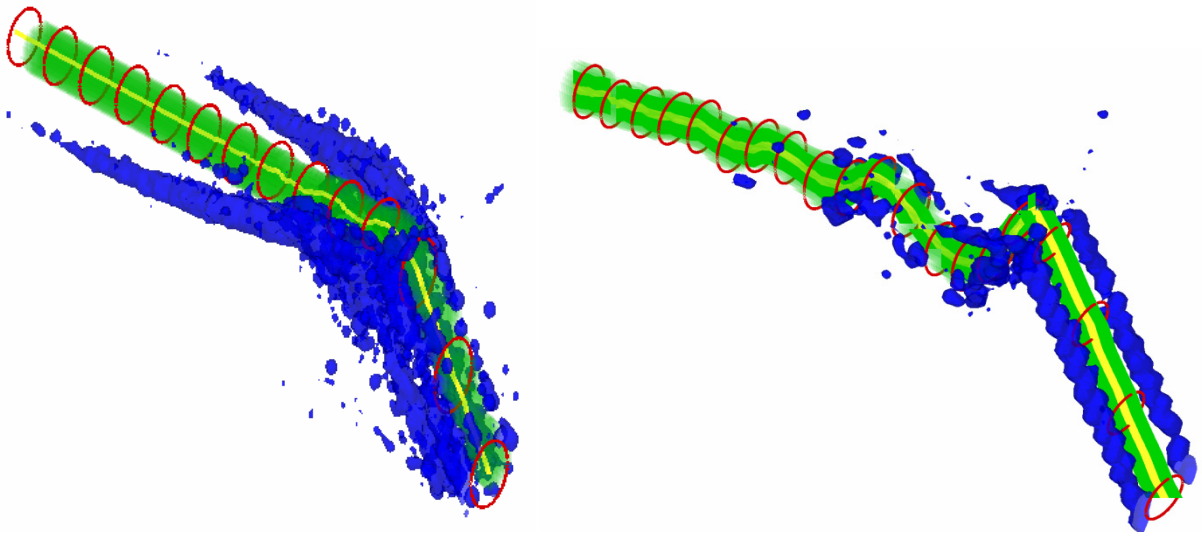

**Figure 4.12 - (a) left and (b) right – Isosurface plot of $\lambda_2$ values for a vortex detection algorithm as the bubbles progress in time. Yellow lines are the trajectories, red outlines are the bubble shapes and the blue regions are the isosurfaces. (a) corresponds to a 1.6 mm bubble in a surfactant solution and (b) corresponds to a 1.1 mm bubble in pure water.**

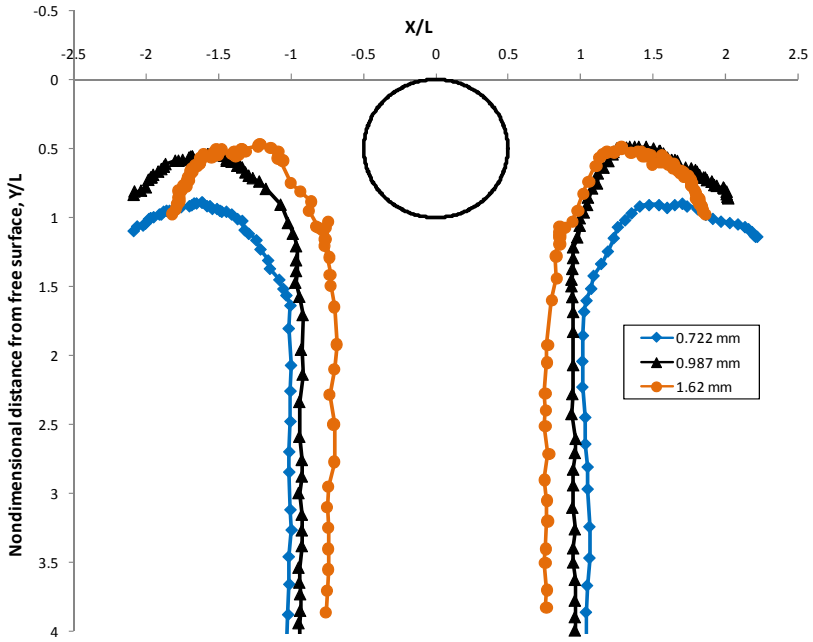


**Figure 4.13 - Vortex center tracking in a surfactant solution. None of these rising bubbles exhibited any rebounding with the free surface. They also maintained circular shapes throughout**

## REFERENCES


1. Davis, R.H., J.M. Serayssol, and E.J. Hinch, *The Elastohydrodynamic Collision of 2 Spheres.* Journal of Fluid Mechanics, 1986. **163**: p. 479-497.
2. Joseph, G.G., et al., *Particle-wall collisions in a viscous fluid.* Journal of Fluid Mechanics, 2001. **433**: p. 329-346.
3. Legendre, D., C. Daniel, and P. Guiraud, *Experimental study of a drop bouncing on a wall in a liquid.* Physics of Fluids, 2005. **17**(9): p. -.
4. Canot, E., et al., *Numerical simulation of the buoyancy-driven bouncing of a 2-D bubble at a horizontal wall.* Theoretical and Computational Fluid Dynamics, 2003. **17**(1): p. 51-72.
5. Malysa, K., M. Krasowska, and M. Krzan, *Influence of surface active substances on bubble motion and collision with various interfaces.* Advances in Colloid and Interface Science, 2005. **114**: p. 205-225.
6. Zholkovskij, E.K., et al., *Dynamics of rear stagnant cap formation at low Reynolds numbers 1. Slow sorption kinetics.* Journal of Colloid and Interface Science, 2000. **226**(1): p. 51-59.
7. Griffith, R.M., *The effect of surfactants on the terminal velocity of drops and bubbles.* Chemical Engineering Science, 1962. **17**: p. 107-1070.
8. Wu, M.M. and M. Gharib, *Experimental studies on the shape and path of small air bubbles rising in clean water.* Physics of Fluids, 2002. **14**(7): p. L49-L52.
9. Raffel, M., C.E. Willert, and J. Kompenhans, *Particle image velocimetry : a practical guide*. Experimental fluid mechanics. 1998, Berlin ; New York: Springer. xvi, 253 p.
10. Hain, R. and C.J. Kahler, *Fundamentals of multiframe particle image velocimetry (PIV).* Experiments in Fluids, 2007. **42**(4): p. 575-587.
11. Haller, G., *An objective definition of a vortex.* Journal of Fluid Mechanics, 2005. **525**: p. 1-26.
12. Zhou, J., et al., *Mechanisms for generating coherent packets of hairpin vortices in channel flow.* Journal of Fluid Mechanics, 1999. **387**: p. 353-396.

# Chapter 5: NUMERICAL MODELING AND EXPERIMENTS OF COARSENING FOAM

This document is under review by the *International Journal of Mineral Processing*

Hyunsun Do[1]*, Michael Brady[1]*, Pavlos P. Vlachos[2], Demetri P. Telionis[1] and Roe-Hoan Yoon[3]
[1]Department of Engineering Science and Mechanics
[2]Department of Mechanical Engineering
[3]Department of Mining Engineering
Virginia Polytechnic Institute & State University
Blacksburg, VA 24060 USA

## ABSTRACT

Numerical and experimental results of drying and wetting foam are presented. Foam can be wetted by wash water delivered on its top boundary, or drained by allowing the liquid to move downward in response to gravity. These processes are governed by nonlinear equations that in special cases accept exact solutions. Here we develop a numerical model that satisfies realistic boundary conditions. Numerical results are presented in conjunction with experiments conducted with coarsening foam. In addition, calculations were carried out modeling the wetting and draining of coarsened foam. From the simulations and experiments, coarsening bubbles were found responsible for accelerating drainage, or vice versa.

## KEYWORDS

Froth flotation, Flotation bubbles, Flotation kinetics, Computational fluid dynamics, modeling.

(*) Authors one and two have equally contributed to this paper

## INTRODUCTION

Dry foam can be defined as the state of foam where the sides of the polyhedra are flat films with very small thicknesses. These films are called lamellae, and the edges of the polyhedra meet along tubes with tricuspid cross-sections called Plateau borders (PB). In dry foam, the liquid is contained mostly in the Plateau borders. In this paper we develop a model based on dry foam as a basis in order to extend the models to wet foams. This is essential for flotation processes were the dry foam assumption is not applicable.

Small amounts of surfactants are enough to alter the fluid velocity on the walls of the lamellae and the PBs. A dry foam structure is thus equivalent to a complex network of solid pipes, except that the diameters of these pipes can expand and contract depending on the wetness of the foam. Some authors (Leonard and Lemlich [1]; Verbist *et al*. [2]) neglect the viscous losses along the junctions and arrive at simple equations that govern foam drainage. More advanced modeling has also been achieved (Neethling *et al*. [3]; Koehler *et al* [4]) by taking into account losses in the junctions. But most of these solutions have been limited to ideal situations that neglect the coarsening of the foam and its rising. Analytical solutions that meet idealized initial and/or boundary conditions also exist (Verbist *et al* [2]). The aim of the present paper is to develop a numerical model that overcomes this limitation and present its results in combination with experimental validation for foam draining and drying.

Coarsening, a very common phenomenon in practical situations is controlled by two major well-known mechanisms. The first is gas diffusion. Pressure gradients between the different sized bubbles cause gas to diffuse from the smaller bubbles to the larger ones. However, gas diffusion is often neglected in practice because it is a much slower process than drainage. The second mechanism is film rupture. As liquids drain through bubbles, the film gets thinner and thinner

until it breaks. This drainage-induced film rupture has long been studied both experimentally and theoretically (Ivanov and Dimitrov [5]; Manev *et al.* [6]; Sharma and Ruckenstein [7]; Vrij and Overbeek [8]; Wang and Yoon [9]), but there is still no general approach that can explain why film ruptures at certain conditions.

Most of the coarsening research to date involves the measurement of liquid fraction in bulk foam (Carrier and Collin [10]; Monin et al. [11]). Coarsening characteristics are generally inferred from the changing drainage properties such as the measured velocity (Hutzler and Weaire [12]). Direct observation of the changing bubble size, which defines coarsening, is a more useful tool to study foam dynamics and validate foam models. Two major methods to directly analyze bubble size within the foam are light scattering using a coherent light source, and optical measurements using photography. Light scattering directs a laser from one side of a foam to the other, and determines the bubble size based on the attenuation of light intensity (Weaire and Hutzler [13]). Although this technique is useful, it requires a complex model to determine the average bubble size and it is subject to several assumptions about the foam. Direct optical measurements use image processing to separate the individual bubbles and determine the diameter. In the present study we use direct optical measurement to determine the bubble size and capacitance measurements to determine the liquid fraction. Bubble size and liquid fraction are independently measured in a time resolved fashion to study foam drainage and coarsening.

## Experimental Setup

In this section we describe the experimental method to simultaneously determine bubble size and liquid fraction in foam as a function of time. These methods are used to investigate the drainage of stable foams, as well as the characterization of unstable, coarsening foams. The end result is a depiction of the liquid fraction and bubble size that are resolved spatially and temporally. The

liquid fraction is measured by changing capacitance. The bubble size is measured optically using pattern recognition methods developed for this task and described in a following section.

Bubbles are created by air supply that passes through a sintered metal disk beneath a rectangular (1.75”x1.75”x20”) foam column as shown in Figure 1. Varying the porosity of the sintered metal disk controls the bubble size, and consequently the size of the polyhedra in rising foam. The bubbles created here are between 0.5 and 2.5 mm diameter. The foam is allowed to rise to the top of the container and then the airflow is discontinued. The solution is a mixture of the nonionic surfactant Neodol 23-7.5 and deionized water. The surfactant used must be nonionic to work with capacitance-based measurements. Concentrations varied well above the Critical Micelle Concentration (CMC) to create stable foams, here $10^{-3}$M, and well below the CMC for coarsening experiments ($10^{-6}$ M). The capacitance sensors are located on the outside of the cell and are described in the following section.

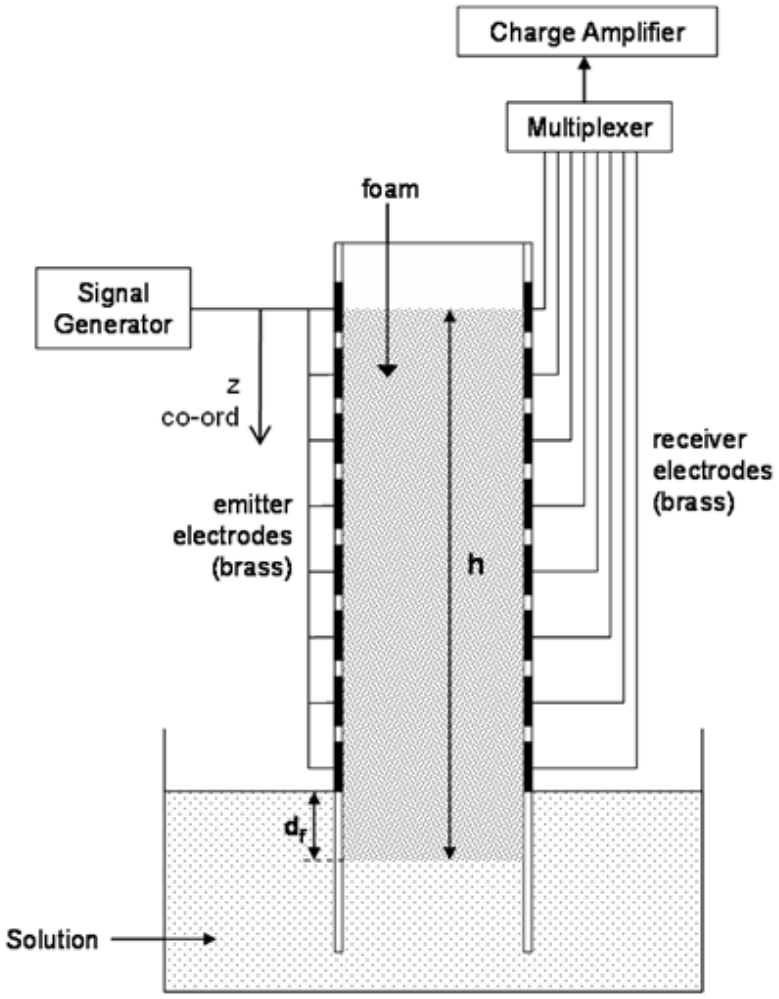


**Figure 5.1 - Foam generation and measurement experimental setup**

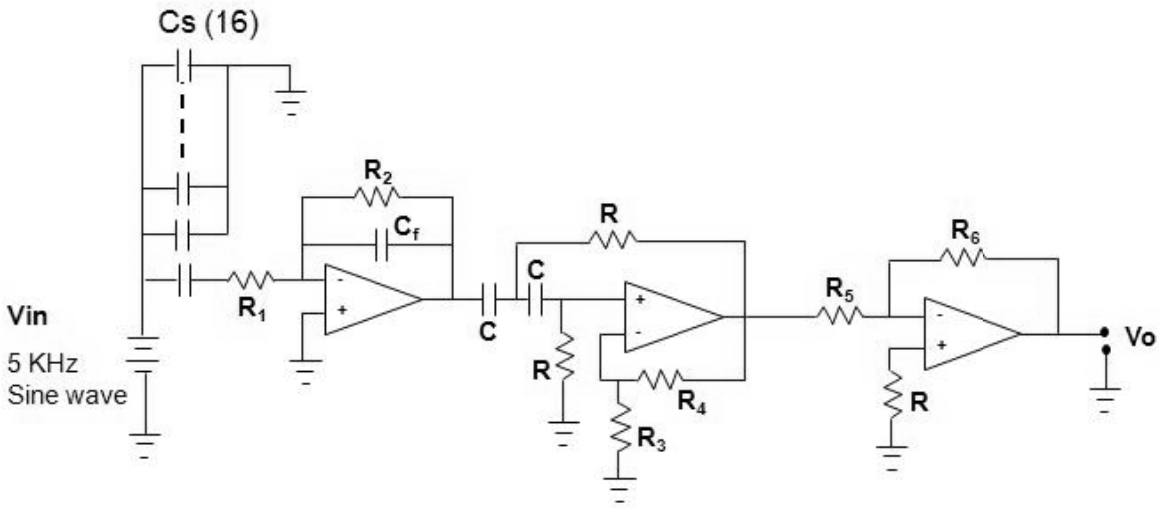


**Figure 5.2 - conditioning circuit layout for capacitance measurements**

## Liquid Fraction Measurement Method

The foam liquid fraction profiles are measured using capacitance sensors. Sixteen sensors are arranged in a parallel plate configuration. A schematic of the process is shown in Figure 1. The electrodes are mounted on the interior of the transparent polycarbonate cell. Each of the emitter electrodes are attached to a sine-wave generator. An AC signal in the kHz range is sent to each of the emitter electrodes. The receiver electrodes are then selectively switched with a multiplexer. As each receiver electrode is being read, the other receiver electrodes are grounded using another multiplexer and a series of analog switches. This method of reading from one receiver electrode and grounding the rest creates electric field lines that are nearly parallel than the case of simply switching the emitter and receiver electrodes while floating the unused ones (Reinecke and Mewes [14]; Halow et al. [15]). Using this method also increases the capacitance for a given electrode surface area and therefore the sensitivity of the sensor. The laws that

govern parallel plate capacitors are now applicable. The output of the multiplexer is then sent through a charge amplifier, a Sallen Key high pass filter, and a voltage amplifier, as shown in Figure 2. The results are then read into a data acquisition card. $V_s$ is the voltage of the sine wave generator, $C_s$ the sensor capacitance, $V_o$ is the output voltage, and f is the input frequency. The transfer function and gain are shown in Figure 2. The amplification of the input sine wave due to the varying capacitance of the foam will be correlated to the liquid fraction. Because the input and output signals are sinusoidal, the gain can be determined by dividing the RMS of the output signal, $V_{o,}$ by the RMS of the input signal, $V_s$, over a set number of cycles. An estimation of the circuit output based on system inputs can be determined assuming that laws of a parallel plate capacitor apply (a dubious assumption given the large distance-to-area ratio between the sensors). A relation between the liquid fraction of the foam and the gain of the circuit can be determined. The capacitance of a parallel plate capacitor with a dielectric medium between the plates is $C_s=\kappa\varepsilon_0 A/d$, where $\kappa$ is the dielectric constant, A is the electrode area, d is the distance between the emitting and receiving electrode, and $\varepsilon_0$ is the permittivity constant $8.8542\times10^{-12}$ $C^2/(Nm^2)$. The liquid fraction is linearly related to the dielectric constant of the foam by, $\phi(\kappa)=(\kappa-\kappa_a)/(\kappa_w-\kappa_a)$, where $\kappa_w$ and $\kappa_a$ are the dielectric constants of water and air, usually taken to be about 1.00053 and 80, respectively. Given the equations of a parallel plate capacitor, the geometry of the tank and, after determining the transfer function of the instrumentation, a liquid fraction versus voltage gain curve can be obtained from the sensor. The transfer function, H(f), is the multiplication of the individual transfer functions of the charge amplifier, the low pass filter and the voltage amplifier and is shown in Equation 1. The gain would be the magnitude of the transfer function. This would give a theoretical approximation to the liquid fraction based on the measured gain of the signal (output voltage over input voltage). However it is necessary to

calibrate the system due to the assumptions made in the derivation, namely the assumption of an ideal parallel plate capacitor and an ideal circuit. Therefore, it is more prudent to calibrate the sensor using a known liquid fraction and a known input/output voltage.

$$H(f)=\left[\frac{R_2}{R_1-\frac{j}{2\pi f C_s}}\right]\cdot\left[\frac{1+\frac{R_4}{R_3}}{\frac{-1}{4\pi^2 f^2 R^2 C^2}-\frac{j}{2\pi f\left(\frac{2-R_4/R_3}{RC}\right)}}\right]\cdot\left[-\frac{R_6}{R_5}\right] \quad \textbf{5.1}$$

The following calibration procedure is being used for each of the capacitors. Foam with a constant liquid fraction throughout the column height is created by wetting the foam from the top with a syringe array releasing solution at a constant flow rate. The equilibrium liquid fraction is verified by observing constant signal intensity of all sensors along the height of the column. Once equilibrium is established, the foam height h, and the depth of the foam extending beneath the solution surface, $d_f$, are measured. The liquid fraction, assuming negligible shear forces on the column walls, can be calculated using hydrostatics,

$$\phi=\frac{d_f}{h} \quad \textbf{5.2}$$

Because the transfer function is nonlinear, the process must be repeated for many liquid fraction values. A calibration curve for a single sensor is shown in Figure 3. The gain versus liquid fraction calibration curve is then constructed, where gain is defined as:

$$\text{Gain}=\frac{\text{RMS}\left[V_{\text{receiver}}\right]}{\text{RMS}\left[V_{\text{emitter}}\right]} \quad \textbf{5.3}$$

The process can be repeated at a rate up to 10 Hz. This relatively fast scan time is somewhat less than the time scale of the foam, making the measurement time resolved. This measurement technique is used in tandem with optical measurements with the camera recording frame rate equal to that sampling rate.

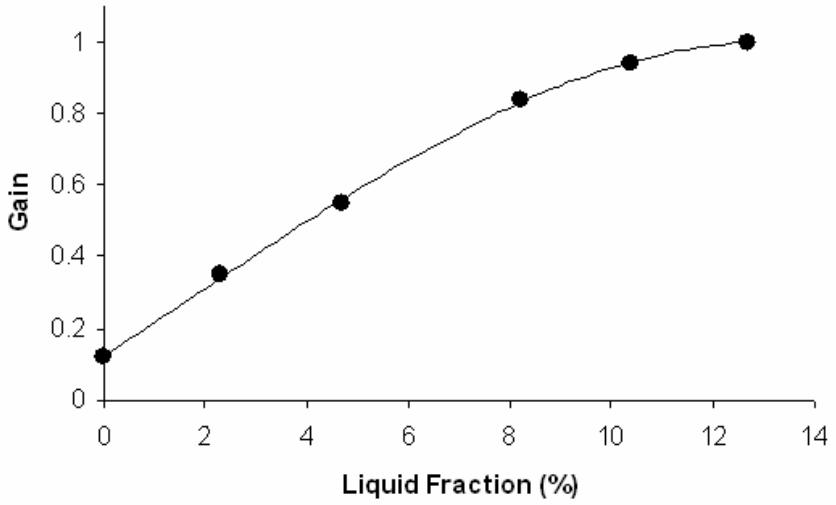


**Figure 5.3 - Typical calibration curve**

## Optical Measurements and Image Processing

The process of taking an original digital photograph of foam and extracting the diameter is based on an image-processing code developed in-house for this purpose. Figure 4 shows a sample photograph of relatively stable foam with a cell diameter of about 1.3 mm. The foam was created using $4x10^{-3}$ M Neodol solution. The image to the left in Figure 4 shows a raw image taken. To more clearly define the boundaries, a high-pass filter is applied to the image. Next, image erosion is used on the filtered image. Image erosion passes a mask image through the

binarized image and the result is the maximum of the input image, multiplied with the mask. Image erosion has the effect of closing holes in the image. For example, if one of the lamellae in Figure 4 is not completely closed with a boundary, and if not corrected, it may be grouped together with other bubbles later during the image processing. To remove noise, image dilation is used. This process has the undesirable effect of increasing the size of the individual bubbles. To restore the correct sizes and shape to the lamellae, the binary image is then eroded again using the same masking element as the previous dilation. The sizes and shapes of the lamellae can now be characterized.

Once the bubbles are separated, the geometric center of mass and the diameter can easily be found using pixel counting. The diameter of the bubbles is simply the diameter of a circle equal in area to the area of the bubbles. Figure 4 (right) shows the lamellae with the corresponding equivalent diameter, the colors indicate the grouping of the different lamellae.

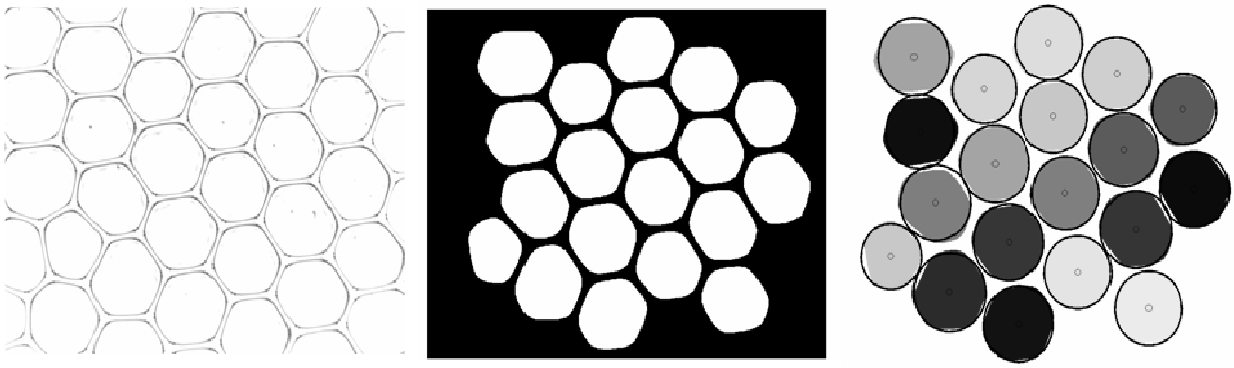

**Figure 5.4 - Optical bubble sizing. Original image (left), after image masking (center), and determination of equivalent bubble size (right)**

## Analytical Modeling

Conservation of mass of the fluid yields a simple relationship between the cross-section of the Plateau Borders (PB), $A$, and the mean velocity in a PB, $u$:

$$\frac{\partial A}{\partial t} + \frac{\partial}{\partial x}(Au) = 0 \tag{5.4}$$

where $x$ is the distance in the vertical direction with origin at the free surface of the foam column. This is based on the assumption of uniform distribution of bubble sizes in the vertical direction, $x$. If the velocity is related to hydrostatic pressure gradients and laminar viscous pressure drop through the PB, one can arrive at the following nonlinear equation (Verbist *et al*.[2]):

$$\frac{\partial A}{\partial t} + \frac{1}{\eta}\frac{\partial}{\partial x}(\rho g A^2 - \frac{C\gamma}{2}\sqrt{A}\frac{\partial A}{\partial x}) = 0 \tag{5.5}$$

where $C$ is a constant determined by the shape of the PB cross section (equal to 0.4 for the current work), $\eta$ is the viscosity, $g$ is the gravitational acceleration, $\gamma$ is the surface tension and $\rho$ is the density of the fluid. Using the following nondimensional quantities among which $\eta^*$ is the effective viscosity approximately 150 times larger than $\eta$ (Verbist *et al*. 1996),

$$x = \xi x_0, \quad A = \alpha x_0^2, \quad t = \tau t_0, \quad x_0 = \sqrt{C\gamma/\rho g}, \quad t_0 = \eta^*/\sqrt{C\gamma\rho g} \tag{5.6}$$

one arrives at the equation

$$\frac{\partial \alpha}{\partial \tau} + \frac{\partial}{\partial \xi}(\alpha^2 - \frac{\sqrt{\alpha}}{2}\frac{\partial \alpha}{\partial \xi}) = 0 \tag{5.7}$$

This is essentially the Berger's equation. It is parabolic in nature, but if the last term is small, it accepts wave-like solutions. Its character is similar to boundary-layer equations and can be solved numerically using well-established methods (Telionis [16]).

Equation (7) is based on the assumption that foam consists only of a network of tubes. This may be acceptable in the case of very dry foams where the sizes of junctions are negligible. But it may no longer be a good assumption for wet foam. The fluid contained in the junctures, *i.e*. the vertices of the polyhedra and the corresponding friction losses must be considered. Whether losses through the vertices or PBs dominates the drainage is still controversial ([1-4]; [16]), but Neethling *et al*. [3] claim that both play important roles. Accounting for the losses through the vertices, a more generalized drainage equation is expressed in terms of liquid fraction ε as follows ([3]).

$$\frac{\partial \varepsilon}{\partial t} + \nabla\left(\frac{\varepsilon \rho g}{k\eta}\right) + \nabla\left(\frac{\varepsilon \nabla(-P_{gas} + \gamma / r)}{k\eta}\right) = 0 \qquad \textbf{5.8}$$

where $r$ is the radius of curvature of PB, $P_{\text{gas}}$ is the gas pressure in a bubble cell, and $k$ is the coefficient of pressure drop that includes both the PB viscous losses ($C_{PB}$) and vertex losses ($C_V$)

$$k = \left(\frac{3C_{PB}}{r^2} + \frac{4.178(C_V - 0.418C_{PB})}{rr_b}(1-\varepsilon)^{1/3} + \frac{6.806(C_V - 1.588C_{PB})}{r_b^{\,2}}(1-\varepsilon)^{2/3}\right) \qquad \textbf{5.9}$$

Here $r_{\text{b}}$ is the bubble radius. In order to recast this equation in terms of the Plateau border cross-sectional area, we noted its relationship to the liquid fraction:

$$\varepsilon = NA / S = N\alpha x_0^2 / S \qquad \textbf{5.10}$$

where $N$ is the total number of PBs in the foam column, and $S$ is the cross-sectional area of the column. Assuming that the temperature does not vary significantly in the froth, one obtains the following relation between the pressure and volume of bubbles ($V_{\text{b}}$):

$$pV_b = \text{constant} = (pV_b)_{top} \qquad \textbf{5.11}$$

and thus we express Eq. (7) in terms of the liquid fraction

$$\frac{\partial \varepsilon}{\partial t}+\frac{\partial}{\partial x}\left(\frac{\varepsilon\rho g}{k\mu}+\frac{\varepsilon\nabla(-(pV)_{top}/(\frac{4}{3}\pi r_b^{\,3})+\gamma/r)}{k\mu}\right)=0 \qquad \textbf{5.12}$$

It should be noted here that the pressure of gas inside a foam cell, neighboring a Plateau Border, is constant, and therefore does not produce a pressure gradient to drive the flow. But the pressure is dropping from cell to cell as we move up in the foam, and therefore these pressure changes will drive the flow through junctions.

Equation (12) is more general than the equation presented in Neethling *et al.* [3], because it accounts for variations in the cell size, expressed in terms of the bubble volume $V_b$ or the bubble radius $r_b$. To non-dimensionalize Eq. (12), one can follow the same approach with Verbist *et al.*'s as shown in Eq.(6) and introduce more of its characteristic parameters such as pressure $\Pi=\mu/t_0$ and surface tension $\Gamma=\mu x_0/t_0$. Then all terms in the equation can be non-dimensionalized with following relations:

$$A=\alpha x_0^2,\quad k=\kappa\cdot C_V/x_0^2,\quad x=\xi x_0,\quad r=\delta\cdot x_0,\quad r_b=\beta\cdot x_0,$$

$$p=p^*\Pi,\quad \gamma=\gamma^*\Gamma \text{ and } t=\tau t_0. \qquad \textbf{5.13}$$

Also from the definitions of the liquid fraction and Bond number, *Bo*,

$$\varepsilon=\frac{4CN/\pi\gamma}{d^2\rho g}\alpha=\frac{4CN/\pi}{Bo}\alpha \qquad \textbf{5.14}$$

in which $d$ is the diameter of the channel. Substituting all of those terms in Eq. (10), one finally obtains:

$$\frac{\partial \alpha}{\partial \tau} + f_1 \frac{\partial}{\partial \xi}\left(\frac{\alpha}{\kappa} + \frac{\alpha}{\kappa}\frac{\partial}{\partial \xi}\left(\frac{-C_1}{\beta^3} + \frac{1}{C\delta}\right)\right) = 0 \qquad \textbf{5.15}$$

where $f_1$ is a constant defined as $150/C_v$, and $C_1$ is a nondimensional parameter defined as $C_1 = 3\rho g(pV_b)_{top} / 4\pi C^2\gamma^2$.

## RESULTS AND DISCUSSION

Three types of experiments were conducted to match the cases considered and solved numerically. These are free drainage, forced drainage and coarsening.

The term "forced drainage" is often used in literature for the case where established foam is allowed to dry, and then it is wetted from its free surface. This is a classical example of a problem that accepts an exact analytical solution in the form of a propagating wave. Uniform foam was created in the setup described earlier and was then allowed to drain until there was very little water content. The foam was then wetted from the top, and the instantaneous liquid fraction profiles were measured and plotted. Figure 5.5 shows the progression of the liquid fraction in time. In this figure the origin, $\xi=0$ corresponds to the free surface, and $\xi$ increases with depth. The shape of the wave profile and the wave speed does not change at all during the forced drainage experiments. The wave speed is defined here as the ratio of the distance between two wave fronts, and the time increment between the two. The wave front position can be defined as the location of the maximum wave slope.

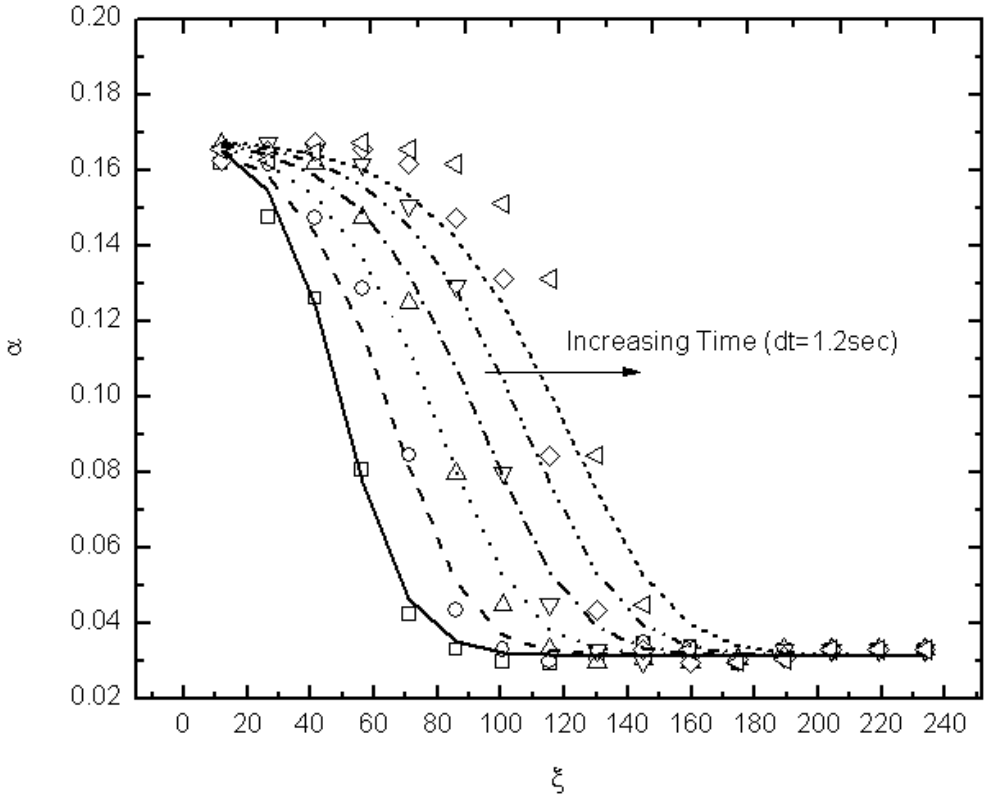


**Figure 5.5 - Forced drainage simulated (lines) and experimental results (symbols). Initially the foam was dry, then wetted from the top , ξ=0, and propagated along the direction of depth ξ**

Free drainage is the progression of the liquid fraction when initially uniform foam (liquid fraction and bubble size) is allowed to drain. The numerical and experimental results of the free drainage are shown in Figure 5.6. For this experiment, we created stable foam using a high concentration of surfactant. The sparger airflow was turned off. Then the foam was wetted from the top using the needle cascade. Once a uniform liquid fraction was attained, the flow of solution to the needles was turned off, marking the beginning of the free drainage experiment. The boundary condition on the free surface for the numerical solution imposes zero liquid

fractions. Bubble sizes are uniform along the foam column. The top boundary was assumed to be very dry while bottom was very wet. The assumption was considered appropriate from the experimental results as the top quickly dries out while the bottom is consistently wet. In this drainage, draining occurs smoothly and the profiles monotonically approach very low values of liquid fraction. It should be noted in both Figures 5 and 6 that the simulation deviates slightly from the experimental data in the middle of drainage. This may be due to the fact that the regime where major liquid contents go through, either the plateau borders (PBs) or their vertices, changes in time. In fact, other researchers have shown this experimentally by observing that the flow characteristics were changing with increased dropping flow rate at the foam top (Koehler [17], [4] , [18]). According to their account this change is attributable to the effect of the PB and whether they PB vertices are dominant or not. The current model does not account for these transient characteristics of the relation between PBs and PB vertices.

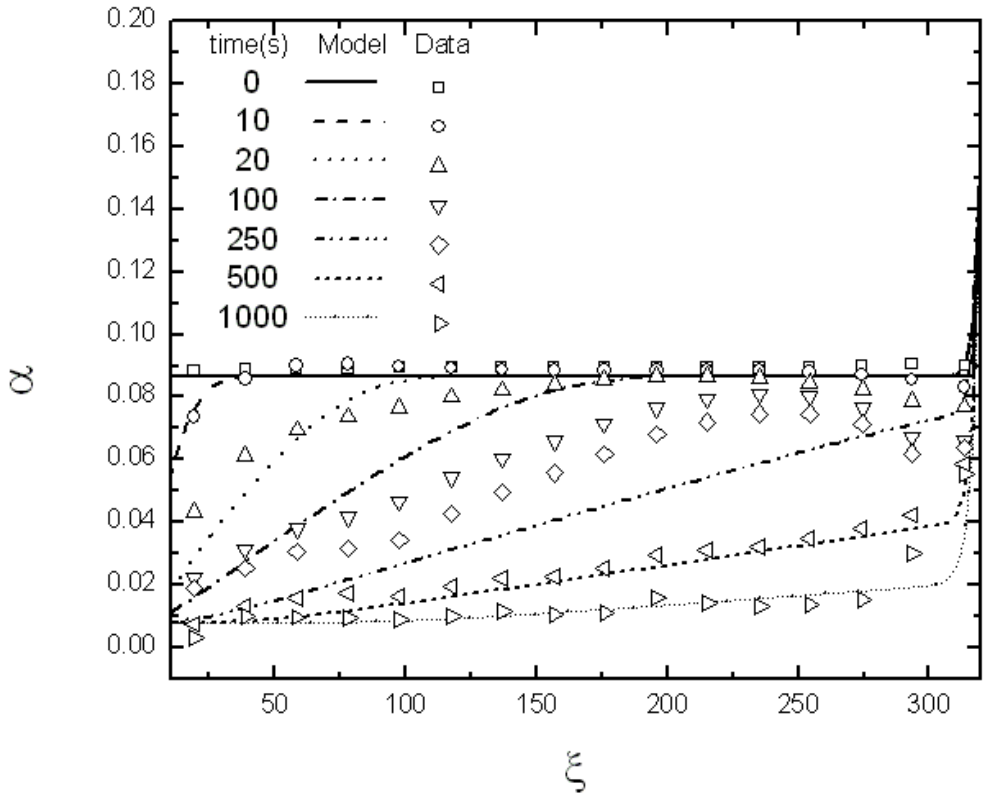


**Figure 5.6 - Comparison of the simulated wetness profile using current model (lines) with data (numerals) for free drainage without coarsening. Liquid fraction data ($\varepsilon$) was converted to $\alpha$ by assuming proper number of PBs (N=30)**

## Coarsening

Coarsening is the changing of bubble size of foam in time. The two main mechanisms for coarsening are lamellae rupture and gas diffusion. In the present coarsening experiments, uniform foam was created and wetted from the top as in the case of free drainage. Then the flow of solution on the top of the foam was stopped and the foam was allowed to evolve. To promote coarsening, a much lower concentration of surfactant ($10^{-6}$ M) was used. The results of a coarsening test are shown in Figure 5.7. The optical measurements were taken at two locations, each with about a 1.5"x1.5" field of view at depths of h/3 and 2h/3. The bubble size measurements shown in Figure 5.7 were averaged over each camera field of view. The liquid

fraction measurements for the locations corresponding to the placement of the cameras are also shown. The plot shows a region of abrupt increase in bubble size (coarsening), occurring simultaneously with a sharp decrease in the liquid fraction. This trend is observed at both locations shown. The liquid fraction measurements show three distinct regions: a drainage region where the foam has not yet coarsened, a sharp decrease in liquid fraction during coarsening, and a region of very small liquid fraction after the foam has coarsened. Another observation is that the slope of the liquid fraction in the drainage region seems to have decreased from the first location to the second. In addition, the slope of the liquid fraction in the coarsening region also seems to have decreased towards the bottom of the tank.

As shown in the coarsening experiment, bubble sizes change not only with respect to time but to their positions also. Coarsening is accountable in the current drainage model (see Eq.15) when an analytical relation among bubble size, its position, and time evolution is known. The lack of proper model for the lamellae rapture and the corresponding bubble size growth render the problem of incorporating a drainage model with coarsening very challenging. On that ground, direct comparison between the experiment and the model is not presented here except for separate simulations in Figures 5.8 and 5.9. The simulated profiles in Figure 8 were obtained assuming an ideal case where bubble size changes as a function of position only. Bubble size was assumed to be linearly increasing with height, such that bubble diameters are five times larger at the top than at the bottom. Changes of the number of PBs due to coarsening were ignored. All other conditions for the simulation were the same as in Figure 5.6. The wetness profile deviates significantly from that of free drainage with mono-dispersed bubbles. Given all other conditions equal, foam with higher value of $C_1$ (lower surface tension) shows more wet regions near bottom. This means that lower surface tension, that is, higher surfactant

concentrations, decelerate the foam drainage process if the coarsening rate is assumed to be unaffected by that change. Another indirect comparison of the experiment is given in Figure 5.9. Given two different uniform bubble sizes along the column, presented are the changes of local wetness at near top, middle, and bottom of foam. Larger bubbles show faster drainage and one may conclude that larger bubbles accelerate drainage as the fixed input parameter in this case was the bubble size. Carrier et al. [19-20], also observed similar trends experimentally in mono-dispersed foams introducing different sizes of bubbles.

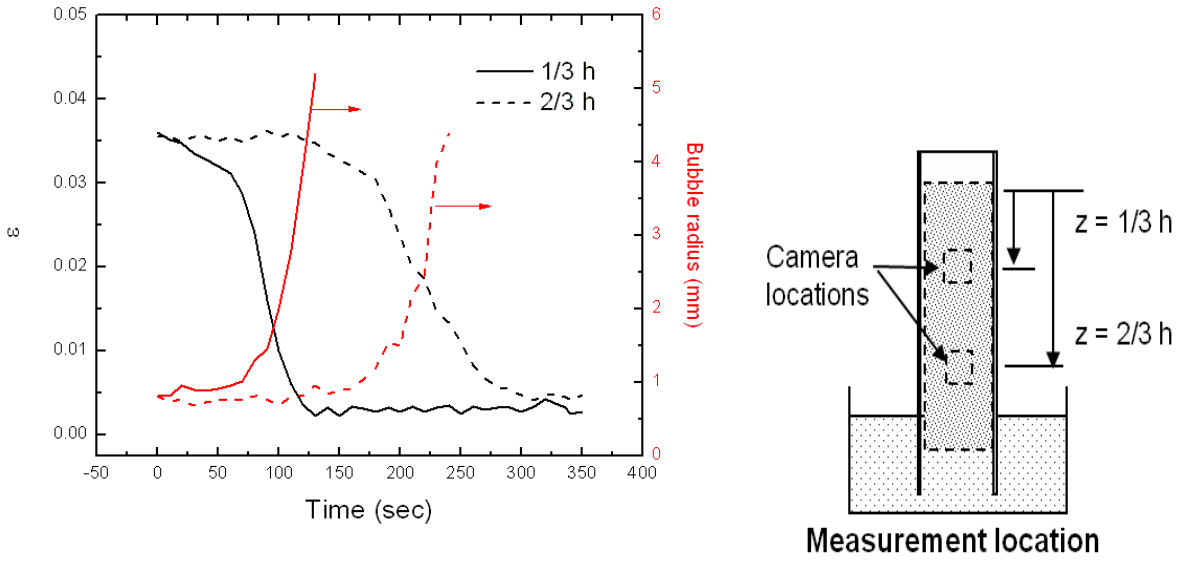


**Figure 5.7 - Typical coarsening results (left) and corresponding camera positions. (right). Liquid fraction in black and bubble size in red lines**

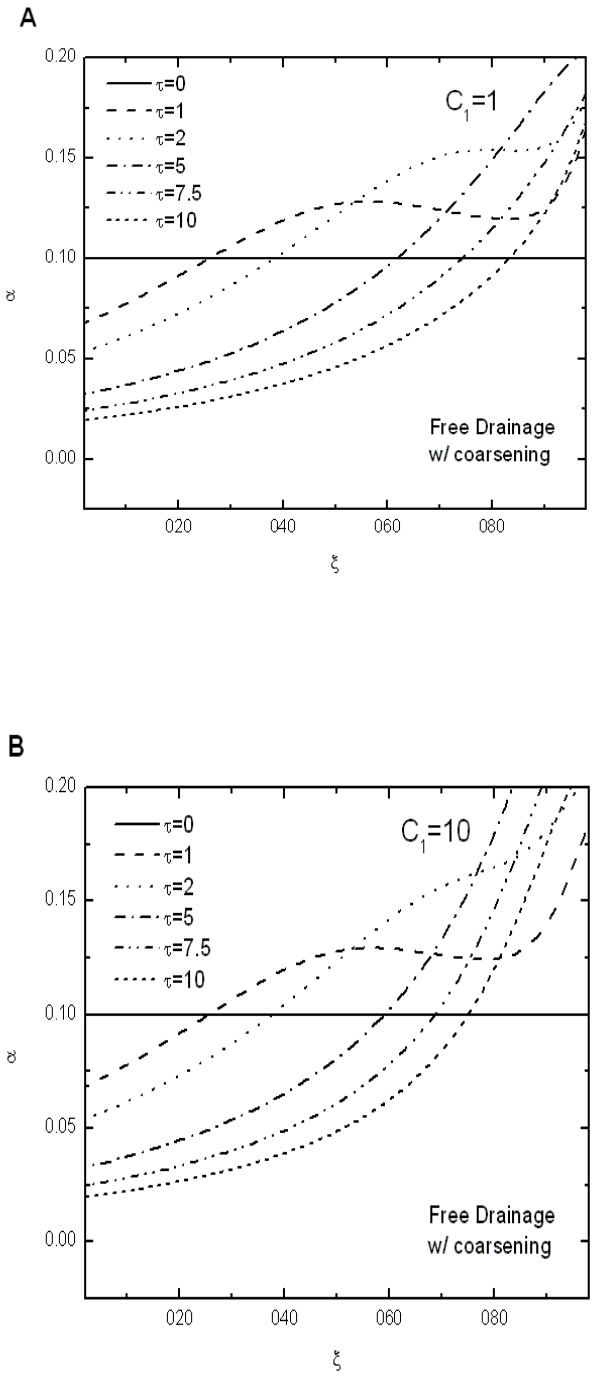


**Figure 5.8 - Simulated wetness profile for free drainage with coarsening. Figures show how the profiles evolve with the changes of C1 as in Eq.(15)**

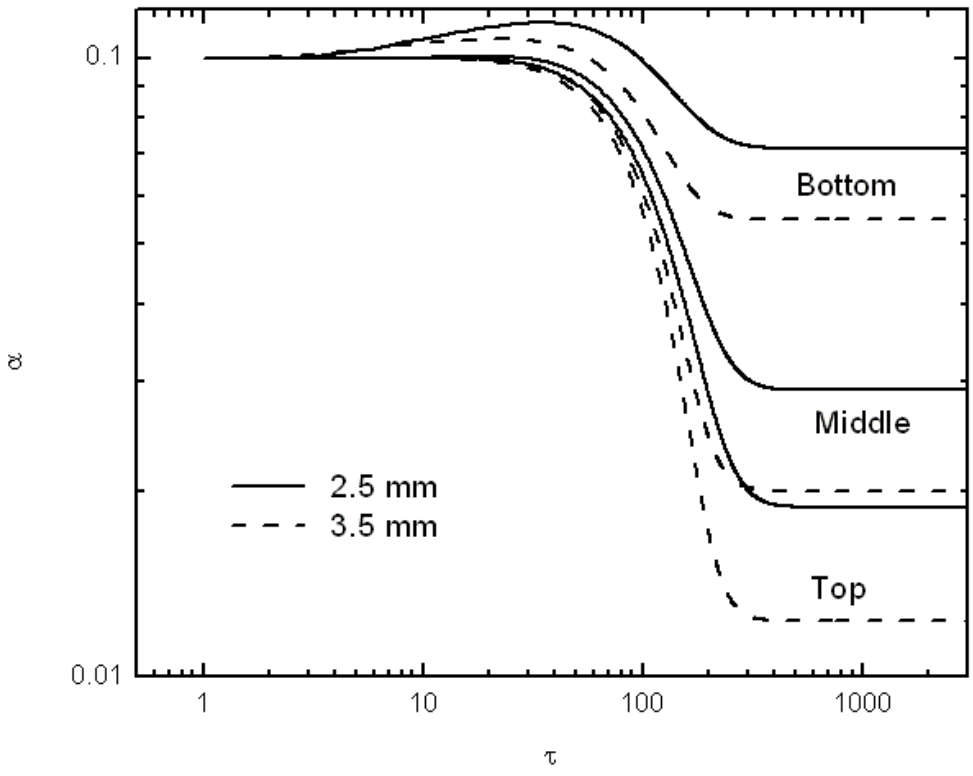


**Figure 5.9 - Simulated liquid fraction change for free drainage at different positions. Solid lines are for 2.5mm bubbles, and dashed lines are for 3.5mm**

## CONCLUSIONS

Drainage through foam was studied both experimentally and numerically. The liquid fraction profiles of forced drainage experiments showed the classical wave-like solutions of analytical drainage models. Without coarsening, the free drainage experiments showed good agreement with the theoretical model developed. Free drainage experiment on coarsening foam showed that the tendency of the bubble size change corresponds to that of the liquid fraction change at a given position. Simulations were also run for other cases with realistic boundary conditions of foam such as locally-changing bubble sizes, and different initial bubble sizes. The wetness profiles deviated significantly from those of mono-dispersed foam when arbitrary changes of bubble size were implied in the model. Bubble coarsening was observed in the experiment, and its relation to drainage was found both experimentally and numerically.

## ACKNOWLEDGEMENTS

The support of the Department of Energy (DOE) Center for Advanced Separation Technology (CAST) is gratefully acknowledged

## REFERENCES


1. Leonard, R.A. and Lemlich, R., 1965, A study of interstitial liquid flow in Foam", *AICHE Journal*, 11, 18-29.
2. Verbist, G., Weaire, D. and Kraynik, A.M., 1996, The foam drainage equation, *J.Phys.:Condens.Matter* 8, 3715-3731.
3. Neethling, S.J., Lee, H.T. and Cilliers, J.J.,2002, A foam drainage generalized for all liquid contents, *.Phys.:Condens.Matter* 14,331-342.
4. Koehler, S.A., Hilgenfeldt, S. and Stone, H.A.,2000, A generalized view of foam drainage: experiment and theory, *Langmuir* 16, 6327-6341.
5. Ivanov,I.B. and Dimitrov, D.S.,1974, Hydrodynamics of thin liquid films.- Effect of surface viscosity on thinning and rupture of foam films, *Colloid and Polymer Sci*. 252, 982-990.
6. Manev, E., Scheludko, A. and Exerowa, D.,1974, Effect of surfactant concentration on the critical thickness of liquid films, *Colloid Polym. Sci*. 252, 586-593.
7. Sharma, A. and Ruckenstein, E., 1987, Critical thickness and lifetimes of foams and emulsions: role of surface wave-induced thinning, *J. Colloid and Interface Sci.* 119, 14-29.
8. Vrij, A. and OVerbeek, J., 1968, Rupture of thin liquid films due to spontaneous fluctuations in thickness, *J.Amer. Chem. Soc.* 90, 3074-3078.
9. Wang, L. and Yoon, R.-H., 2006, Role of hydrophobic force in the thinning of foam films containing a nonionic surfactant, *Collids and surfaces A*: Physicochem. Eng.Aspects 282-283, 84-91.
10. Carrier, V., and Colin, A., 2003, Coalescence in draining foams, *Langmuir* 19, 4535-4538
11. Monin, D., Espert, A., and Colin, A.,2000, A new analysis of foam coalescence: from isolated films to three-dimensional foams, *Langmuir* 16, 3873-3883.
12. Hutzler, S., Weaire, D., 2000, Foam coarsening under forced drainage, *Philosophical Magazine Letters* 80(6), 419-425.
13. Weaire, D., and Hutzler, S., The Physics of Foams, 2001, Oxford University Press.

14. Reinecke N, and Mewes D.,1996, Recent developments and industrial/research applications of capacitance tomography., Measurement Science and Technology, 7, pp 233-246.
15. Halow J.S., Fasching G.E., Nicoletti P, and Spenik J.L., 1993, Observations of a fluidized bed using capacitance imaging., *Chem. Eng. Sci.* 48., 643-659.
16. Telionis, D.P., *Unsteady Viscous Flow,* 1981, Springer.
17. Koehler, S.A. Hilgenfeldt, S. and Stone, H.A., 2004, Foam drainage on the microscale: I. Modeling flow through single plateau borders, *J. Colloid. Int. Sci. 276*, 420-438.
18. Koehler, S.A., Hilgenfeldt, S. and Stone, H.A.,1999, Liquid flow through aqueous foams: the node-dominated foam drainage equation, *Physical review letters* 82(21), 4232-4235
19. Durand, M, Martinorty, G. , and Langevin, E. , Liquid flow through aqueous foams: from the plateau-border-dominated regime to the node-dominated regime, *Phys. Rev. E*, 60. (6), R6307
20. Carrier, V., and Colin, A., 2002, Foam drainage: A film contribution?, *Phys. Rev. E* ,65, 061404

# Chapter 6: Summary of Findings and Impact

The major findings of each chapter and their broad impact will now be stated.

A range of turbulence characteristics, including isotropic turbulence was created in a model flotation cell using a turbulence grid as described in chapter 2 of this document. The turbulent dissipation rate was measured using a cross-correlation-based Particle Image Velocimeter. Particle Tracking Velocimetry was used to determine the velocity fluctuations of the solid particles and the bubbles relative to the fluid phase. RMS velocities of particles and bubbles were calculated and compared to experimental and theoretical models that are based on the turbulent dissipation rate. The particle RMS slip velocity was in good agreement with Liepe and Möckel's empirical model, demonstrating 12% mean error. A theoretical model, derived by Levins and Glastonbury was found to be in good agreement with the bubble RMS, but substantially underpredicted the RMS of the solid particles. In addition, the theoretical models derived by Abrahamson, and Williams and Crane provided good and almost identical agreement in predicting the RMS of the bubble velocity, but did not do as well in predicting particle fluctuations. Multiphase, turbulent collision models are currently used in the flotation industry. However, validation of the models has not been investigated experimentally. The findings in Chapter 1 have contributed to the overall validity of the collision models, and flotation modeling in general.

The mean flow, as well as turbulent quantities were measured in a Rushton turbine using time resolved DPIV. The objective in Chapter 3 was to provide accurate turbulence measurements in the impeller stream. The periodic component of the flow was found to contribute significantly to the fluctuating velocities. In addition the turbulent kinetic energy was reduced by up to 45% by

removing the blade frequency. The turbulent kinetic energy dissipation rate was found to be less affected by the periodicity of the flow, varying by as much as 8%. The flow was shown to be anisotropic close to the impeller. Vortex detection revealed that the tip vortices travel in a nearly radial direction from the impeller for small Reynolds numbers and in more erratic directions for higher Reynolds numbers. The maximum and mean normalized dissipation in the impeller stream showed decreasing trends with the Reynolds number. Other normalized turbulence quantities, namely $U_{rms}$, $V_{rms}$, Reynolds stresses and vorticity magnitude scaled as nearly constant values with the Reynolds number. Good agreement was found for time averaged Reynolds stresses and turbulent energy dissipation. The work on the Rushton impeller, described in Chapter 3, is of importance to flotation fundamentals. The fundamentals of a small scale Rushton mixing device can be applied to flotation machines. The effect of the blade passage on the turbulence has not been investigated fully, and the accurate characterization of the turbulent kinetic energy and turbulent dissipation rate is important in understanding turbulent mixing. The isotropic nature of the turbulence is also of importance to validate the use of computational models in similar turbulent environments. The primary contribution of this chapter is the tracking of the tip vortices and their distribution in the impeller stream. The tip vortices carry the majority of the turbulent kinetic energy in a mixing vessel. The advection and breakdown of these tip vortices is significant to understand the overall energy dissipation, and structure of the turbulence within a mixing vessel.

The rise and interaction of a bubble with a free interface was investigated with Time Resolved Particle Image Velocimetry in Chapter 4. The presence of a surfactant significantly affects the approach and collision characteristics of a bubble. The surfactant changes the viscous forces around the bubble due to the adsorption coverage of the surfactant at the bubble-fluid interface.

A bubble traveling through a surfactant solution (1e-3 M Sodium Dodecyl Sulfate) did not exhibit bouncing behavior regardless of the size. In contrast a relatively large (1.1 mm) bubble in pure water rebounded from the free surface three distinct times, and even smaller bubbles (800 microns) rebounded from the surface. In the surfactant solution, the flow can be characterized as containing a vortex ring trailing the bubble during the approach stage, and after impact, the vortex ring slow spreads away parallel to the wall and dissipates. The rebounding exhibited complex vortex behavior, and the vortices tended to dissipate more quickly than in the case with surfactant adsorption. The behavior of a rising bubble and its interaction with a free interface is important to the fluid mechanics of flotation. Bubble and solid particles collide in flotation machines, and the characterization of the flow around the bubble, and how it varies with a surfactant, is very important for collision modeling. The analysis in Chapter 4 can be used to better model collision characteristics and drag properties of bubbles in flotation environments.

Drainage through different types of foams was studied both experimentally and numerically in Chapter 5 of this dissertation. The liquid fraction profiles of forced drainage experiments showed the classical wave-like solutions of analytical drainage models. Without coarsening, the free drainage experiments showed good agreement with the theoretical model developed. Free drainage experiments on coarsening foams showed that the change in bubble size corresponds to a changing liquid fraction at a given position. Simulations were also run for other cases with realistic boundary conditions of foam such as locally-changing bubble sizes, and different initial bubble sizes. The wetness profiles deviated significantly from those of mono-dispersed foam when arbitrary changes of bubble size were implied in the model. Bubble coarsening was observed in the experiment, and its relation to drainage was found both experimentally and numerically. The recovery process and its optimization in flotation is strongly dependant on the

nature of the foam and its stability. A robust method to measure foam coarsening is not available in the literature. The experimental technique developed was used to validate foam drainage and coarsening models and can be directly applied to current flotation coarsening models and their validation.

Each of the problems studied here were determined to be areas where modern experimental fluid mechanics can contribute fundamental research and understanding of the floatation process. The understanding of the underlying physics can lead to the design and use of more efficient flotation systems.